Design of a Rotor-tied Doubly fed Induction Generator

by

OreOluwa I. Olubamiwa

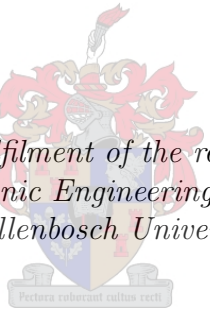

Thesis presented in partial fulfilment of the requirements for the degree of Master of Electrical and Electronic Engineering in the Faculty of Engineering at Stellenbosch University

Department of Electrical and Electronic Engineering,
University of Stellenbosch,
Private Bag X1, Matieland 7602, South Africa

Study leader: Dr Nkosinathi Gule

December 2017

Declaration

By submitting this thesis electronically, I declare that the entirety of the work contained therein is my own, original work, that I am the sole author thereof (save to the extent explicitly otherwise stated), that reproduction and publication thereof by Stellenbosch University will not infringe any third party rights and that I have not previously in its entirety or in part submitted it for obtaining any qualification.

Date: December 2017

Abstract

The severe effects of climate change has seen a global push towards an increase in the use of renewable energy sources. Wind energy is a major renewable energy source and its usage in electricity generation is steadily rising. The doubly fed induction generator (DFIG) is the most commonly used generator in wind turbines due to its wide speed range of operation and easy power factor control implementation. DFIGs also use fractionally rated power converters which have lower converter losses compared to fully rated converters in induction and synchronous generators.

Recently, a new DFIG topology (the rotor-tied DFIG) has been proposed. In this topology, the DFIG's rotor is connected to the grid and the stator to fractionally rated power converters. This topology has been shown to lead to higher efficiency as the higher frequency (grid frequency) is on the rotor core, which is typically smaller than the stator core, thus lower core losses. It was also suggested that designing DFIGs in this topology could lead to higher power densities. The topology requires no extra complexity in operations as a similar control system used with a conventional DFIG can be used.

The steady state operation of the rotor-tied DFIG is first discussed and a new method of calculating slip for this topology is given. The proportions of the rotor and stator power to the input mechanical power to the generator at different slip values are illustrated. The transformer model equivalent circuit of rotor-tied DFIGs is also described.

The purpose of this study is to design and optimize a low power rotor-tied DFIG. The design process is presented in a sequential manner from the calculation of the rotor size, to the rotor and stator winding parameters, then the slot and core dimensions. The obtained model is then evaluated with finite element analysis (FEA) specific for rotor-tied DFIGs. The FEA is used to evaluate the power density, power factor and efficiency. The harmonic content in the model is also assessed. The design is then optimized to increase the power density and lower the harmonic content.

A 5.5 kW rotor-tied DFIG is designed and its performance is evaluated using FEA. The optimization is executed using a response surface approximation of the FEA model with a genetic algorithm and this significantly reduces optimization time. The design of experiments for the response surface approximation is based on a combination of the latin hypercube sampling and composite sampling methods.

Finally, a prototype is constructed and tested in a DFIG standalone mode. The tests are conducted in the sub-synchronous, synchronous, and super-synchronous regions of operation. The stator is excited with DC at synchronous speed, and slip frequency AC by the use of an AC drive at other speeds. The rotor is connected to a resistive load in all the tests. Tests results show that the prototype's efficiencies at synchronous and sub-synchronous speeds, for the rated stator current, are similar. The efficiencies at super-synchronous speeds are however lower with the same rated stator current due to the power rating of the AC drive used to excite the stator.

Uittreksel

Die ernstige gevolge van klimaatsverandering het tot 'n globale toename in die gebruik van hernubare energiebronne gelei. Windenergie vorm 'n belangrike deel van die energiebronne en die gebruik van wind vir kragopwekking styg aanhoudend. Die dubbel-gevoerde induksie generator (DFIG) is die mees algemeen gebruikte generator in wind turbines weens sy wye omvang van spoed werking en eenvoudige implementering van arbeidsfaktor beheer. DFIGs gebruik ook laer kapasiteits omsetters in vergelyking met gewone induksie en sinchrone generators.

Onlangs is 'n nuwe DFIG topologie (rotorgebonde DFIG) voorgestel. In die topologie word die masjien se rotor aan die netwerk gekoppel en die stator aan lae kapasitiet omsetters. Dit is bewys dat die topologie tot 'n hoër masjien effektiwiteit lei, omdat die hoër frekwensie op die rotor is. Dit lei tot minder kernverliese, weens die feit dat die rotor kleiner is as die stator. Dit is ook voorgestel dat DFIGs wat so ontwerp word, tot hoër drywingsdigthede kan lei. Die bedryf van 'n rotorgebonde DFIG vereis ook nie ekstra kompleksitiet nie, aangesien konvensionele DFIG beheerstelsels toegepas kan word.

Die bestendige toestand werking van die rotorgebonde DFIG word bespreek, waarna 'n nuwe metode vir die berekening van die glip vir die topologie gegee word. Die verhouding tussen die rotor en stator drywing en die megansiese intree drywing by verskillende glip waardes word geïllustreer. Die ekwivalente transformator model van die rotorgebonde DFIG word ook beskryf. Die doel van die navorsing is om 'n lae drywing rotorgebonde DFIG te ontwerp en te optimeer.

Die ontwerp proses word op 'n opeenvolgende wyse aangebied, vanaf die berekening van die rotor grootte, die rotor- en statorwikkelingsparameters en uiteindelik die gleuf en kern dimensies. Die voorgestelde model word dan met behulp van eindige element analise (EEA) geëvalueer. Die eindige element analise word gebruik om die drywingsdigtheid, arbeidsfaktor en effektiwiteit te evalueer. Die harmoniese inhoud in die model word ook geassesseer. Die ontwerp word dan geoptimeer om die drywingsdigtheid te verhoog en die harmoniese inhoud te verlaag.

'n 5.5 kW rotorgebonde DFIG is ontwerp en die prestasie word geëvalueer met behulp van die EEA program. Die optimeering geskied met behulp van 'n generiese oppervlak reaksie benadering algoritme. Die metode verminder die optimeeringstyd aansienlik. Die ontwerp van die oppervlak reaksie benadering is 'n kombinasie van die latyn hiperkubus en saamgestelde monsternemingsmetodes.

Ten slotte word 'n prototipe van die rotorgebonde DFIG gebou en getoets in 'n alleenstaande modus. Die toetse word uitgevoer vir die sub-sinchroon, sinchroon en super-sinchroon bedryfstoestande. Die stator is opgewek met 'n GS-bron by sinchroon spoed en met glip frekwensie WS, by die ander bedryfstoestande. Die rotor is aan 'n weerstandslas gekoppel vir al die toetse. Die toetsresultate toon dat die prototipe se effektiwiteit by sub-sinchroon en sinchroon spoed vir ken stator stroom, is soortgelyk. Die effektiwiteit by super-sinchroon is egter laer as gevolg van die kendrywing van die WS omsetter wat gebruik is om die stator op te wek.

Publications

Parts of this thesis were presented in the following conference papers:

- O. I. Olubamiwa and N. Gule, "Design methodology for rotor-tied doubly fed induction generators," *Southern African Universities Power Engineering Conference (SAUPEC),* Stellenbosch, 2017.
- O. I. Olubamiwa and N. Gule, "The steady state operation of a rotor-tied doubly fed induction generator," *Southern African Universities Power Engineering Conference (SAUPEC),* Stellenbosch, 2017.

Acknowledgements

I would like thank the following people for the various roles played throughout the project:

- My supervisor, **Dr Nkosinathi Gule** for his guidance throughout this project and instilling in me a valuable research philosophy for future projects. Thanks for your conscientious supervision.
- My parents, **Dr Olayiwola & Mrs Abiodun Olubamiwa** for their financial support throughout my studies, their prayers and advice. God bless you.
- My **EMLab colleagues** for their advice, motivation and support.
- Mr Pietro Petzer, Andre Swart, Murray Jumat, Howard Koopman, Kenan and Tsepang for their assistance during the construction of the prototype.

Blessed be the name of God forever and ever, for wisdom and might are His.

Contents

List of figures

List of tables

Nomenclature

Acronyms

DD	Direct drive
DFIG	Doubly fed induction generator
DOE	Design of experiments
FEM	Finite elements method
IM	Induction machine/motor
LHS	Latin hypercube sampling
PMSG	Permanent magnet synchronous generators
SCIG	Squirrel cage induction generator
SG	Synchronous generator

DFIG design parameters

α	Flux density shape factor	
$\beta_{r,s}$	Rotor, Stator chording factor	
$\cos\varphi, Pf$	Power factor	
η	Efficiency	
λ	Stack aspect ratio	
σ_{tan}	Rotor tangential stress	Nm^{-2}
τ	Pole pitch	mm
$\tau_{rp,sp}$	Rotor, Stator slot pitch	mm
θ_{sk}	Rotor skew angle	^{0}
A	Specific electric loading	$\mathrm{A\,m}^{-1}$
a_1	Number of current parallel paths	
a_p	Number of conductors in parallel	
A_{co}	Wire cross section	mm^2
A_{su}	Slot useful area	mm^2
$B_{g,t,c}$	Air-gap, teeth, core flux density	T
$b_{r1,2}$	Rotor slot widths	mm
$b_{s1,2}$	Stator slot widths	mm
$b_{tr,s}$	Rotor, Stator teeth widths	mm
C	Essons constant	$\mathrm{J/dm}^{-3}$

D	Diameter	mm
d_{co}	Wire diameter	mm
f	Frequency	Hz
f_{sm}	Maximum slip frequency	Hz
g	Air-gap length	mm
$h_{or,s}$	Rotor, Stator slot opening height	mm
$h_{r,s}$	Rotor, Stator slot height	mm
h_w	Slot wedge height	mm
J_{co}	Current density	A/mm^2
k_f	Form factor	
k_w	Winding factor	
k_{fe}	Stacking factor	
k_{fill}	Slot fill factor	
L	Stack length	mm
n	Rated machine speed	rpm
$N_{r,s}$	Number of rotor/stator turns per phase	
$n_{r,s}$	Number of rotor/stator slots	
$n_{sr,s}$	Number of turns per rotor/stator slots	
p_1	Number of machine pole pairs	
P_n	Rated power output	kW
q	Number of slots per pole per phase	
S	Apparent power	kV A

Equivalent circuit parameters

ϕ_m	Magnetizing flux	Wb
Ψ	Flux linkage	Wb – t
$\underline{E}$	Induced voltage	V
$\underline{I}$	Induced current	A
$\underline{I}_m$	Magnetizing current	A
$\underline{V}$	Supplied voltage	V
a_{rs}	Effective turns ratio	
L_l	Leakage inductance	H
L_m	Magnetizing inductance	H
R	Winding resistance	Ω
X_l	Winding reactance	Ω

X_m	Magnetizing reactance	Ω

Generator power & speed

Ω_m	Rotor mechanical speed	$\mathrm{rad\,s^{-1}}$
ω_m	Rotor mechanical angular frequency	$\mathrm{rad\,s^{-1}}$
ω_r	Rotor flux frequency	$\mathrm{rad\,s^{-1}}$
ω_s	Stator flux frequency	$\mathrm{rad\,s^{-1}}$
P_m	Mechanical power input to generator	W
P_r	Rotor power	W
P_s	Stator power	W
s	slip	
T_m	Mechanical torque input to generator	$\mathrm{N\,m^{-1}}$
T_{em}	Electromagnetic torque	$\mathrm{N\,m^{-1}}$

Superscripts

$'$	Stator parameters referred to the rotor side

Subscripts

$_r$	Rotor parameters
$_s$	Stator parameters

Chapter 1

Introduction

The presently felt effects and fore-casted implications of climate change has resulted in an increased push towards adopting clean energy world-wide. Global transformation to a low carbon economy, involving reduced dependence on fossil fuels and increase in the use of renewable energy, is being pursued to tackle climate change [1]. On the back of the climate change agreement signed at the United Nations Climate Change Conference COP 21 in 2015, a significant leap in the usage of renewable energy by various countries is apparent. In 2015, a new record for global investment in renewable energy was set at $285.9 billion topping the former record of $278.5 billion in 2011 [1, 2].

About 134 GW of electricity from renewable energy (not including power from large hydro projects) was commissioned in 2015, representing about 53.6% of total power generation projects installed that year. Out of this, wind power accounted for 62 GW while solar photovoltaics 56 GW. Although there has been a rapid decrease in the average global levelised costs of solar power from $315 per MWh in 2009 to $122 per MWh in 2015, onshore wind power remains cheaper slated at $83 per MWh. Offshore wind power average costs have also decreased to about $174 per MWh from over $200 per MWh in 2012 [1].

A comparison of the total generating capacities of different renewable energy sources including Hydro as at 2015, is illustrated in Figure 1.1. Wind power represents about 23.4 % of the global renewable energy capacity, positioning as the second highest installed renewable energy source worldwide [3].

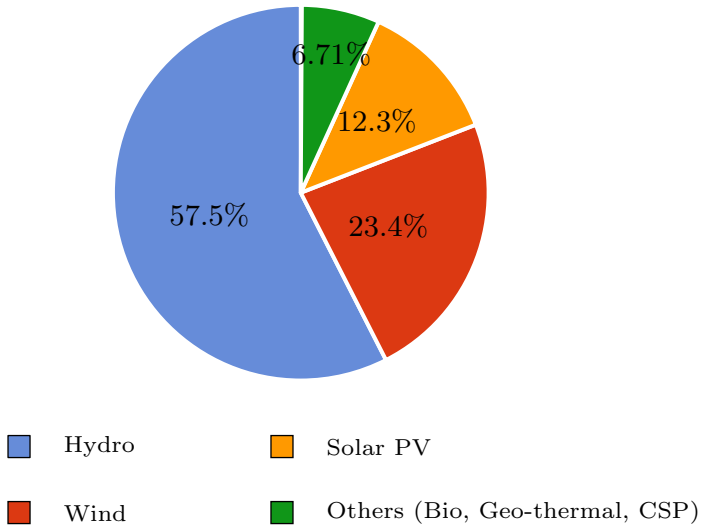

Figure 1.1: Percentages of installed electricity generation capacity from renewable energy globally as at 2015 [3].

Wind power, being a leading global source of renewable energy, as at 2015, made up about 7% of total global electricity generation capacity, with a total installed capacity of approximately 432.9 GW. Wind power also accounted for about 4% of global electricity supply the same year.

The growth trend of global wind power installations from 2005 to 2015, is illustrated in Figure 1.2. It is moderately projected that global wind capacity could grow to about 791.9 GW by 2020 and 977 GW by 2030 [4]. Citing technical and economic potentials in the wind energy sector, an optimistic forecast will see the wind energy capacity surpassing 1800 GW, constituting about 12% of global power generation capacity by 2030 [5].

Renewable energy is no longer viewed as a luxury affordable only to developed countries, and 2015 saw developing economies invest as high as $156 billion in renewable energy excluding large hydro power plants. This was in contrast to the $130 billion invested by developed nations the same year. Although coal is abundant in South Africa, building coal fueled plants in the future may face challenges with investor concerns around exposure to stranded assets due to global climate policies and preferences of cleaner energy technology by development banks [1].

Although wind energy is site specific, the wind resource potential in South Africa is regarded as high, with the presence of high wind speeds along the coastal regions [6]. South Africa has the highest installed wind power capacity in Africa, as about 483 MW of wind power was added in 2015 to the South African national grid, taking the total capacity to 1,053 MW. Furthermore, the Integrated Resource Plan (IRP) has set a target for South Africa to hit 9,000 MW of wind power capacity by 2030 [4].

In [1], cost competitiveness is identified as a major cause of the growing trend of usage of renewable energy in electricity generation. For wind energy conversion systems (WECS), generators which convert the mechanical energy harnessed from the turbine blades to electrical energy were singled out as key components whose choice could lead to decreased costs in [7].

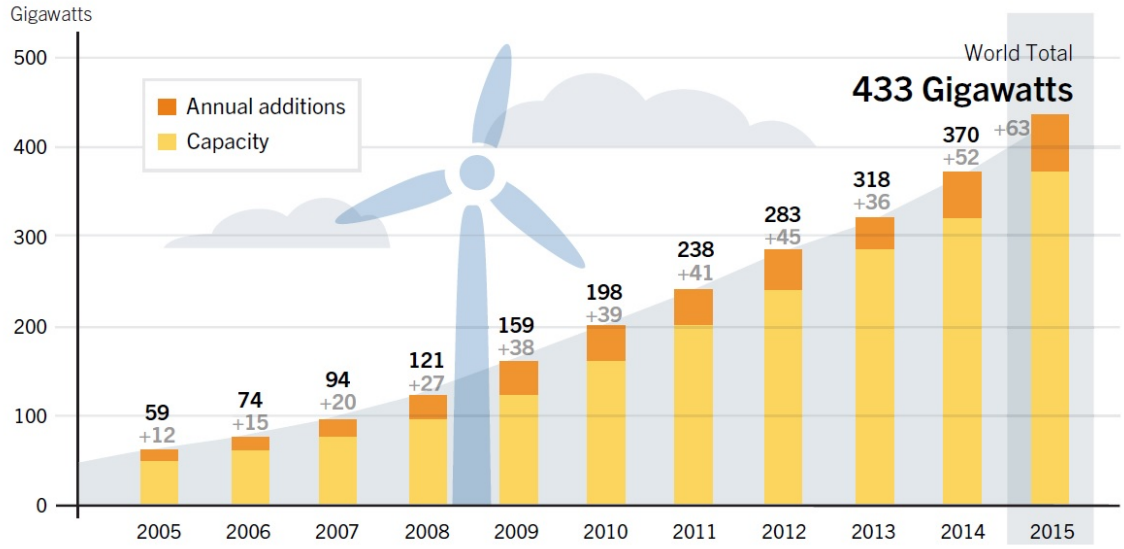

Figure 1.2: Global installed wind power capacity growth trend [3].

In the following section, a quick outline of the components used in wind turbines is given. Generators commonly used in turbines are also discussed considering certain factors including topology, manufacturing costs, repairs and maintenance, suitability to wind turbine locations, and efficiency.

1.1 Wind energy conversion systems

Wind turbines used to harness wind power, are operated at fixed speeds or with variable speed capabilities. Early wind turbines developed in the 1970s were designed as fixed speed turbines, and are featured more in low power systems. The fixed speed turbines are typically associated with asynchronous (squirrel cage induction) generators. Modern wind turbines are commonly operated at variable speeds with advantages of cost effectiveness, improved power quality and efficiency. The variable speed wind turbines also boast of decreased mechanical stresses in the turbine system and islanding capabilities [8].

Variable speed turbines have these common components:

- Pitch/yaw control system to regulate the amount of power absorbed by the turbine by pitching (positioning) the turbine blades in and out of wind direction
- Electrical generator for energy conversion
- Electrical control system evaluating and regulating torque, pitch angle and reactive power

Other components include gearboxes and transformers.

The common variable speed wind turbine topologies, which are based on the wind generator type employed include [7, 9]:

- Geared brushless generators (permanent magnet synchronous generators (PMSGs) or squirrel cage induction generators (SCIGs)) with fully rated converters
- Direct drive (DD) systems with PMSGs
- Doubly fed induction generators (DFIGs) with fractionally rated converters

A background on the generators used in these topologies is provided in the following subsections.

1.1.1 Permanent magnet synchronous generators (PMSGs)

PMSGs are operated in variable speed wind turbines with gearboxes and fully rated converters as illustrated in Figure 1.3(a), or as direct drive systems as illustrated in Figure 1.3(b). PMSGs have gained recognition recently because of their high power density and small mass. PMSGs have further advantages of increased reliability due to the absence of slip rings and brushes, and improved efficiency due to the absence of losses associated with field windings.

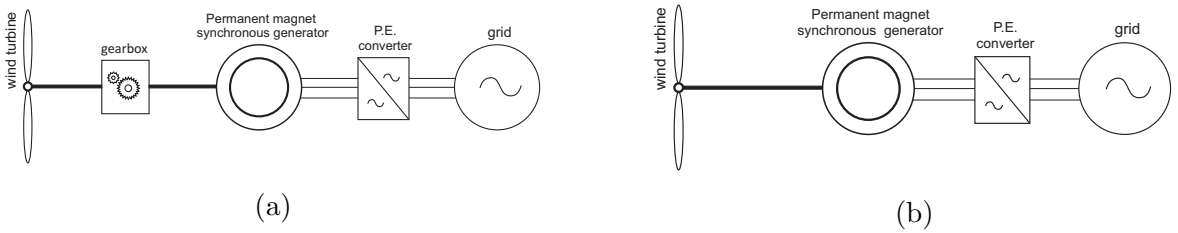

Figure 1.3: (a) Geared SGs with fully rated converters, (b) DD SGs with fully rated converters.

Although PMSGs are considered as the generator choice for small wind turbine applications and used by several manufacturers, the cost of permanent magnets at times prove too high for larger systems. Synchronous generators tend to exhibit low damping such that sudden in rush or gusts of wind are not effectively absorbed electrically and cause unwanted oscillations in the machines which reduce power quality [10].

DD systems typically use PMSGs with fully rated converters, but avoid using gearboxes in order to improve the reliability of wind turbines. However, with the absence of gearboxes, low speed generators are required which are bulky and less efficient than high speed generators [7].

1.1.2 Squirrel cage induction generators (SCIGs)

Squirrel cage induction machines are renowned for their robustness, simplicity, high reliability and low costs. SCIGs are squirrel cage induction machines which are rotated at speeds higher than synchronous speed to generate electricity. SCIGs possess a high level of damping compared to synchronous machines enabling them of better rotor speed fluctuation and drive transient absorption [10]. When used in variable speed wind turbines, SCIGs are operated with gearboxes and fully rated converters as shown in Figure 1.4 [7, 9]. During operation, SCIGs draw reactive power from the utility grid due to the lack of voltage control. SCIGs also have problems of voltage instability [10].

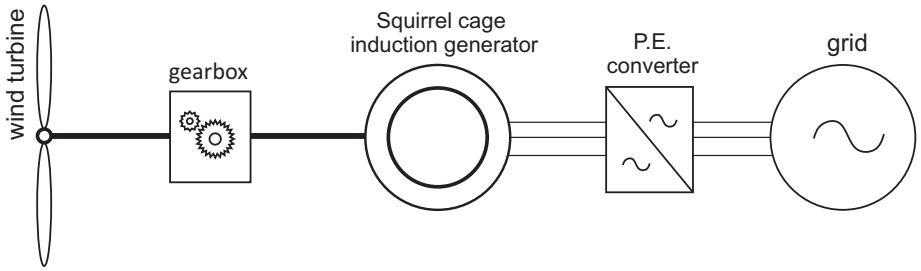

Figure 1.4: SCIGs with fully rated converters.

1.1.3 Doubly fed induction generators (DFIGs)

DFIGs presently edge out their counterparts in prevalence of usage. Put simply, DFIGs are wound rotor induction generators which conventionally have their stator windings directly connected to the grid, while the rotor windings are connected via fractionally rated converters, with gearboxes in their drivetrains as illustrated in Figure 1.5. The access to the rotor windings through slip rings and carbon brushes allow for adjustment of rotor current magnitude, frequency and phase angle. Consequently, they can be operated over a wide speed range (typically between ±30 % of the synchronous speed). Advantages of DFIGs include a wide speed range of operation, easy power factor control, less mechanical stresses and power fluctuations [8,11]. DFIGs also use fractionally rated power converters which have lower converter losses compared to fully rated converters used with SCIGs and PMSGs. Earlier DFIGs suffered from poor grid-fault ride-through capabilities but recent research have brought about improvements [7].

DFIGs generate voltage at constant magnitude and frequencies at varying mechanical speeds by having voltages at slip frequency supplied to the rotor terminals to induce currents that complement the speed changes. All these are accomplished by a robust control system employed alongside DFIGs which also carry out other tasks like maximum power point tracking, power factor control and harmonic filtering.

Ignoring power factor requirements, DFIGs operate in sub-synchronous (positive slip), synchronous (zero slip), and super-synchronous (negative slip) states. The rotor speed is lower than the synchronous speed in the sub-synchronous region and higher in the super-synchronous region. The DFIG operating in the sub-synchronous state draws power from the grid through the rotor terminals at slip frequency. In the super-synchronous state, the rotor terminals supply power to the grid. In the event of the DFIG rotating at synchronous speed, the current in the rotor terminals will be DC with no net power supply or withdrawal. Considering the generating quadrants for DFIGs, in all 3 cases, the stator terminals supply power to the grid.

The speed range that can be accommodated by a DFIG depends on the converter size. The converters supply or draw powers in fractional levels to the stator power and the common practice is for converter ratings to be between a quarter and a third of the rated machine power. This translates to a slip range of about ± 0.3 [8].

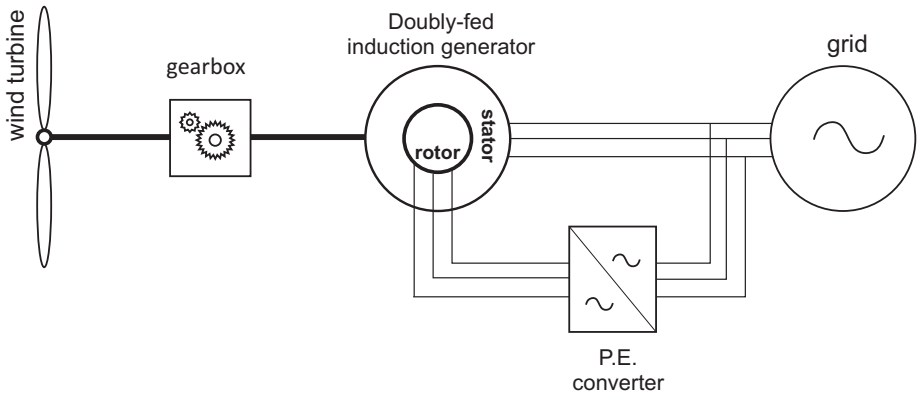

Figure 1.5: (Geared DFIGs with partially rated converters

1.2 Literature review

Three phase squirrel cage induction machines (IMs) are commonly used in industries, and their design methodology is comprehensively documented in several literature including [12–15]. In these literature, various examples of IMs designed to different specifications are presented. The design of large (> 100 kW) wound rotor induction machines is discussed in [12], while a more nuanced DFIG design methodology is given in [16]. The design methodology given in [16] is for large DFIGs in the MW region. As such, some of the DFIG design aspects presented in [16] are useful only for large DFIGs. The optimal design of a large (10 MW) DFIG is also presented in [17]. This DFIG is however designed for direct drive wind turbine topologies.

In [18], a computer aided design (CAD) approach for the design of small DFIGs is discussed. A CAD program is used alongside finite element analysis (FEA) to design a 2 kW DFIG. According to [18], certain design variables including the air-gap flux density, electric loading, current densities, stack length to inner stator diameter ratio and slot opening to slot pitch ratios, can be selected for the design of small DFIGs in the same manner as the design of induction machines. Other variables such as the stator to rotor turns ratio, slot winding type (integral or fractional), and number of winding layers are identified as needing special attention in small DFIG designs.

Although analytical equations used by the CAD program in [18] are not provided, a flow chart of the CAD program is illustrated. The flow chart starts with the determination of machine specifications and initialization of design variables to calculate the main machine dimensions. After the main dimensions calculations, the flow chart has three sequential loops, the first is to ensure that the maximum teeth flux density is below the specified value by adjusting the number of slots per pole per phase and number of current parallel paths. The second loop is to ensure adequate rotor slot area by adjusting any convenient design variable. The third loop is to ensure convergence of weight and efficiency under given constraints by also adjusting the design variables. FEA is used at the end of the flow chart for validation of of design results.

The following subsections are reviews of the topics listed below:

- The methods used in the air-gap sizing of induction machines (including DFIGs).
- The rotor-tied DFIG design and performance
- The rotor-tied DFIG mode of operation and equivalent circuit
- The rotor-tied DFIG in relation to the use of rotary transformers
- Harmonic analysis and mitigation in DFIGs
- DFIG prototype tests without the use of a control system

1.2.1 Induction machine air-gap sizing

Different methods of determining an induction machine's air-gap size are given in available literature, and the D^2L, is a term commonly used to quantify the air-gap size. The use of the Esson's "constant" C is discussed in [12] for the air-gap sizing. The value of the Esson's "constant" with different power ratings is illustrated in Figure 1.6(a) as given in [12]. Using the desired power rating and number of pole pairs, the value of C can be

traced and used to calculate the D^2L of the machine. A similar constant to the Esson's constant is given in [14] for calculating the D^2L with a slightly different scale of units. The value of the machine constant in [14] with machine power per pole is illustrated in Figure 1.6(b).

The use of rotor tangential stress, σ_{tan}, to calculate the D^2L is discussed in [12] and [14]. In [12], a wide range for σ_{tan} is given, and with the estimated electromagnetic torque produced by the machine, the D^2L is calculated. In [14] however, σ_{tan} is calculated using selected air gap flux densities $\hat{B}_g$ (magnetic loading) and the electric loading, A. The rotor tangential stress is used to calculate the D^2L of a 2.5 MW DFIG example in [16]. In [15], the analytical equation for the loading distribution method which uses B_g and A to calculate the D^2L is developed.

An aspect ratio, λ, is commonly used to split the D^2L into its component air-gap diameter, D, and machine stack length, L. In [12], a range of 1.2 - 1.8 is given for the stack aspect ratio, λ, of 4 pole machines, while a single ratio value, which is estimated using the number of poles in the machine, is used to split the D^2L in [14]. In [12], $\lambda = 1.5$ for a 5.5 kW induction motor example, and $\lambda = 1.1$ for a 736 kW (1000 HP) motor example. In [16], $\lambda \approx 1.3$ for a 2.5 MW DFIG example, while for a 7.5 kW induction motor example in [15], $\lambda = 1$.

Lower aspect ratios are recommended for low speed machines in [15], while a purported reduction of winding losses and shortening of end winding connections is obtainable with longer stacks (higher λ) [12]. In [19], different ranges for λ are given for different design outcomes as follows:

1. For good power factor	1.0 to 1.3
2. For good overall design	1.0 to 1.1
3. For good efficiency	1.4 to 1.6
4. For minimum overall cost	1.5 to 2.0

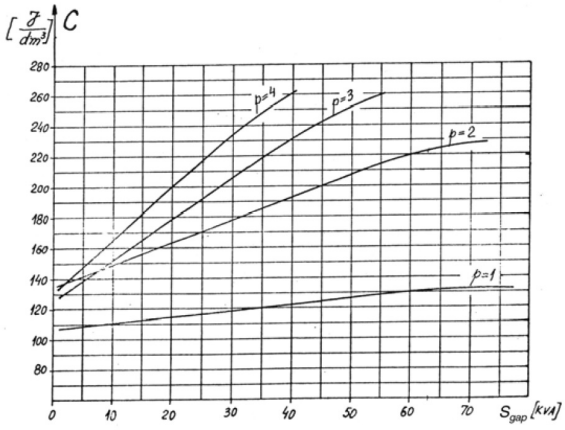

(a)

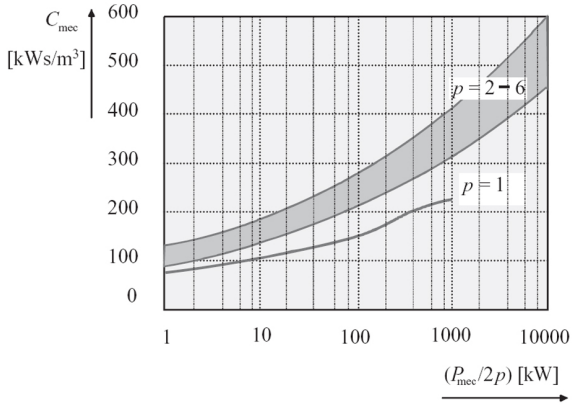

(b)

Figure 1.6: (a) Essons constant C vs air-gap apparent power S_{gap} for machines with different number of pole pairs p [12] (b) Machine constants as a function of power per pole [14].

1.2.2 The rotor-tied DFIG design and performance

A new DFIG topology (the rotor-tied DFIG) was proposed in [20, 21], whereby the rotor windings of the generator are connected directly to the grid and the stator windings via power converters. The reason for this topology was to increase the torque density and efficiency of DFIGs. A comparison of the conventional DFIG topology with the rotor-tied DFIG is illustrated in Figure 1.7.

Induction machine (or DFIG) designs start with the sizing of the stator inner diameter, and in order to maximize the torque output of induction machines or conventional DFIGs, these stator inner diameters are usually large. It was argued in [20, 21] that the largely sized stator bores give rise to over-sized rotors. Also, stating that if the grid was connected to the rotor windings, and the machine design started with the rotor design, then smaller machines could be obtained.

Following this, a couple of 5.5 kW DFIGs were designed in [20, 21]; One for conventional DFIG operation, while the other for the rotor-tied operation as illustrated in Figure 1.8. The DFIG designed for the rotor-tied configuration was smaller than the conventional DFIG, with the weight of the rotor-tied machine being 14.1% less than the conventional machine.

Similar number of turns per phase were used for the corresponding primary and secondary sides of the DFIGs in [20, 21] for fair comparisons. Finite element analysis (FEA) was performed on the conventional and rotor-tied designs in the motoring mode and the rotor-tied DFIG torque per weight was higher than the conventional DFIG by 16.6%. A prototype of the rotor-tied machine was built and tested as a motor, and the experimental results matched the FEA results.

A shape optimization was performed on the initial rotor-tied DFIG design in [20, 21], using a genetic algorithm to maximize the torque per weight in [22]. An approximate model of the FEA model was developed with the Kriging method based on the latin hypercube sampling and used in place of the FEA model for the optimization to reduce execution time. The optimization was performed by using the slot dimensions of the rotor-tied machine as optimization variables. The efficiency of the machine was used as a constraint in the optimization, as drastic reduction in size of the machine could compromise performance.

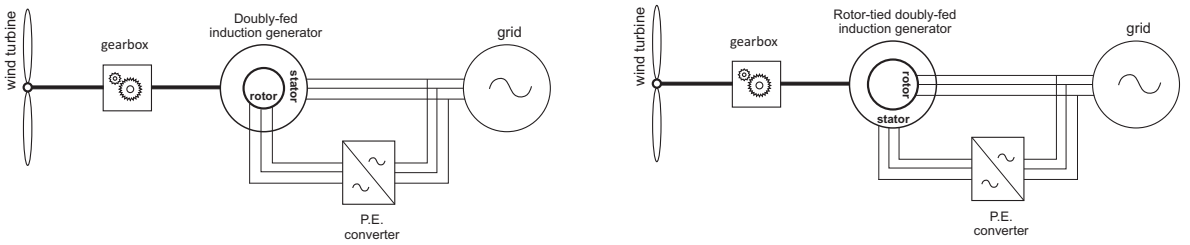

Figure 1.7: DFIG configurations: (a) conventional DFIG (b) rotor-tied DFIG.

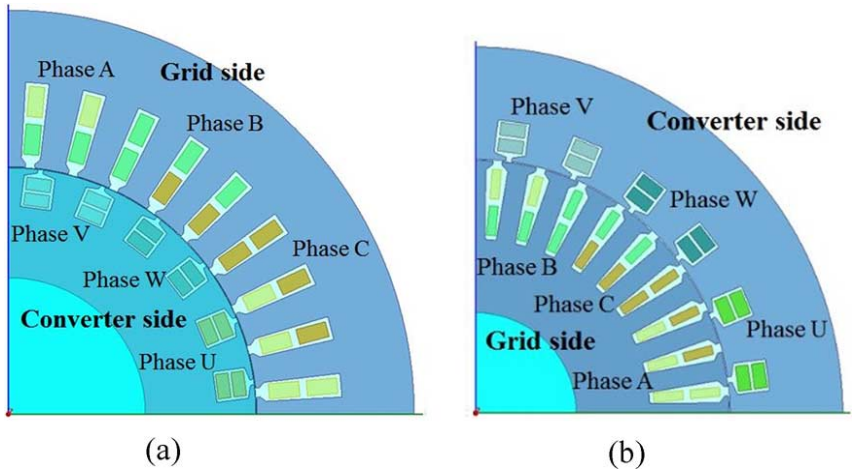

Figure 1.8: DFIG designs (a) Conventional (b) Rotor-tied

The optimized rotor-tied machine in [22] was tested as a generator, however the output was connected to a rectifier and the total DC power output was examined. The torque per weight of the optimized rotor-tied DFIG design was 4.2% greater than the initial design.

Calculations using equivalent circuit parameters in [23], project a 0.5 - 1 % order in energy savings for already conventionally designed machines connected in the rotor-tied configuration. In [24], a 7.5 kW wound rotor induction machine was used as a DFIG and tested in the conventional and rotor-tied configurations. The results obtained in [24] validated the calculations done in [23].

For the control of the rotor-tied DFIG, similar fractionally rated converters functioning the same way as in conventional DFIGs are required. As a result, there is no extra complexity with this topology [23].

1.2.3 The rotor-tied DFIG mode of operation and equivalent circuit

In [23], the operating mode of the rotor-tied DFIG was described according to the mechanical speed of rotation, slip and power flow. A method of calculating the rotor-tied DFIG slip was also given, however, the rotor is taken as the secondary side of the DFIG, and the stator as the primary side. As such, the illustration of the rotor-tied DFIG slip appeared significantly different from conventional DFIG slip, which can introduce difficulties in interpreting the slip curve of the rotor-tied DFIG. A core loss estimation model for rotor-tied DFIGs was also developed in [23].

In the different literature dealing with rotor-tied DFIGs [20–24], the equivalent circuit of the rotor-tied DFIG is not described. In [9], a steady state transformer model based equivalent circuit for conventional DFIGs is described. The phasors for the conventional DFIGs are also given for some operating conditions in [9, 16].

1.2.4 The rotor-tied DFIG and rotary transformers

DFIG systems frequently have their reliability compromised by slip ring and brush assembly which are prone to failures, and in tackling this, different approaches have been considered. One approach is the design of a brushless DFIG [7, 25], while another is the

replacement of the slip ring and brush assembly with a rotary transformer. Rotor-tied DFIGs may be more suitable for the rotrary transformers, as the higher frequency (grid frequency) windings being on the rotor of rotor-tied DFIGs, can help reduce the size of the rotary transformers [26].

1.2.5 Harmonic analysis of DFIGs

The switching techniques employed by back-to-back converters used in DFIGs to generate quasi-sine ac voltages also generate harmonic components in the rotor current. These rotor current harmonic components then induce corresponding harmonic components in the stator windings [27]. In [28], it is also observed that pulsating torque caused by low frequency rotor harmonics can induce speed pulsations depending on the inertia of the machine. These pulsations can consequently cause significant change in the stator current spectrum.

Harmonics are present in the stator current even if a purely sinusoidal voltage source is used on the rotor. The non-sinusoidal distribution of the windings in a DFIG give rise to MMF space harmonics in the machine air-gap. An additional source of harmonics in the machine air-gap are the slot harmonics. Slot harmonics are due to non-uniformity of reluctance due to the slots. Every time the air-gap magnetic field passes across a slot, slot harmonics are produced which induce harmonic voltages in the stator and rotor windings [11].

From a design point of view, increasing the number of slots per pole per phase can be used to increase the number of mmf steps, consequently reducing the harmonics due to the windings. The use of fractional coil pitches in the windings can also lead to decreased harmonic content due to the windings [12, 16]. The use of different filtering techniques have also been investigated to mitigate harmonics in DFIGs from a control standpoint [11, 27, 28].

1.2.6 Testing DFIGs without a control system

In [29], a DFIG prototype is tested without a control system, and prototype was tested as a motor with the torque evaluated. The tests described were similar to standard induction motor tests, with a no-load test and tests at 50 %, 75 % & 100 % of the rated load conducted. In [20, 21], as earlier mentioned, the rotor-tied DFIG prototype was tested as a motor and the developed electromagnetic torque was evaluated. In [22], the rotor-tied DFIG prototype rotor was connected to a rectifier bridge and a voltage at 60 Hz was supplied to the stator and the performance of the machine was evaluated.

1.3 Problem statement

Rotor-tied DFIGs have been shown to have higher efficiencies than conventional DFIGs in [20, 21]. Further investigation into the rotor-tied DFIG mode of operation described in [23] is needed to clearly compare with conventional DFIGs. The available design methodology in [20, 21] supposedly starts with the sizing of the rotor but this process is not clearly outlined. The available design methodology also does not consider all

the necessary performances evaluated in AC generators. Some design aspects specifically relevant to DFIG designs and consequent performances are therefore missing in the design process. Testing of DFIG prototypes as motors or with their output connected to rectifier bridges have some merit, but do not capture the full performance of a DFIG.

Harmonics in DFIGs are generally mitigated by winding techniques and the use of filters alongside the control system. Slot harmonics in DFIG designs may be reduced before filtering is even considered, and this needs investigation.

1.4 Research Objectives

The following objectives are considered in this research project:

- Describe in detail the steady state operation of rotor-tied DFIGs
- Describe a detailed design process for rotor-tied DFIGs.
- Evaluate the effects of different design parameters on the performance of rotor-tied DFIGs.
- Design a 5.5 kW rotor-tied DFIG following the described design process. Evaluate the performance of the designed rotor-tied DFIG with FEA and optimize.
- Construct and test a prototype of the optimized design.

1.5 Thesis Layout

Chapter 1 is an introduction and the rest of this thesis is outlined as follows:

- In **Chapter 2**, the steady state operation of a rotor-tied DFIG is described. The description includes the mode of operation and power flow of rotor-tied DFIGs in terms of the rotor and stator frequencies, the rotor mechanical speed and slip. The equivalent circuit of rotor-tied DFIGs is also detailed.
- In **Chapter 3**, a comprehensive design process for rotor-tied DFIGs is discussed.
- In **Chapter 4**, different design input parameters are investigated to evaluate their influence on the performance of rotor-tied and conventional DFIGs.
- In **Chapter 5**, the design process described in Chapter 3 is used to design a 5.5 kW rotor-tied DFIG. FEA is performed on the initial design to evaluate performance, and an optimization is also performed.
- In **Chapter 6**, the prototyping of the optimized design is described. The test bench for the prototype is also discussed.
- In **Chapter 7**, tests conducted on the prototype are described with important results highlighted.
- In **Chapter 8**, the conclusions of the study are stated alongside recommendations for future research work.

Chapter 2

The Steady State Operation of a Rotor-tied Doubly fed Induction Generator

In this chapter, the slip in a conventional DFIG is first discussed and illustrated. Equations estimating the stator and rotor power in reference to the input mechanical power of conventional DFIGs at different slips are then developed. The method of calculating the rotor-tied DFIG slip presented in [23] is discussed. The rotor-tied DFIG slip plot illustration in [23] is clearly described, and the equations given for the rotor and stator power in reference to the input mechanical power are used to categorize the different regions of operation.

An alternative method of calculating the rotor-tied DFIG slip is presented alongside alternative rotor and stator power calculations in reference to the input mechanical power. The alternative slip calculation method is developed so the rotor-tied DFIG slip matches the conventional DFIG slip at the same mechanical rotational speed. The transformer model based equivalent circuit of rotor-tied DFIGs is also illustrated.

2.1 Slip and power equations in a conventional DFIG

The relationship between the stator electrical frequency, ω_s, rotor electrical frequency, ω_r, and the rotor mechanical angular frequency, ω_m, in a conventional DFIG is given as:

$$\omega_s = \omega_r + \omega_m. \tag{2.1}$$

The mechanical angular frequency, ω_m, is calculated from the mechanical rotational speed, Ω_m, as follows:

$$\omega_m = p_1 \Omega_m, \tag{2.2}$$

where, p_1 is the number of pole pairs in the machine.

The machine slip, s, is then calculated as follows:

$$s = \frac{\omega_r}{\omega_s} = \frac{\omega_s - \omega_m}{\omega_s}. \tag{2.3}$$

The variation of slip with speed in a conventional DFIG is illustrated in Figure 2.1. When $s = 0$, the machine speed is at synchronous speed. The machine is not rotating when $s = 1$, and is rotating at a speed twice the synchronous speed at $s = -1$.

The relationship between the stator power P_s, supplied to the grid, the rotor power, P_r, absorbed or supplied to the grid and the mechanical power, P_m, supplied by a wind turbine to the generator shaft is given as:

$$P_m = P_s + P_r. \tag{2.4}$$

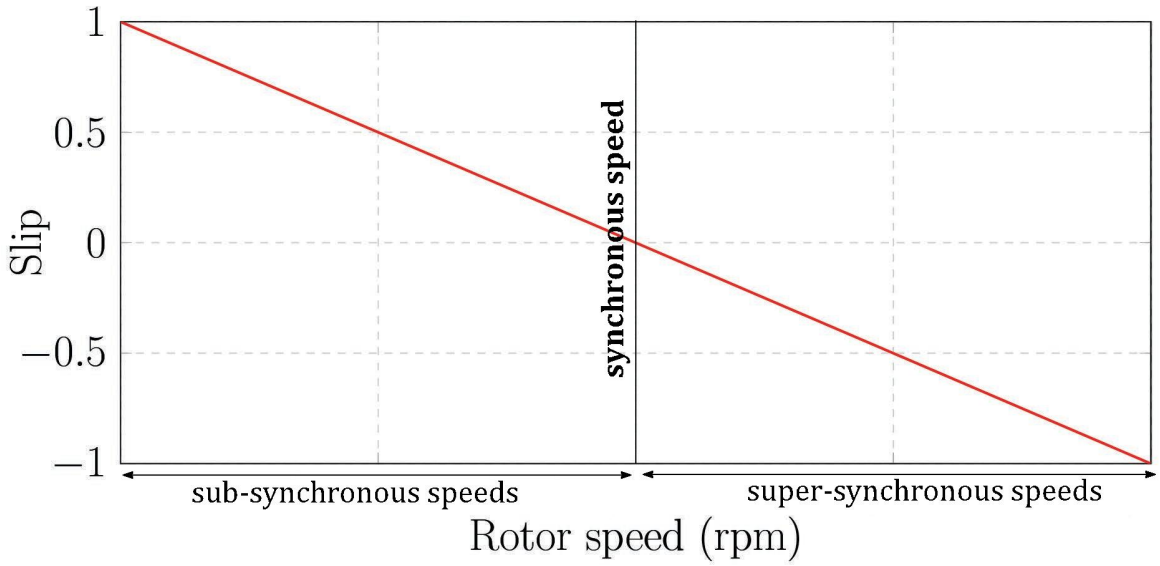

Figure 2.1: Conventional DFIG slip plot.

P_r is calculated as:

$$P_r = P_m - P_s = T_m\omega_m - T_{em}\omega_s, \tag{2.5}$$

where, T_m is the mechanical torque at the shaft, and T_{em} is the electromagnetic torque developed by the machine. Assuming a lossless DFIG system:

$$T_m = T_{em}. \tag{2.6}$$

Therefore, P_r is further obtained as [30, 31]:

$$P_r = T_m(\omega_m - \omega_s) = -T_m(s\omega_s) = -sP_s. \tag{2.7}$$

Similarly, P_s is obtained as follows [8, 30]:

$$P_m = -sP_s + P_s = (1-s)P_s, \tag{2.8}$$

$$P_s = \frac{P_m}{1-s}. \tag{2.9}$$

Combining equations (2.7) & (2.9), P_r is then calculated in terms of P_m as [30]:

$$\frac{P_r}{-s} = \frac{P_m}{1-s}, \qquad P_r = \frac{-sP_m}{1-s}. \tag{2.10}$$

2.2 Slip and power equations in a rotor-tied DFIG

From a transformer model view point, rotor-tied DFIGs have their rotors as the primary side and stators as the secondary side. Although rotor-tied and conventional DFIGs ultimately perform the same functions in a wind turbine, they are operated slightly differently.

For conventional DFIGs, the rotor is rotated mechanically in the same direction as the stator and rotor magnetic fields as portrayed in Figure 2.2(a) [9], while as shown in Figure 2.2(b), the rotor in a rotor-tied DFIG is rotated mechanically opposite in direction to the stator and rotor magnetic fields. The electromagnetic torque is in the same direction as the stator and rotor magnetic fields for a rotor-tied DFIG, while the torque in the opposite direction to the magnetic fields in conventional DFIGs.

The rotor-tied machine works in a motoring mode when rotated mechanically in the same direction as the magnetic fields. To produce an electromagnetic torque in this mode, a higher frequency than the grid frequency is needed on the stator with the rotor still having grid frequency. The stator absorbs power which is equal to the sum of the mechanical power output and rotor power output.

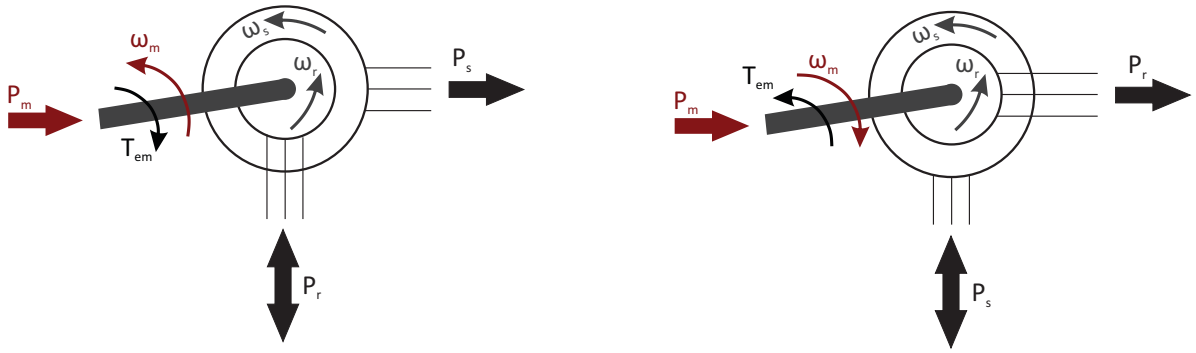

Figure 2.2: (a) Conventional DFIG operation (b) Rotor-tied DFIG operation.

2.2.1 Initial rotor-tied DFIG slip and power equations

The slip in [23] is calculated using the conventional method, and for a 60 Hz system, it is given as:

$$s = \frac{\omega_r}{\omega_s} = \frac{\omega_s - \omega_m}{\omega_s} = \frac{2\pi 60}{\omega_m + 2\pi 60}. \tag{2.11}$$

This is calculated considering that the rotor was rotating mechanically opposite to the electrical fields on the rotor and stator. Having a negative magnitude, ω_m then adds up with ω_s (the slip frequency in this case) to give the grid angular speed ($2\pi 60$).

The equations for P_r and P_s in [23] for the rotor-tied DFIG are obtained by assigning negative polarities to the conventional DFIG calculations as shown respectively:

$$P_r = \frac{sP_m}{1-s}, \tag{2.12}$$

$$P_s = -\frac{P_m}{1-s}. \tag{2.13}$$

A slip plot with regards to the mechanical rotational speed obtained using equation (2.11) is illustrated in Figure 2.3. The slip illustrations in Figure 2.3 appear significantly different from the illustration of a conventional DFIG slip in Figure 2.1.

In describing Figure 2.3 from left to right, four slip regions of operation can be identified: (a) the super-synchronous region, $0 > s > -\infty$, (b) the synchronous region, $s = \pm\infty$, (c) the sub-synchronous region, $+\infty > s \geq 1$ & (d) forward rotation region, $1 > s > 0$ [23]. Regions (a) - (c) are generating regions of operations while region (d) is a motoring region.

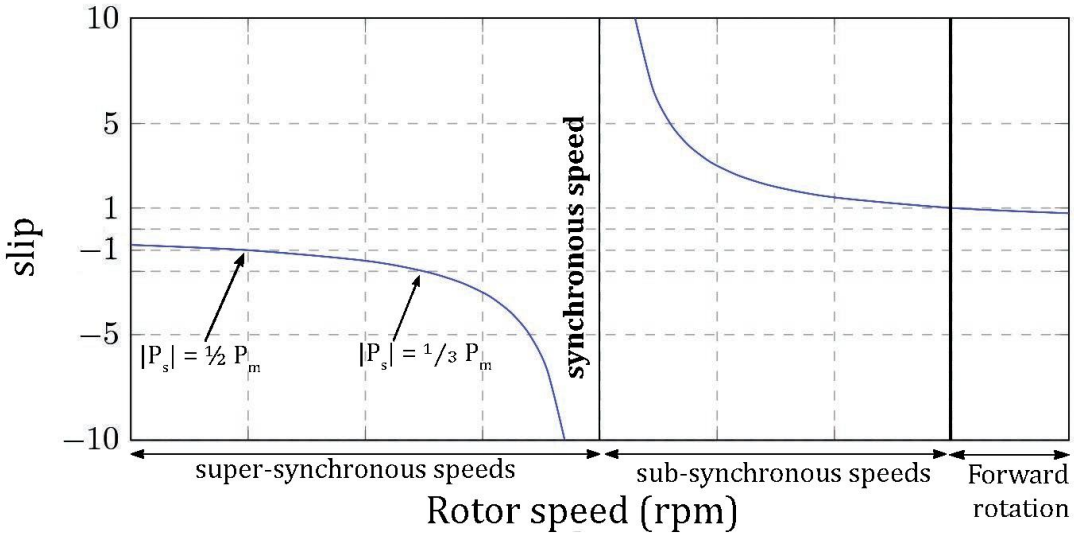

Figure 2.3: Initial rotor-tied DFIG slip plot [23].

(a) Super-synchronous region

At $0 > s > -\infty$ the rotor-tied DFIG is in the super-synchronous region in which both the stator and rotor are supplying power to the grid. Examples of the proportion of stator power to the input power from the turbine at certain slip instances are illustrated in Figure 2.3. At a slip of -1, P_s is half of the mechanical input power, P_m, and P_s is a third of the mechanical input power, P_m, at a slip of -2. Slip only tends towards but never equals zero with increasing speed. It will be noticed that at negative slips, the power of the stator is negative signifying that power is supplied to grid.

(b) Synchronous region

When the machine is rotating at synchronous speed (given the negative magnitude of the mechanical rotation), it can be seen using equation 2.11 that slip tends to infinity. Although, for a given machine, the synchronous speed is a single value, the notation $s = \pm\infty$ is based on the slip plot illustrated in Figure 2.3 depending on the direction of slip change. Using equation (2.13), it is seen that at a slip value of $\pm\infty$, P_s tends to zero, while $P_r \approx -P_m$, indicating that the stator neither absorbs nor supplies power.

(c) Sub-synchronous region

At $+\infty > s > 1$, the machine is rotating at a speed lower than the synchronous speed. In this region the stator power and the input mechanical power add up to make the rotor power. Taking a slip instance of 5, $P_s = \frac{P_m}{4}$, using equation (2.13), while $P_r = \frac{-5P_m}{4}$ using equation (2.12). The positive value of P_s with respect to P_m indicates that power is absorbed from the grid by the stator in this region. At a slip of 1, both P_r and P_s tend to zero as the machine not rotating.

(d) Forward rotation region

At $1 > s > 0$, the rotor-tied DFIG rotates in the forward direction (same direction as the magnetic fields). In this region, the mechanical rotation has a positive magnitude and this leads to a fractional positive slip value. In this region, the stator frequency field is higher than the rotor (grid) frequency and the machine rotates in a forward direction. At a slip of say 0.5, P_s is twice the mechanical power, P_m, while $P_r = P_m$. The power flow direction changes in this region, with the mechanical and rotor power leaving the machine, while the stator absorbs power from the grid into the machine. This region is however not of interest in this research, as it is a motoring region.

2.2.2 Alternative slip and power equations for a rotor-tied DFIG

Taking note of the opposite direction of mechanical rotation (with regards to convention) as shown in Figure 2.2(b), the rotor mechanical angular frequency, ω_m, has a negative magnitude with respect to the rotor electrical rotation. Therefore the relationship between the stator electrical frequency, ω_s, rotor electrical frequency, ω_r, and the rotor mechanical angular frequency, ω_m, for the rotor-tied DFIG is given as:

$$\omega_s = \omega_r - \omega_m. \tag{2.14}$$

It should be noted the rotor electrical frequency, ω_r, is the synchronous speed. For ease of calculation, slip, s, will be defined with reference to the rotor such that:

$$s = \frac{\omega_s}{\omega_r} = \frac{\omega_r - \omega_m}{\omega_r}. \tag{2.15}$$

Calculating slip this way yields rotor-tied DFIG slip values which exactly match conventional DFIG slip values at different speeds. The slip variation with rotor mechanical speed obtained using equation (2.15) is illustrated in Figure 2.4. Similar to a conventional DFIG, at a slip of -1, the machine is rotating at a speed twice the synchronous speed. The machine rotates at synchronous speed at a slip of zero, while the speed is zero at a slip of 1. At slips higher than 1, the machine is in the forward rotation mode.

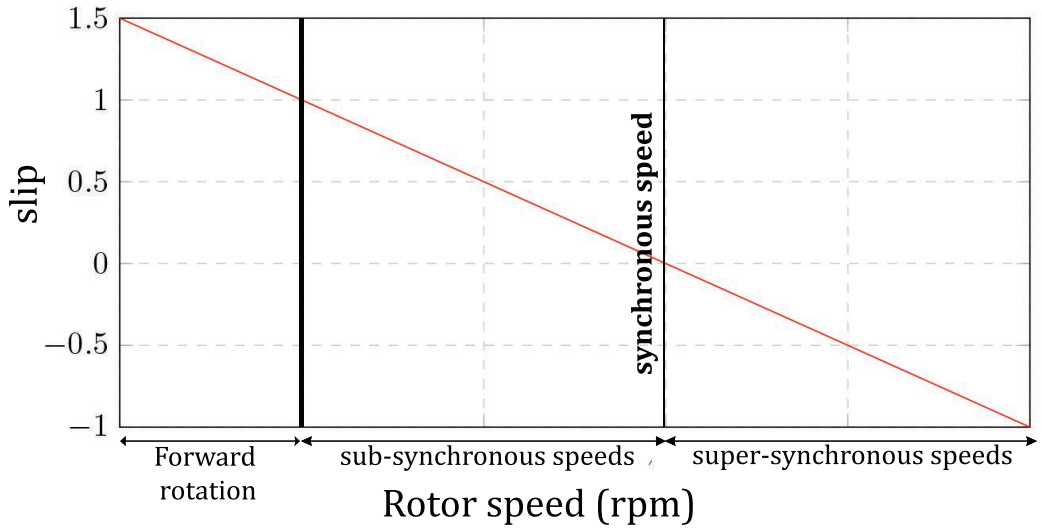

Figure 2.4: Proposed rotor-tied DFIG slip plot.

P_r and P_s with respect to P_m are calculated in a similar way as for conventional DFIGs. Regarding the change in reference of slip calculations, the rotor-tied DFIG rotor power, P_r, is similar to the conventional DFIG stator power, P_s, and vice versa. The equations for P_r & P_s in relation to P_m respectively are given as:

$$P_r = \frac{P_m}{1-s}, \tag{2.16}$$

$$P_s = \frac{-sP_m}{1-s}. \tag{2.17}$$

As is with the conventional DFIG power equations in section 2.1, a positive P_r/P_s value indicates generation. To have the same power references as in section 2.2.1, the equations of P_r and P_s can also be assigned negative polarities which yield:

$$\begin{aligned} P_r &= \frac{-P_m}{1-s}, \\ P_s &= \frac{sP_m}{1-s}. \end{aligned} \tag{2.18}$$

The proportion of the rotor and stator power to the total input mechanical power at different slip values is illustrated in Figure 2.5. For convenience, equation (2.18) is used for the calculations in the plot, therefore, the negative magnitudes indicate power generation to the grid. Noting that back-to back converters in DFIGs are usually fractionally rated with respect to the input mechanical power, P_m, DFIGs are commonly operated within a slip range of about $\pm$ 0.3. Given that the speeds at which wind turbines supply rated mechanical power to DFIGs correspond to a negative slip value [30, 32], the stator power of a rotor-tied DFIG, P_s, at a slip of -0.3 is approximately -0.23P_m.

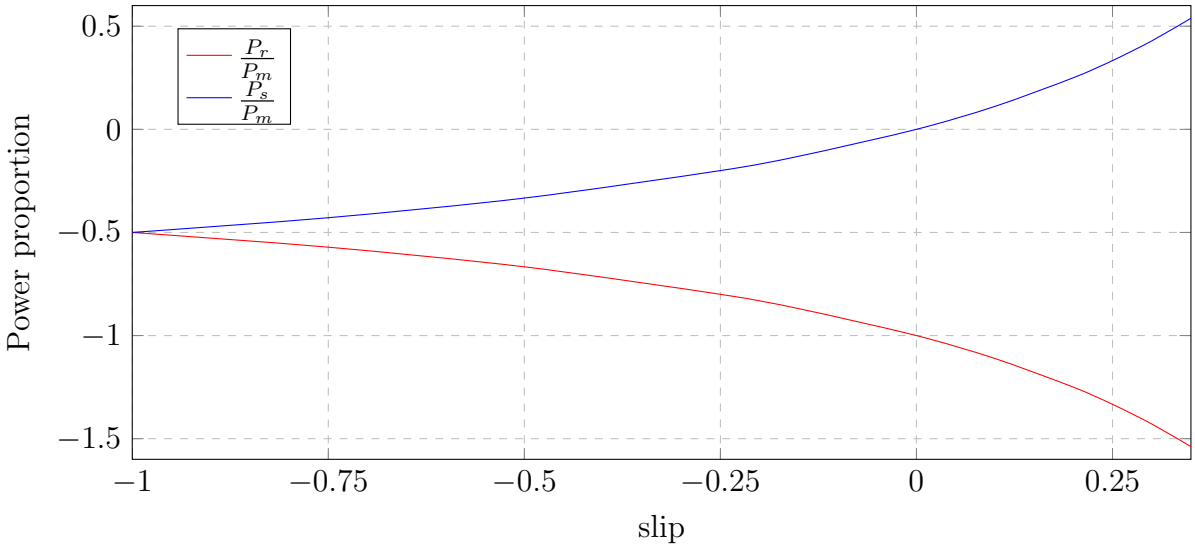

Figure 2.5: Proportion of rotor and stator power to the input mechanical power vs slip.

2.3 Equivalent circuit

With the alternative slip equations developed in section (2.2), the equivalent circuit of a rotor-tied DFIG can be obtained in a similar way to that of a conventional DFIG (or induction machine) given in [9, 16], which are based on the phase model of a transformer. Assuming that the stator and rotor are star connected with core losses neglected, the per phase equivalent circuit of a rotor-tied DFIG is shown in Figure 2.6. Rated grid voltage at grid frequency is applied to the rotor while the stator is supplied through a back-to-back converter at slip frequency.

2.3.1 Voltage Equations

From the circuit in Figure (2.6), the following voltage equations can be obtained:

$$\underline{V}_r - \underline{E}_r = (R_r + X_{lr})\underline{I}_r \quad \text{at rotor/grid frequency, } f_r, \tag{2.19}$$

$$\underline{V}_s - \underline{E}_s = (R_s + X_{ls})\underline{I}_s \quad \text{at stator frequency, } f_s, \tag{2.20}$$

where, $\underline{V}$ represents the supplied voltages, $\underline{E}$, the induced voltages, $\underline{I}$, current, R, the winding resistances (details are given in section A.1), and X_l the leakage reactances (details in A.2). The subscripts $(_r)$ and $(_s)$ represent the rotor and stator parameters respectively.

With the stator side of Figure 2.6 referred to the rotor side as shown in the circuit in Figure (2.7), the voltage equations can be re-written as:

$$\frac{\underline{V}'_s}{s} - \underline{E}_r = \left(\frac{R'_s}{s} + jX'_{ls}\right)\underline{I}'_s \quad \text{at } f_r, \tag{2.21}$$

$$\underline{V}_r - \frac{\underline{V}'_s}{s} - (R_r + jX_{lr})\underline{I}_r + (\frac{R_s}{s} + jX_{ls})\underline{I}'_s = 0 \quad \text{at } f_r, \tag{2.22}$$

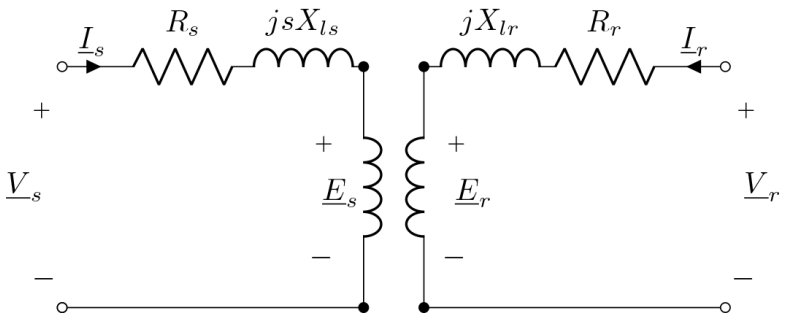

Figure 2.6: DFIG steady state phase equivalent circuit with the different frequencies on the rotor and stator.

where, the ($'$) notation signifies the stator parameters referred to the rotor side (details are given in section B.1).

The emf induced in the rotor windings is:

$$\underline{E}_r = jX_m(\underline{I}_r + \underline{I}'_s) \quad \text{at } f_r, \tag{2.23}$$

where, X_m is the magnetizing reactance (details in A.11).

2.3.2 Flux Linkages

The rotor and stator fluxes are given by:

$$\underline{\Psi}_r = L_m(\underline{I}_r + \underline{I}'_s) + L_{lr}\underline{I}_r = L_r\underline{I}_r + L_m\underline{I}'_s, \tag{2.24}$$

$$\underline{\Psi}'_s = L_m(\underline{I}'_s + \underline{I}_r) + L'_{ls}\underline{I}'_s = L_s\underline{I}'_s + L_m\underline{I}_r, \tag{2.25}$$

where, $L_{r,s}$ are the rotor and stator inductances respectively given as:

$$\begin{aligned} L_r &= L_m + L_{lr}, \\ L_s &= L_m + L'_{ls}. \end{aligned} \tag{2.26}$$

Then, the voltage equations can be further simplified to become:

$$\underline{V}_r - R_r\underline{I}_r = j\omega_r\underline{\Psi}_r, \tag{2.27}$$

$$\underline{V}'_s - R_s\underline{I}'_s = js\omega_r\underline{\Psi}'_s. \tag{2.28}$$

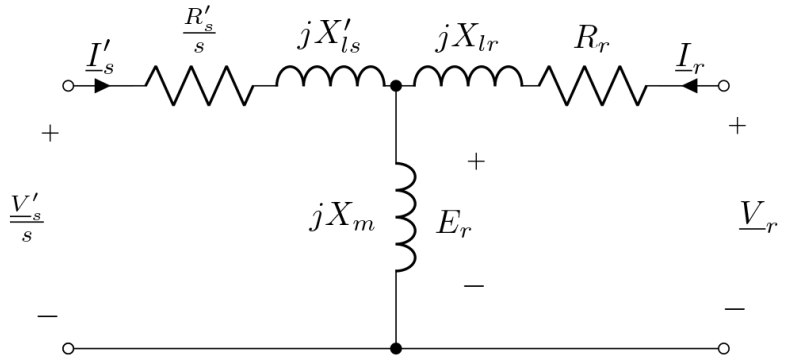

Figure 2.7: DFIG steady state phase equivalent circuit with the stator reffered to the rotor side.

2.3.3 Phasor diagrams

The equivalent circuit equations can be used to estimate the rotor-tied DFIG steady state values of the rotor and stator fluxes, current and voltages at specific grid side conditions, all with their angles. Since the grid voltage of the machine is known, alongside the power rating, the rotor current can also be easily deduced. The rotor current is deduced from the equation of the active power P_r, of the rotor side as:

$$P_r = 3Re\{\underline{V}_r \cdot \underline{I}_r{}^*\}. \tag{2.29}$$

The reactive power absorbed or supplied by the rotor Q_r, is given as:

$$Q_r = 3Im\{\underline{V}_r \cdot \underline{I}_r{}^*\}. \tag{2.30}$$

With equation (2.27), the rotor flux at a specific rotor power factor (which determines the current angle) can be obtained. The stator current is then calculated using equation (2.24) from which the stator flux is deduced from equation (2.25). Once all these have been obtained, the stator voltage referred to the rotor side is calculated using equation (2.28). These quantities can be represented with phasor diagrams upon calculation as illustrated in Figure 2.10.

Motoring and generating operations

A distinction between the motoring and generating modes of the rotor-tied DFIM operation is the relative position of the rotor and the stator fluxes. If $\underline{\Psi}_r$ leads $\underline{\Psi}'_s$, the machine is operating within a motoring region and the opposite for a generating region [9]. At lagging power factors(rotor reactive power, $Q_r > 0$), $\underline{I}_r$ makes an angle varying from -90^0 to -180^0 as the power factor increases, while at leading power factor ($Q_r < 0$), the angle varies from +90^0 to +180^0. It should be noted however that -180^0 and +180^0 are the same angle, and when $\underline{I}_r$ is at this angle, the machine is supplying power at unity power factor ($Q_r = 0$) at the grid side.

General description of rotor-tied DFIG phasors

The phasors illustrated in Figure 2.10 are for rotor-tied doubly fed induction machines (DFIMs) operating as generators with the secondary side (stator) phasors referred to the rotor. Positive angle references are given in a counter-clockwise direction with $\underline{V}_r$ as the reference at 0^0 as illustrated in Figure 2.8(a).

$\underline{\Psi}_r$ and $\underline{\Psi}'_s$ are always approximately angled at 90^0 relative to their respective voltages. As can be seen from equations (2.27) & (2.28), the phase shift is caused mainly by the inductive component hence the 90^0 shift. The effect of a non-unity power factor condition is usually negligible due to the much higher voltage values. At leading power factor (at the grid side), $\underline{\Psi}'_s$ is slightly larger than $\underline{\Psi}_r$ and lower at lagging power factor. At unity power factor, $\underline{\Psi}_r$ and $\underline{\Psi}'_s$ are identical in magnitude.

Rotor-tied DFIG phasors at grid-side lagging power factor

In Figure 2.8(a), the machine has a lagging power factor at the rotor side and is rotating at a sub-synchronous speed. $\underline{V}'_s$ has a positive acute angle to the rotor voltage. $\underline{I}'_s$ varies

however from a positive acute angle at very low power factors to a negative acute angle at higher power factors.

In Figure 2.8(b), the machine also has a lagging power factor at the rotor side and is rotating at a super-synchronous speed. The major distinction to Figure 2.8(a) is the direction of $\underline{V}_s'$ which hovers around the 180^0 angle.

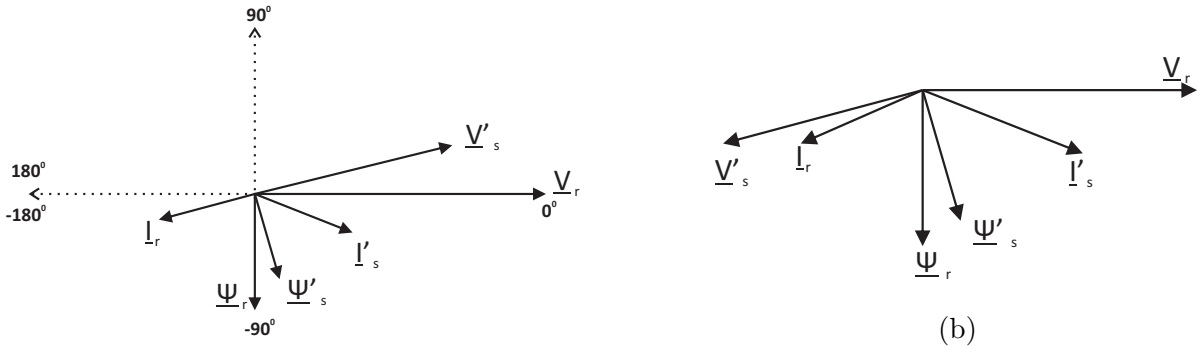

Figure 2.8: Rotor-tied DFIG Phasor diagrams: (a) $Q_r > 0$ at subsynchronous speed, (b) $Q_r > 0$ at supersynchronous speed.

Rotor-tied DFIG phasors at grid-side unity power factor

In Figures 2.9(a) & 2.9(b), the grid-side of the machine is at unity power factor and is rotating at a sub-synchronous and super-synchronous speed respectively. The distinction is the direction of $\underline{V}_s'$. At sub-synchronous speeds, $\underline{V}_s'$ is located at a very small positive acute angle to $\underline{V}_r$ with the angle increasing with increasing slip. At super-synchronous speeds, $\underline{V}_s'$ has a negative obtuse angle to $\underline{V}_r$ and the angle magnitude increases with increasing slip.

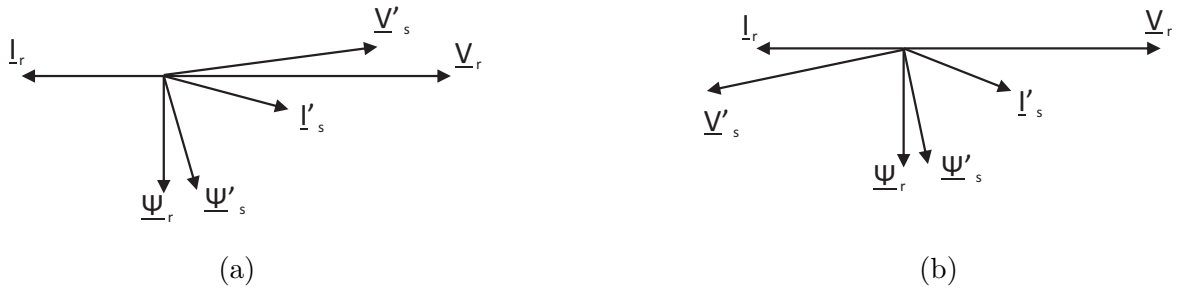

Figure 2.9: Rotor-tied DFIG Phasor diagrams: (a) $Q_r = 0$ at subsynchronous speed, (b) $Q_r = 0$ at supersynchronous speed.

Rotor-tied DFIG phasors at grid-side leading power factor

In Figures 2.10(a) & 2.10(b), the machine has a leading power factor (supplying reactive power to the grid) at sub-synchronous and super-synchronous speeds respectively. The distinction is also the position of $\underline{V}_s'$ which is similar to the machine at lagging power

factors in Figures 2.8(a) & 2.8(b). $\underline{I}'_s$ however does not have a positive angle at any point with $\underline{V}_r$ but always an acute negative angle which decreases with increasing slip.

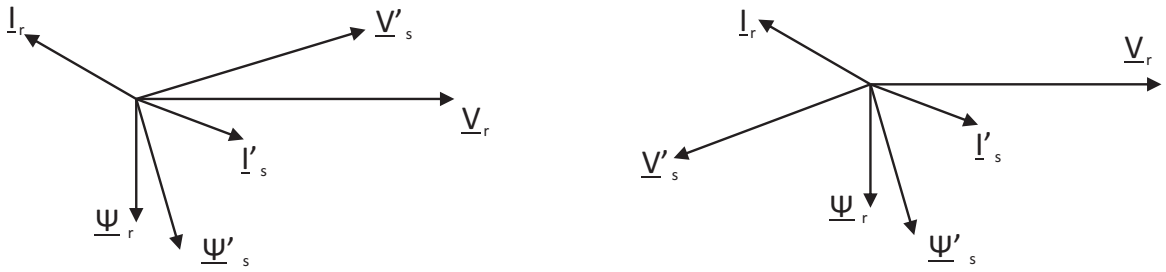

(a) (b)

Figure 2.10: Rotor-tied DFIG Phasor diagrams (a) $Q_r < 0$ at subsynchronous speed, (b) $Q_r < 0$ at supersynchronous speed.

2.4 Summary

The operations of rotor-tied DFIGs are detailed in this chapter and the major subjects discussed are listed as follows:

- The difference in operations of rotor-tied and conventional DFIGs in wind turbines.
- An alternative method for calculating the rotor-tied DFIG slip to the one given in [23].
- The proportion of converter power and rotor power to the input mechanical power in rotor-tied DFIGs based on slip.
- The per-phase transformer model equivalent circuit of the rotor-tied DFIG.
- Phasor diagrams of the rotor-tied DFIG at different operating points.

Chapter 3

The Rotor-tied DFIG Design Process

In this chapter, the design aspects of rotor-tied DFIGs are comprehensively discussed. Design considerations are given alongside analytical equations for calculating machine design parameters. The considerations are centered around obtaining rotor-tied DFIGs with high power densities and favourable qualities like high efficiency, high power factor, low voltage and current harmonics.

First, the rotor-tied design process in [20, 21] is briefly discussed. Then, a comprehensive design process, which is obtained from a blend of elements of the standard DFIG process described in [16] and the design process in [20,21], is presented. The adaptability for small DFIGs, of certain design aspects which are not covered in [20, 21], and are only discussed for large machines in [16], are discussed. These include the calculations of the rotor slot dimensions and the stator winding parameters. The initial rotor sizing is developed analytically from the flux in a single turn coil as done in [15] and other analytical equations at the different design stages are given.

The use finite element analysis (FEA) to evaluate the performance of rotor-tied DFIGs is discussed. The analytical design process and equations may not cater to certain strategic and essential performances, hence a way of optimizing designs is also discussed.

3.1 Initial rotor-tied DFIG design process

The design procedure of rotor-tied DFIGs described in [20,21] begins with the rotor sizing after the determination of design specifications. Although in [21], it is stated that the rotor-tied DFIG rotor size is calculated using electric and magnetic loadings, the analytical formula used to determine the rotor size is not provided in either [20] or [21].

Upon calculating the rotor size (outer diameter and stack length), the flux per pole is determined using the stack length, pole pitch and air-gap flux density. With the flux per pole calculated, the number of rotor turns per phase is calculated with the rated grid voltage. In [20], the full-load current for the rotor is determined from the rated input power and voltage. The full-load current with a selected current density, is then used to calculate the cross-sectional area of conductors used in the rotor. With the conductor area and a chosen fill factor, the slot and teeth dimensions are calculated, after which the rotor inner diameter is then determined. The analytical equations for calculating the slot and core dimensions are not given.

The stator is designed after all the rotor parameters have been determined. A convenient turns ratio between the rotor turns per phase and the stator turns per phase is selected from which the number of turns per phase in the stator is determined. From the stator turns per phase, the induced emf per stator phase is calculated. Using the already selected turns ratio and winding factors of the rotor and stator, the current in the stator windings

is determined. An estimated ratio of the stator mmf to rotor mmf, K_i, is also used in the calculation of the stator current. The stator current is used to calculate the stator conductor cross-sectional area using the selected current density as is done with the rotor, after which the stator slot and core dimensions are determined. The summary of the complete design process of rotor-tied DFIGs described in [20, 21] is illustrated in Figure 3.1.

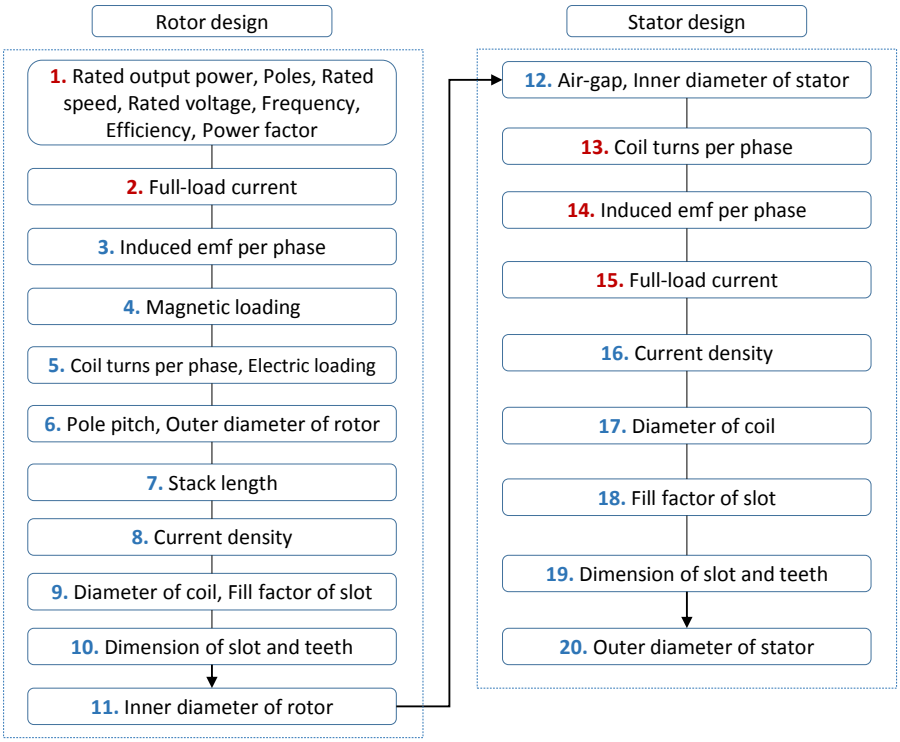

Figure 3.1: Initial rotor-tied DFIG design process [21].

3.2 Comprehensive rotor-tied DFIG design process

In this section, a thorough design process of rotor-tied DFIGs is presented. The rotor sizing process is clearly described with developed analytical equations for calculating the rotor size given. The analytical equations for all the design aspects such as the slot and core dimension calculations are provided.

The rotor-tied DFIG design begins with outlining the desired design specifications; the rated power, P_n, the rated speed, n, grid frequency, f, number of pole pairs, p_1, efficiency, η, and power factor.

After the selection of the design specifications, the stator power, P_s, and rotor power, P_r, are determined. Alongside the determination of the stator and rotor power, is the selection of the rotor and stator voltages. The rotor voltage V_r is equal to the grid voltage whereas a convenient stator voltage, V_s, is set. This is a different method to the rotor-tied DFIG design process in [20, 21], where a convenient turns ratio is selected, from which the stator voltage and current are then calculated.

The rotor size is determined using the loading distribution method. The rotor power with the magnetic and electrical loadings ($\hat{B}_g$ & A respectively) are used in the sizing. The

rotor-stator slot number combination is set before calculating the rotor size, as the rotor winding factor, K_{w1}, (calculated from the number of rotor slots per pole per phase q_1), is used in the calculation of the rotor size. After the rotor size has been determined, the (rotor then stator) winding parameters are calculated from which the slot and core dimensions are then calculated.

FEA is used to evaluate the performance of the design and the power density, power factor, efficiency, and harmonic content are highlighted as critical factors for assessment. If the efficiency and power factor of the design are lower than the desired values, the magnetic and electric loadings are modified and the rotor size is re-calculated. The teeth and core flux density values are also reviewed and the slot and core dimensions are re-calculated. After, the initial design conditions are satisfied, the design is further enhanced to increase the power density and lower the harmonic content by an optimization process.

In the following subsections, the different design aspects and choices of input design parameters are discussed. Analytical equations needed at each stage of the design process are either derived or provided.

3.2.1 Rotor and stator power

The rotor (grid side) is not expected to supply the full machine power rating as the design process in [20,21], which is illustrated in Figure 3.1 suggests. The stator supplies a percentage of the total generated power (which translates to P_s) depending on the power rating of the converter available. From the power rating of the converter, which is used as the stator power P_s, the maximum permissible negative slip is calculated using equation (2.17). Neglecting the losses in the machine, the difference between the input mechanical power P_m (the rated machine power) and the stator power is assigned as the rotor power P_r. It should be noted however, that the DFIG converter power ratings are typically only a small fraction (about a third) of the total DFIG power rating, as a large sized converter will compromise the efficiency advantage of the DFIG.

3.2.2 Rotor-stator slot number combination

Specific rotor-stator slot combinations are common with similarly rated induction machines. This is due to years of manufacturing and research experience with induction motor design. For induction motors, the slot number combinations affect factors like starting current, torque ripple and breakdown torque while slot number combinations affect harmonic content and power density in DFIGs.

Being indicative of the power quality, steps are usually taken to greatly mitigate the presence of harmonics in generators. Besides power quality issues, harmonics introduce parasitic torques in machines leading to noise and unwanted vibrations [12, 14].

Saturation in the iron parts of DFIGs (especially the teeth) sets up harmonics, so care must be taken to restrict the flux density in the machine teeth to permissible levels according to the steel lamination material in use. While higher slot numbers lead to more steps in the mmf distribution and less space field harmonic content with lower losses [12], too high a number produces thinner teeth which saturate easily. In [14], a range of 7 - 45 mm is given for induction machine slot pitches. The higher values in this range are used for larger machines.

In [12], a simple rule of rotor slots number, n_r, being different from the stator slots number, n_s, i.e., $n_r \neq n_s$, is given for wound rotor machines. Also when n_r or n_s is a multiple of the other, there is a risk of slot alignment and subsequent locking, so such combinations are avoided. The choice of combination is however further narrowed for DFIGs, which are usually constructed with integral numbers of slots per pole per phase on the rotors and stators [16].

3.2.3 Rotor sizing

The rated power or torque produced in induction machines is dependent on the size of the air-gap. The air-gap size is commonly quantified with the term D^2L, where D is the air-gap diameter, and L is the stack length of the machine. The D^2L is used as a standard output coefficient to size induction machines according to desired rated output power or torque.

The loading distribution method is commonly used to calculate the D^2L using the air-gap flux density $\hat{B}_g$, and the specific electric loading A [15]. The D^2L can also be calculated using either the Esson's constant [12] or the rotor tangential stress [14].

The D^2L calculation will be adapted to calculate the rotor size for rotor-tied DFIGs. Instead of using the air-gap power, which is the total machine rated power, the rotor power, P_r, which is determined from section 3.2.1, is used to determine the rotor size. The rotor power in the rotor-tied DFIG stays constant at the synchronous speed or higher, thus the synchronous speed is used to size the rotor.

D^2L calculation

The rotor apparent power, S_r (kVA), is given by:

$$S_r = 3E_{rph}I_{rph} \times 10^{-3}, \tag{3.1}$$

where, E_{rph} is emf induced per phase and I_{rph} is the phase current in the rotor.
From section B.1:

$$E_{rph} = 4k_f k_{wr} f_r N_r \phi_m, \tag{3.2}$$

where, k_f is the voltage form factor, k_{wr} is the rotor winding factor, f_r is the rotor frequency which is also the grid frequency, N_r is the number of rotor turns per phase and ϕ_m is the peak magnetizing flux per pole. The magnetizing flux is calculated as:

$$\phi_m = \alpha \hat{B}_g \tau_r L, \tag{3.3}$$

where, α is the flux density shape factor estimating the amount of saturation, $\hat{B}_g$ the peak air gap flux density and τ_r the rotor pole pitch [12, 13].
The variation of the form factor, k_f, and the flux density shape factor, α, with degrees of teeth saturation is illustrated in Figure 3.2 (redrawn from [12]). A teeth saturation factor k_{st} value of zero is for a purely sinusoidal voltage waveform, with increasing values representing the expected levels of saturation for choices of α and k_f.

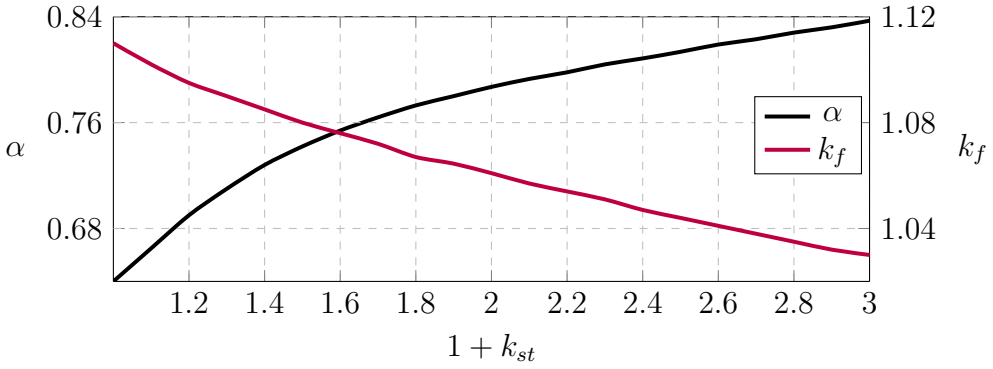

Figure 3.2: Form factor k_f and flux density shape factor α relative to teeth saturation factor [12].

Since the rotor is connected directly to the grid, a purely sinusoidal waveform is desired, thus a k_{st} value of zero is selected with consequent α and k_f values of 0.64 and 1.11 respectively. The air-gap flux density is also given as $\bar{B}_g$, which is a product of α and $\hat{B}_g$.

A recommended range for the peak air gap flux density $\hat{B}_g$ for induction machines is given as 0.7 - 0.9T in [14]. A narrower range of 0.65 - 0.78T is given for 4-pole inductions machines in [12].
The rotor pole pitch, τ_r, is calculated as:

$$\tau_r = \frac{\pi D_{ro}}{2p_1}, \tag{3.4}$$

where, D_{ro} is the outer rotor diameter and p_1 is the number of pole pairs.
The rotor frequency, f_r (Hz), relates to the design rated speed, n (rpm), and number of pole pairs, such that:

$$f_r = \frac{np_1}{60}. \tag{3.5}$$

Given the number of turns per phase in the rotor, N_r, the total number of turns in a 3-phase machine is $3N_r$. With two conductors in a turn, the rotor circumference, C_r, is used to calculate the specific electric loading, A, such that:

$$C_r = \pi D, \tag{3.6}$$

$$A = \frac{2(3N_r)I_{rph}}{C_r} = \frac{2(3N_r)}{\pi D_{ro}} I_{rph}. \tag{3.7}$$

The specific electric loading, A, is also known as the linear current loading/density [12,14], or the ampere conductors per meter [15]. A broad range of A ($\mathrm{A\,m^{-1}}$) for induction machines is given in different design books [12–15] with values spanning $5000 - 65000$ $\mathrm{A\,m^{-1}}$. In [33], the variation of the range with increase in machine power is also detailed.

The grid side phase current, I_{rph}, can then be calculated from equation (3.7) as:

$$I_{rph} = \frac{A\pi D_{ro}}{6N_r}. \tag{3.8}$$

Substituting equations (3.2), (3.3), (3.5), (3.4) & (3.8) into equation (3.1) gives:

$$\begin{aligned} S_r &= \frac{3\left[4k_f\left(\frac{np_1}{60}\right)k_{wr}N_r\bar{B}_g\left(\frac{\pi D_{ro}}{2p_1}\right)L\left(\frac{A\pi D_{ro}}{6N_r}\right)\right]}{10^3} \\ &= \frac{4k_f\pi^2}{240}k_{wr}A\bar{B}_gD_{ro}^2Ln\times 10^{-3}. \end{aligned} \tag{3.9}$$

Then, the rated rotor output power, P_r, can be calculated as:

$$P_r = S_r\eta\cos\varphi, \tag{3.10}$$

where, $\cos\varphi$ is the grid power factor and η is the machine efficiency.
Incorporating equation(3.10) into (3.9) yields:

$$\frac{P_r}{\eta\cos\varphi} = \frac{4k_f\pi^2\times 10^{-3}}{240}k_{wr}A\bar{B}_gD_{ro}^2Ln. \tag{3.11}$$

The D_{ro}^2L can then be calculated as:

$$D_{ro}^2L = \frac{240\times 10^3}{4k_f\pi^2}\frac{P_r}{\eta\cos\varphi k_{wr}nA\bar{B}_g}. \tag{3.12}$$

Stack aspect ratio

Upon determination of the D_{ro}^2L value, an aspect ratio is chosen to fragmentize this coefficient into its component rotor diameter D_{ro} and the machine stack length L. Replacing the D_{ro}^2L with the term "rotor output coefficient", O_r, the stack aspect ratio, λ, is given as:

$$\lambda = \frac{L}{\tau_r}, \tag{3.13}$$

and from equation (3.4), the aspect ratio becomes:

$$\lambda = \frac{2p_1L}{\pi D_{ro}}, \tag{3.14}$$

giving:

$$L = \frac{\lambda\pi D_{ro}}{2p_1}. \tag{3.15}$$

The output coefficient can then be given as:

$$O_r = \frac{D_{ro}^3\lambda\pi}{2p_1}, \tag{3.16}$$

from which the rotor diameter, D_{ro}, is then calculated as:

$$D_{ro} = \sqrt[3]{\frac{2p_1O_r}{\lambda\pi}}. \tag{3.17}$$

A very wide range of about 0.6 - 4 for the aspect ratio, λ, is seen in different literature [12, 13, 15, 34, 35] for various reasons . Generally, the range is narrower for small, medium speed machines (<10Kw) [15]. A range of about 0.6 - 1.8 is given in [12, 35]. Further details about the choice of aspect ratio are given in section 4.1.

Air gap length

According to the formula given in [12], the air gap length, g, can be calculated as:

$$g = (0.1 + 0.012(\sqrt[3]{P_n}))mm \tag{3.18}$$

The air gap lengths are usually standardized in values (0.25, 0.3, 0.35, 0.4....) [12].

3.2.4 Rotor and stator winding parameters

The winding parameters are calculated after determining the inner rotor diameter and stack length. The number of rotor turns per phase, N_r, and turns per slot, n_{sr}, are first determined alongside the rotor phase current, I_{rph}, from which a suitable stator phase voltage, V_{sph}, is selected and used to calculate the stator number of turns per phase, N_s, and slot, n_{ss}. The stator phase current, I_{sph}, is then estimated.

Rotor windings

Rearranging equation (3.2), the number of turns per phase in the rotor windings, N_r, is calculated as:

$$N_r = \frac{E_{rph}}{4k_f k_{wr} f_r \phi_m}, \tag{3.19}$$

where, E_{rph} is the phase voltage of rotor and k_{wr} is the rotor winding factor
The number of turns per rotor slot, n_{sr}, is obtained as follows:

$$n_{sr} = \frac{a_1 N_r}{p_1 q_r}, \tag{3.20}$$

where, a_1 is the number of current parallel paths, and q_r is the number of rotor slots per pole per phase.

Rotor current

The grid side of a DFIG is usually operated at unity power factor with the converter side supplying the machine magnetising current [9, 16]. This operational power factor, $(\cos\varphi_g)$, is different from the inherent power factor of the machine due to its magnetizing reactance $(\cos\varphi)$. The inherent machine power factor, $\cos\varphi$, is used in the rotor sizing, whereas the operational power factor, $\cos\varphi_g$, is used to calculate the actual operational rotor current. For the rotor-tied design, the rated rotor phase current, (I_{rph}, grid side) can be determined with an operational power factor $(\cos\varphi_g)$ of 0.95. This operational power factor is inspired by the EON grid code illustrated in [9], in which DFIGs can operate at a minimum of 0.95 inductive power factor. I_{rph} is calculated as:

$$I_{rph} = \frac{P_r}{3V_{rph} cos\varphi_g}, \tag{3.21}$$

Stator windings

In calculating the stator winding parameters in the initial design process illustrated in Figure 3.1, a turns ratio is selected, from which the stator voltage and current are calculated. For the proposed design process, considerations for the stator windings are started by selecting a desired induced voltage, V_{2ph}, at maximum slip. The number of stator turns per phase, N_s, is then calculated similarly to N_r in equation (3.19) assuming the same flux per pole, ϕ_m, is present at both windings.

This method takes a more basic approach than using the same voltages at both the stator and rotor windings (to eliminate the need for a transformer at the secondary side) as given in [16]. Problems arise using the method in [16] for smaller generators such that the secondary side has too many turns of wires with very small cross sections so a lower voltage than the grid voltage can be selected. It should also be noted that maximum slip frequency f_{sm} is used instead of the grid frequency. The number of stator turns per phase, N_s, is calculated as:

$$N_s = \frac{V_{sph}}{k_f k_{ws} f_{sm} \phi_m}, \tag{3.22}$$

where, k_{ws} is the stator winding factor, and f_{sm} is the maximum slip frequency.
The stator (converter) to rotor (grid) turns ratio, a_{sr}, is then calculated as:

$$a_{sr} = \frac{N_s k_{ws}}{N_r k_{wr}}. \tag{3.23}$$

It is assumed that the stator provides the magnetising current, and in calculating the rated stator current, the rotor current is first referred to the stator side as I'_{rph}. I'_{rph} is calculated as:

$$I'_{rph} = \frac{I_{rph}}{a_{sr}}. \tag{3.24}$$

The magnetising current, I_m, referred to the stator side is estimated using an assumed ratio, k_m, which is the percentage of the magnetising current to the rotor current as follows:

$$I'_m = k_m I'_{rph}. \tag{3.25}$$

The rated stator current is then determined as:

$$I_{sph} = \sqrt{I'^2_{rph} + I'^2_m} = I'_{rph}\sqrt{1 + k_m^2}. \tag{3.26}$$

Wire cross section

The rotor/stator magnetic wire cross section, A_{co}, is calculated from the rotor or stator phase current, I_{ph}, and a selected current density, J_{co}. Guidelines for selecting the current density are obtained from [12, 14]. The cross section is calculated as:

$$A_{co} = \frac{I_{ph}}{J_{co}}. \tag{3.27}$$

The wire gauge diameter, d_{co}, is given as:

$$d_{co} = \sqrt{\frac{4A_{co}}{\pi}}. \tag{3.28}$$

A condition is given in [12] such that for d_{co} values greater than 1.3 mm, a number of conductors, a_p, can be used in parallel. The new wire gauge diameter, d'_{co}, is then calculated as:

$$d'_{co} = \sqrt{\frac{4A_{co}}{\pi a_p}}. \tag{3.29}$$

3.2.5 Slot and core dimensions

Random wound conductors are commonly used in small machines. For random wound conductors, the rotor and stator slots can be designed using parallel teeth, as it affords a uniform flux density along the teeth. On the other hand, larger machines are usually wound with rectangular conductors due to the higher currents, and rectangular slots are typically used leading to non-parallel teeth.

For rectangular slots, care is usually taken such that the flux density in the minimum teeth width along the teeth length is not higher than the rated teeth flux density. With the minimum teeth width having the rated flux density value, non-parallel teeth typically take up more area than parallel teeth, leading to an increased machine size. This increase in size is negligible for large machines, but is more significant in smaller machines.

A teeth flux density range between $1.5T$ and $1.65T$ is suggested in [12]. The lower flux densities lead to higher power factors and efficiencies but also larger sized machines. Higher teeth flux densities lead to smaller machines (higher power densities) but run the risk of saturation, which can significantly reduce the power factor and efficiency, and also lead to increased harmonic content.

Calculations for trapezoidal shaped stator slot dimensions with parallel teeth are given in [12] but not for rotor slots with parallel teeth. This is also the case in other design handbooks. The method used in [12] to calculate the stator slots will be expanded, by clearly deriving the equations for calculating the slot dimensions. The method is then adapted to calculate rotor slot dimensions.

Stator slot dimensions

A trapezoidal shaped stator slot geometry is illustrated in Figures 3.3 & 3.4. In Figure 3.3, the stator slot pitch and a parallel tooth are illustrated, while different sections/dimensions of the stator slot are illustrated in Figure 3.4.

The useful slot area, A_{su}, of a slot is calculated using a practically obtainable slot fill factor, k_{fill}, as:

$$A_{su} = \frac{\pi d'^2_{co} a_p n_{ss}}{4k_{fill}}, \tag{3.30}$$

where, n_{ss} is the number of turns per stator slot. The stator pole pitch, τ_s, is calculated using the stator inner diameter, D_{si}, as:

$$\tau_s = \frac{\pi D_{si}}{2p_1}. \tag{3.31}$$

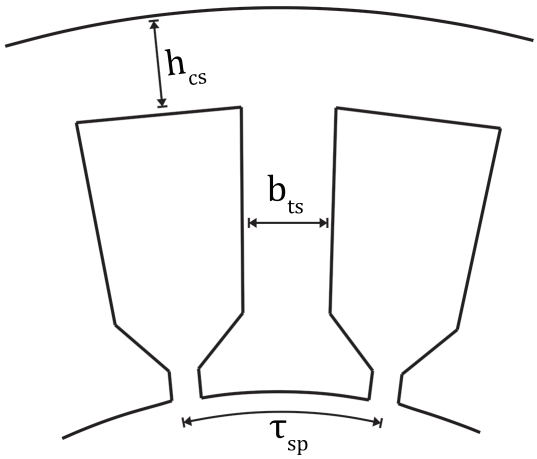

Figure 3.3: Stator slot pitch.

The stator slot pitch, τ_{sp}, is calculated using the number of stator slots per pole per phase, q_s, as:

$$\tau_{sp} = \frac{\tau_s}{3q_s}. \tag{3.32}$$

The stator teeth width, b_{ts}, is calculated as:

$$b_{ts} = \frac{\hat{B}_g \tau_{sp}}{\hat{B}_{ts} k_{fe}}, \tag{3.33}$$

where, $\hat{B}_{ts}$ is the apparent peak stator slot teeth flux density, and K_{fe} is the lamination stacking factor.
The stator lower slot width, b_{s1}, is calculated as:

$$b_{s1} = \frac{\pi(D_{si} + 2h_{os} + 2h_w)}{n_s} - b_{ts}, \tag{3.34}$$

where, h_{os} is the stator slot opening height, h_w is the stator slot wedge height, and n_s is the number of stator slots.
Given the trapezoidal shape, the useful slot area can be calculated as:

$$A_{su} = h_s \frac{(b_{s2} + b_{s1})}{2}. \tag{3.35}$$

From the stator slot geometry is illustrated in Figure 3.4, the angle z^0 can be calculated from the stator slot pitch angle θ_{sp}:

$$\begin{aligned} \theta_{sp} &= \frac{2\pi}{n_s}, \\ z^0 &= \frac{\theta_{sp}}{2} = \frac{\pi}{n_s}. \end{aligned} \tag{3.36}$$

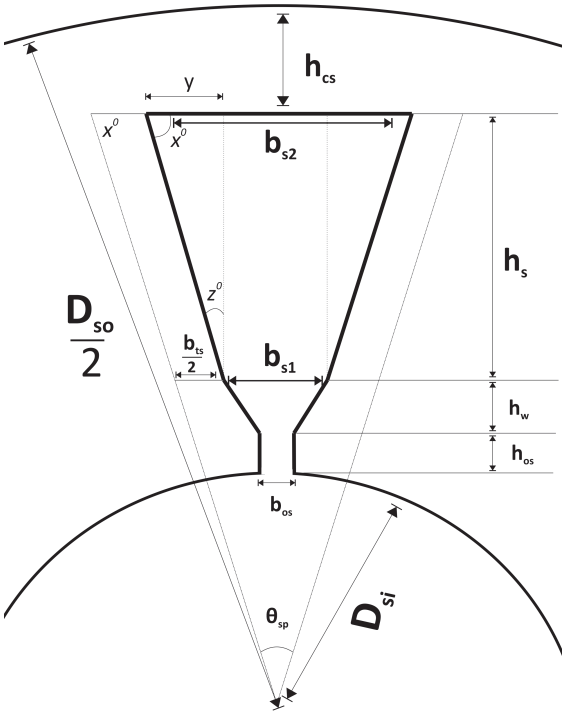

Figure 3.4: Stator slot geometry.

The length y is calculated as:

$$\tan z^0 = \frac{y}{h_s}, \tag{3.37}$$

which leads to:

$$b_{s2} - b_{s1} = 2h_s \tan z^0. \tag{3.38}$$

From equation (3.38):

$$h_s = \frac{(b_{s2} - b_{s1})}{2 \tan z^0}. \tag{3.39}$$

Substituting equation (3.39) into (3.35):

$$2A_{su} = \frac{(b_{s2} - b_{s1})(b_{s2} + b_{s1})}{2 \tan z^0}, \tag{3.40}$$

$$b_{s2}^2 - b_{s1}^2 = 4A_{su} \tan z^0, \tag{3.41}$$

The stator upper slot width, b_{s2}, is calculated as:

$$b_{s2} = \sqrt{4A_{su} \tan z^0 + b_{s1}^2}. \tag{3.42}$$

The useful slot height, h_s, is then calculated using b_{s2}, from equation (3.35):

$$h_s = \frac{2A_{su}}{b_{s1} + b_{s2}}. \tag{3.43}$$

Rotor slot dimensions

Using a similar trapezoidal slot shape as with the stator slot, the rotor slot pitch is illustrated in Figure 3.5 with the slot geometry illustrated in Figure 3.6. A similar slot fill factor, k_{fill}, as with the stator slot is selected, and the useful rotor slot area, A_{ru}, is calculated similarly as:

$$A_{ru} = \frac{\pi d'^2_{co} a_p n_{sr}}{4 k_{fill}}. \tag{3.44}$$

The rotor slot dimensions are calculated similarly to the stator slots with a little constraint. The rotor pole pitch, τ_r, is calculated as:

$$\tau_r = \frac{\pi D_{ro}}{2p_1}, \tag{3.45}$$

where, D_{ro} is the outer rotor diameter. The rotor slot pitch τ_{rp} calculated using the number of rotor slots per pole per phase, q_r, as:

$$\tau_{rp} = \frac{\tau_r}{3q_r}. \tag{3.46}$$

The rotor teeth width, b_{tr}, is then calculated as:

$$b_{tr} = \frac{\hat{B}_g \tau_{rp}}{\hat{B}_{tr} k_{fe}}, \tag{3.47}$$

where, $\hat{B}_{tr}$ is the apparent peak rotor slot teeth flux density. The rotor upper slot width, b_{r1}, is calculated as:

$$b_{r1} = \frac{\pi(D_{ro} - 2h_{or} - 2h_w)}{n_r} - b_{tr}. \tag{3.48}$$

An height, h_0, at which the slot width is zero, which translates to the sum of h_r and h_{br0} in Figure (3.6) is calculated as:

$$h_0 = \frac{\frac{b_{r2}}{2}}{\tan z}, \tag{3.49}$$

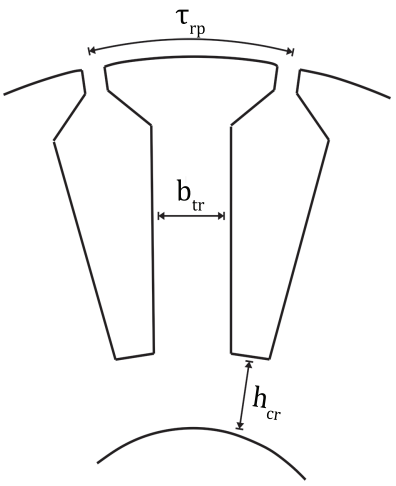

Figure 3.5: Rotor slot pitch.

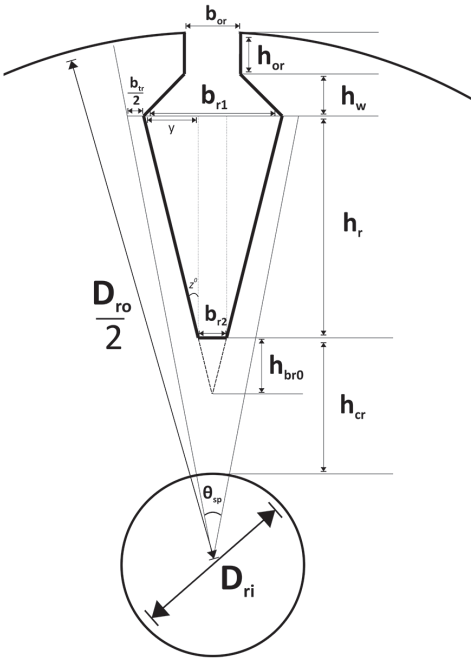

Figure 3.6: Rotor slot geometry.

the area, A_{s0}, of the right angled triangle h_0 makes with half of b_{r2} is calculated as:

$$A_{s0} = \frac{b_{r2}h_0}{4}. \tag{3.50}$$

If A_{s0} is greater than half the useful slot area, other calculations can proceed. Otherwise, it means the calculated slot area exceeds the area available for the slots with parallel teeth. If this happens, the current density or teeth flux density can be increased within permissible ranges to decrease the useful slot area or teeth area respectively. If the problem still persists, the machine aspect ratio can be reduced to increase the rotor outer diameter which makes more slot area available.

The rotor useful slot area can also be calculated similarly to equation (3.35):

$$A_{ru} = h_r \frac{(b_{r1} + b_{r2})}{2}. \tag{3.51}$$

The lower rotor slot width, b_{r2}, is then calculated as:

$$b_{r2} = \sqrt{b_{r1}^2 - 4A_{ru}\tan\frac{\pi}{n_r}}, \tag{3.52}$$

and h_r is calculated from equation (3.51) as:

$$h_r = \frac{2A_{ru}}{b_{r2} + b_{r1}}. \tag{3.53}$$

Core heights

Although, DFIG control systems are capable of power factor adjustment, a machine with a low unadjusted power factor will require larger excitation current and therefore larger

converters with increased losses. As a result, care should be taken to have appropriate core heights for both the rotor and stator.

The rotor or stator core height, $h_{cr,s}$, is calculated based on the desired back core flux density. A range of 1.4 to 1.7 T is given for the back core flux density in [12]. The equation for calculating the core height as given in [14] is:

$$h_{cr,s} = \frac{\phi_m}{2k_{fe}L\hat{B}_{cr,s}}, \tag{3.54}$$

where, $\hat{B}_{cr,s}$ is the back core flux density of rotor or stator.

3.2.6 FEA and optimization

Although the initial dimensioning and designing of electrical machines are carried out using analytical methods, numerical methods are commonly used to evaluate the performance of the machine designs and FEA is the most frequently used. FEA accurately computes the electromagnetic fields of electrical machines irrespective of the geometry. From FEA, performances such as the power factor, efficiency and AC power can be determined. The effects of saturation are also covered in the analyses. Also since all the tests are done virtually, multiple design parameters can be easily varied to investigate their effects on machine performance without having to build actual prototypes [14, 15].

A design obtained using only analytical methods may meet expected performance targets without necessarily being the best possible design. In some other cases, analytical methods may not easily achieve the desired performance targets. Many machine characteristics exhibit non-linear tendencies, and optimization techniques can be used to efficiently compute the design parameters and improve the initial design which was obtained using analytical methods.

FEA solver

The Ansys electronic desktop is used for FEA in this project. Initial models are created according to the calculated dimensions using the slot AC option for both the rotor and stator in RMxprt. The analytical RMxprt model is then converted to a transient Maxwell 2D-FEA model. This greatly reduces the amount of time that will otherwise have been spent sketching out the machine geometry solely in Maxwell.

The magnetic solvers in Maxwell (Magnetostatic, eddy current & transient) have their niche applications. Although the magnetostatic and eddy current solvers being static solvers are fast, they have their limitations for analysing DFIGs. For the magnetostatic solver, AC current cannot be applied to the model windings, while analysis is done at a single frequency for the eddy current solver thus slip frequency cannot be applied to the secondary windings. The transient solver is therefore used in analysing the rotor-tied DFIG.

The default configuration present after converting an RMxprt model with an AC slot for the rotor and stator to a time step 2D FEA model, is that of a conventional DFIG. This needs to be modified to analyse rotor-tied DFIGs. The speed of the rotor-tied DFIG is always assigned a negative polarity with respect to the magnetic fields in line with section 2.2.

FEA winding excitations

Current and voltage winding excitations are available in Maxwell transient models which can be manipulated to simulate different conditions including grid/back-to-back converter short circuit and open circuit connections. To simulate the grid side of the rotor tied DFIG, 3-phase voltages are applied to the rotor windings at grid frequency. The estimated winding resistances and end connection leakage inductances are specified in the rotor voltage windings as calculated from sections A.1 and A.2 respectively. To simulate the operations of back-to-back converters, current windings at slip frequencies are used on the stator. The following equations are adapted on the windings; $V_{A,B,C}$ for the rotor side phase voltages and $I_{U,V,W}$ for the stator phase currents:

$$\begin{aligned} V_A &= \hat{V}_{1ph} sin(\omega t), \\ V_B &= \hat{V}_{1ph} sin(\omega t - \frac{2\pi}{3}), \\ V_C &= \hat{V}_{1ph} sin(\omega t + \frac{2\pi}{3}), \end{aligned} \tag{3.55}$$

$$\begin{aligned} I_U &= \hat{I}_{2ph} sin(s\omega t - \varphi_1), \\ I_V &= \hat{I}_{2ph} sin(s\omega t - \frac{2\pi}{3} - \varphi_1), \\ I_W &= \hat{I}_{2ph} sin(s\omega t + \frac{2\pi}{3} - \varphi_1), \end{aligned} \tag{3.56}$$

where, $\hat{V}_{1ph}$ is the peak value of rated rotor phase voltage, $\hat{I}_{2ph}$ is the rated peak value of stator current calculated from equation (3.26) and φ_1 is the grid side power factor angle (used to implement unity power factor operations).

To simulate models at sub-synchronous speeds, the slip frequency is assigned a positive polarity and a negative polarity at super-synchronous speeds. To test the performance of the machine at synchronous speed, the slip frequency is set to zero and thus DC is applied at the stator windings. The rotor and stator excitations at a super-synchronous and synchronous speed are illustrated in Figures 3.7 & 3.8 respectively.

The DC applied to the stator windings at synchronous speed is the sine of the stator phase current peak($\hat{I}_{2ph}$). Phase U of the stator having no phase shift will be zero while phases W & V will be the peak current multiplied by $+\frac{\sqrt{3}}{2}$ & $-\frac{\sqrt{3}}{2}$ respectively. This way, the algebraic sum of the current magnitudes in the stator windings is similar to other speeds at slip frequency.

To run a model at unity power factor using this method, a free run has to be executed setting $\varphi_1 = 0$. The inherent machine power factor of the model is then calculated alongside the angle and then used to run a unity power factor condition. The power factor can be calculated by implementing the equations given in section C.1 as output variables in Maxwell.

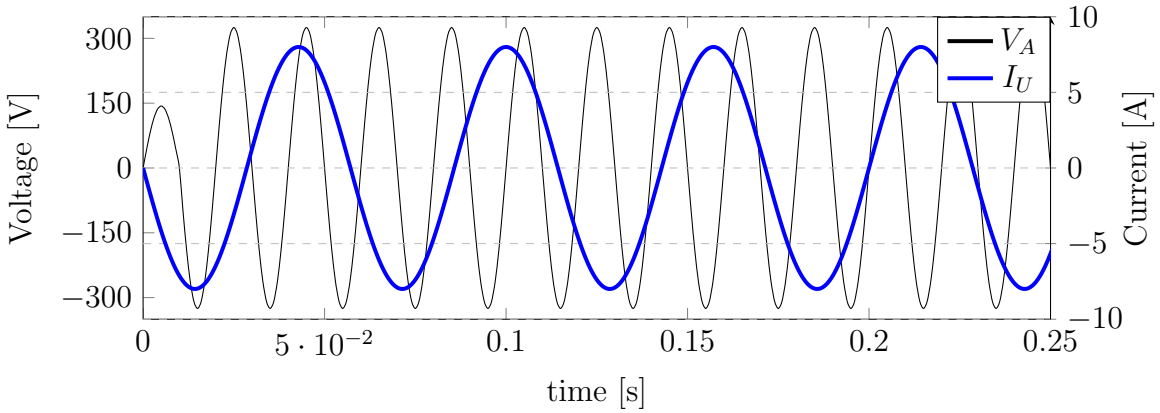

Figure 3.7: V_A & I_U at 2025rpm.

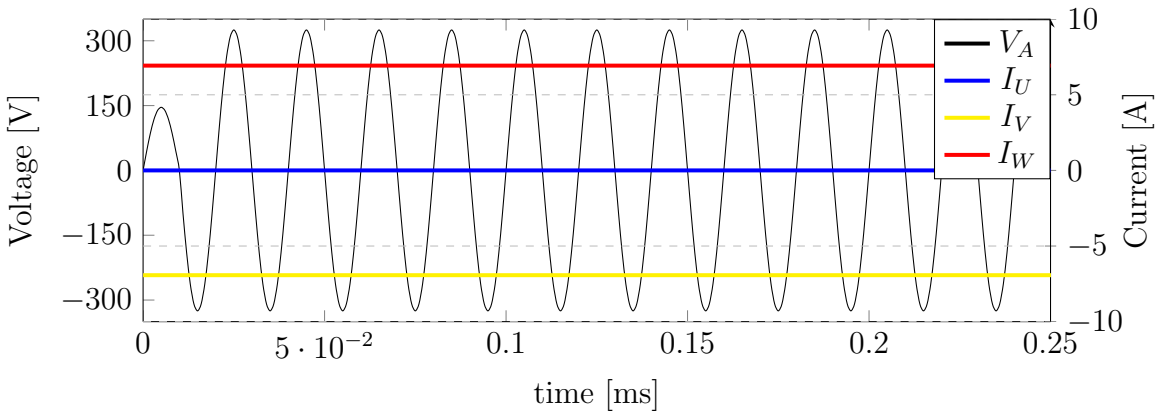

Figure 3.8: V_A, I_U, I_V & I_W at synchronous speed.

3.2.7 Optimization

Choices of optimizers are largely at the discretion of the designer as various pros and cons exist for the different optimizer types and there is no clear favourite. Experience and suitability to the specific application play huge roles in the choice of optimizers. In this research, a genetic algorithm is used for the optimization of a rotor-tied DFIG design.

The genetic algorithm uses a maximum number of iterations (generations) as a stopping criteria. A population is set alongside the probabilities of crossover and mutation. In each iteration, a population size of design points within the specified design space are evaluated. Hypothetically, if a population of 30 is set and a maximum number of 70 iterations is chosen, a total number of 2100 different designs are evaluated. If these design points are direct FEA runs, the time taken is prohibitive considering transient FEA. A pseudo-model can be obtained with a much less number of FEA solutions depending on the number of variables employed. The time taken to create the pseudo-model and run the optimization is only a small fraction compared to direct FEA coupled optimizations. A flow chart of the optimization process is illustrated in Figure 3.9.

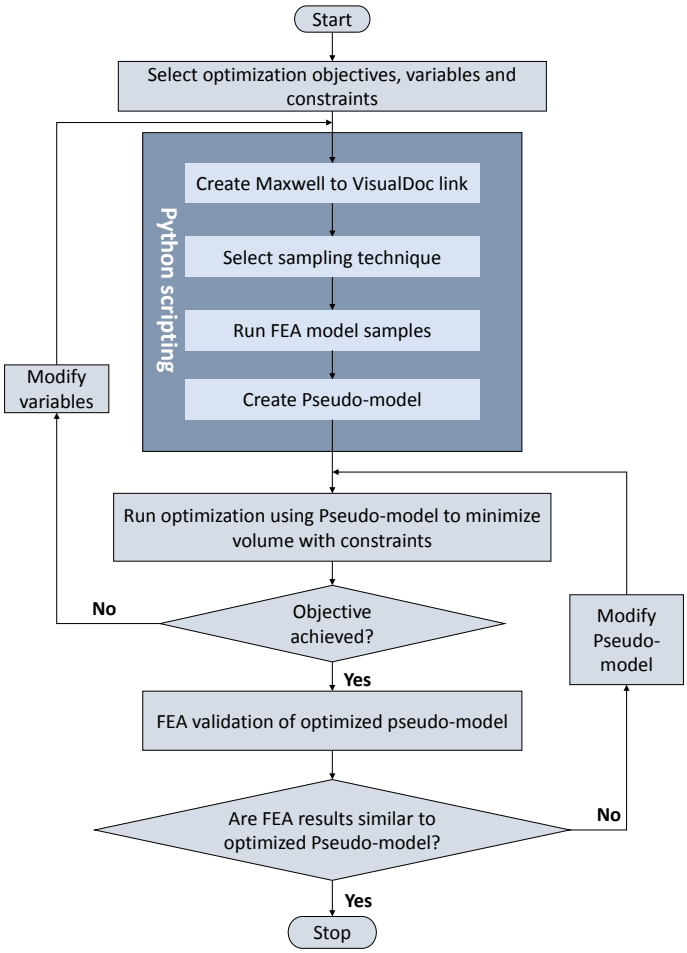

Figure 3.9: Optimization outline.

Response surface optimization

To run the optimization, the FEA package Maxwell, is connected to VisualDoc (a software integration and general purpose design optimization solution suite) via an IronPython script. The Pseudo-model used to replace the FEA models is a full quadratic response surface approximation of the FEA models. The design of experiments (DOE) for the model approximation is created by combining the optimal Latin hypercube sampling (LHS) method and a composite sampling. The two sampling methods are combined to complement each other and eliminate their weaknesses.

The LHS method is a layered random sampling technique which is largely preferred to Monte-Carlo sampling because it avoids clustering. For the LHS, the range of a variable is uniformly divided into non-overlapping intervals/subgroups. The sampling is then executed such that each subgroup is represented. The LHS is commonly used in complex response surface approximations of multi-variable optimizations due to the efficiency in sampling the design search space. The LHS however has a slight drawback of not guaranteeing the sampling of extremities in the sample space [36–38]. Composite samples are added to ensure extremities are included and increase the number of samples in general for better accuracy.

3.3 Design process summary

A summary of the rotor-tied DFIG design process is illustrated in Figure 3.10. The major aspects of the design process discussed and the accompanying analytical equations are outlined.

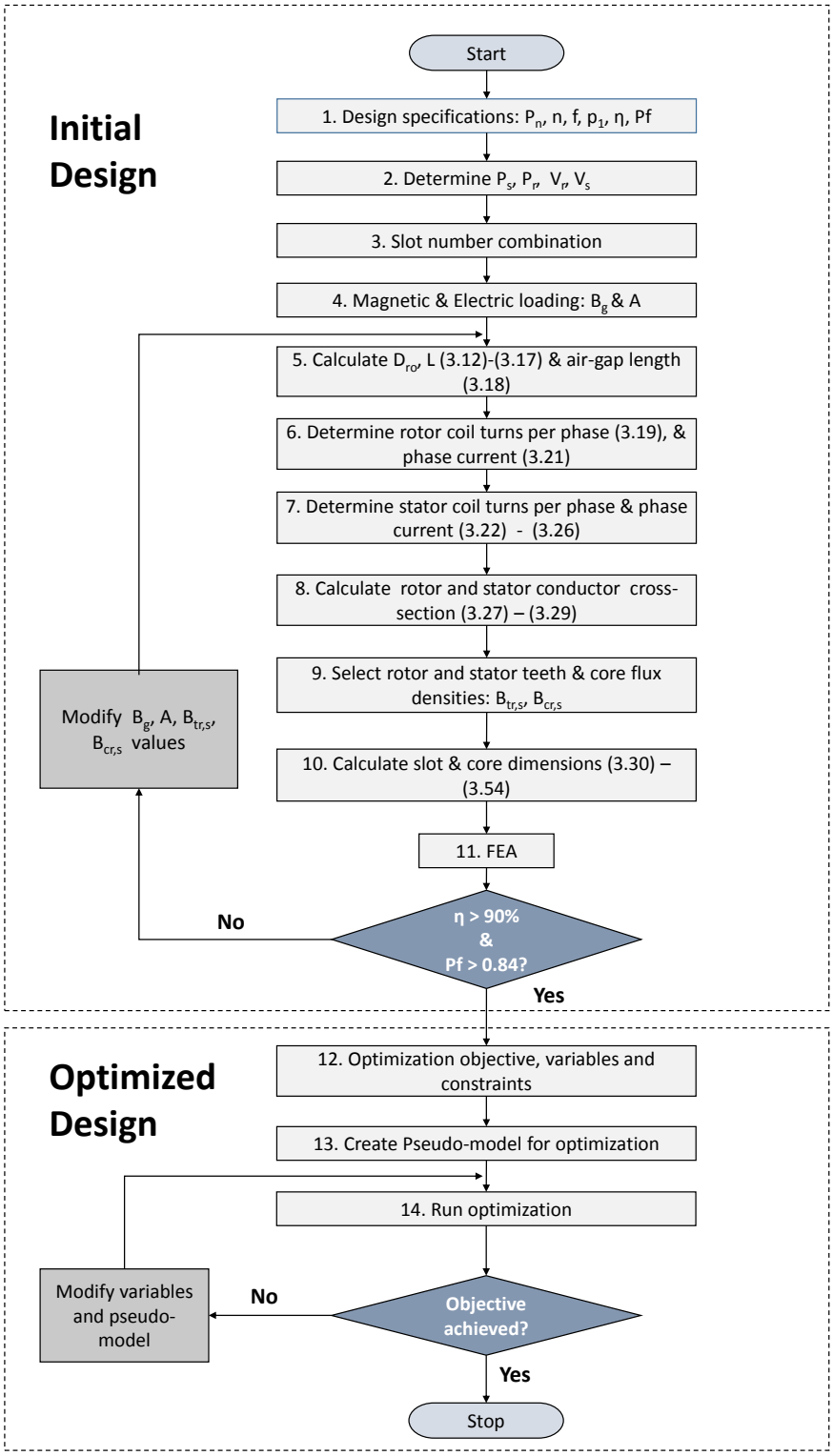

Figure 3.10: Proposed design process for the rotor-tied DFIG.

3.4 Summary

A brief summary of this chapter is as follows:

- The presentation of a detailed design process for rotor-tied DFIGs
- Design considerations such as choices of flux densities, design rated speeds, electric loading, etc., at each stage of the design process were highlighted with implications.
- Analytical equations for calculating necessary design parameters such as the D^2L, number of turns in the rotor and stator, rotor and stator voltages & currents, etc., were given.
- Analytical equations for calculating the machine slot dimensions were developed.
- FEA of rotor-tied DFIGs is explained and an optimization technique using an approximation of the FEA models is discussed.

Chapter 4

Evaluation of Conventional and Rotor-tied DFIGs

In this chapter, finite element analysis (FEA) is used to evaluate the performance of rotor-tied and conventional DFIGs designed with similar specifications but different design input parameters. The power densities (PD), power factors and total harmonic distortions (THD) of the designs are evaluated and compared. The stack aspect ratio, teeth and core flux densities are selected as key input parameters whose choices significantly affect the performance of DFIG designs. These parameters are varied to produce the different designs whose performances are compared.

4.1 Rotor-tied DFIG stack aspect ratio considerations

When calculating the number of turns per phase, a lot of rounding up is done, especially when using a double layer winding, given the even number of turns per slot condition. This leads to over-estimation or under-estimation of the winding number of turns, thus designs with different aspect ratios can have the same number of turns within reasonable limits.

The design input parameters and rated specifications given in Table 4.1 are used to design six 5.5 kW rotor-tied DFIGs with different aspect ratios. The design process used to obtain an initial design in chapter 3 is followed, but the designs are not optimized. In Table 4.2, FEA results of the six 5.5 kW rotor-tied DFIGs are shown. The results as a whole do not depict any particular trend, however a closer look at the designs with 1.1 & 1.2 aspect ratios suggests a trend. They both have the same rotor and stator number of turns per slot (n_{sr} & n_{ss} respectively), with the $\lambda = 1.2$ design having a higher power factor and lower THDs but a lower power density.

Table 4.1: Design specifications and input parameters

Item	Symbol	Unit	Value
Rated output power	P_n	kW	5.5
Rated phase voltage	V_{1ph}	V	230
Efficiency	η	%	90
Power factor	$\cos\varphi$	-	0.84
Number of pole pairs	p_1	-	2
Magnetic Loading (Air-gap flux density)	$\hat{B}_g$	T	0.75
Electric loading	A	Am^{-1}	17000
Form factor	K_f	-	1.11
Flux density shape factor	α	-	$\frac{2}{\pi}$
Stator to input mechanical power ratio	$\lvert\frac{P_s}{P_m}\rvert$		0.26
Teeth flux density	$\hat{B}_{t(r,s)}$	T	1.6
Core flux density	$\hat{B}_{c(r,s)}$	T	1.5

Table 4.2: Summary of 5.5 kW rotor-tied DFIGs with different aspect ratios

	Items	A $\lambda = 1.1$	B $\lambda = 1.2$	C $\lambda = 1.3$	D $\lambda = 1.4$	E $\lambda = 1.5$	F $\lambda = 1.6$
Design parameters	D_{ro}/L (mm)	146/125	142/133	138/141	134/148	131/155	129/162
	N_r	168	168	156	156	156	144
	N_s	200	200	192	184	184	176
	n_{sr}	28	28	26	26	26	24
	n_{ss}	50	50	48	46	46	44
FEA results	Power factor	0.83	0.85	0.82	0.822	0.827	0.8
	PD (Wcm^{-3})	0.758	0.751	0.727	0.740	0.751	0.6996
	Current THD (%)	11.8	10.6	11.3	11.4	11.2	11.26
	Voltage THD (%)	0.87	0.85	0.77	0.85	0.83	0.85

To further evaluate the effect of the aspect ratio selection, the calculated winding number of turns per phase for a 5.5 kW rotor-tied DFIG with $\lambda = 1.0, 1.3, 1.4$ & 1.6 are each used for a number of designs with different aspect ratios (rotor diameters and stack lengths). In this way, the number of turns per phase for the extreme aspect ratios (1.0 & 1.6) are used as a limit for the possible number of turns for that machine rating. For each set, the number of turns is kept constant but the rest of the design follows the process set out in chapter 3. The optimization aspect of the process is also not performed.

Varying the aspect ratio with the number of turns kept constant, at a basic level, is similar to varying the air-gap flux density, $\hat{B}_g$. However, the machine shapes are different and the aspect ratios give a higher degree of design freedom than using $\hat{B}_g$. This is because, if only $\hat{B}_g$ is varied, when calculating the number of turns per slot, a lot of rounding off is done which alters the value of $\hat{B}_g$. As a result, machines whose D^2L are calculated with different $\hat{B}_g$ can end up having the same $\hat{B}_g$ based on the number of turns.

Designs with the same aspect ratios across different sets have the same rotor outer diameters and stack length but different outer stator and inner rotor diameters. The slot dimensions also differ for designs with different turns numbers having similar aspect ratios. The teeth and core flux densities are kept constant at 1.6T & 1.5T respectively for all the designs.

4.1.1 Power factor

The power factors of the different designs are illustrated in Figure 4.1. For designs with the same number of turns, there is an observable increase in power factor with increase in aspect ratio. Also, the designs with higher number of turns have higher power factors than designs with similar aspect ratios. Therefore, higher number of turns and aspect ratios could lead to higher power factors. This is as a result of a reduction in air-gap flux density with aspect ratio and number of turns increases.

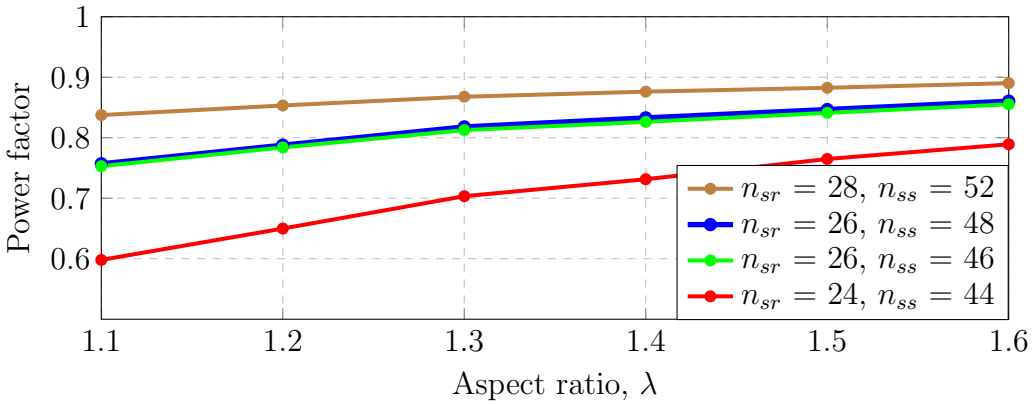

Figure 4.1: Power factors of 5.5 kW rotor-tied DFIGs designed with different aspect ratios.

4.1.2 Power density

The power density curves for the different designs are illustrated in Figure 4.2. Except in one case (designs with n_{sr}=24 & n_{ss}=44), designs with the same number of turns decrease in power density with increase in aspect ratio. This is traceable to the reduction in $\hat{B}_g$ which leads to bigger machines.

Generally, the designs with higher power factors generate slightly more power, but the machine volume increases with increasing aspect ratio. The increase in volume however supersedes the power rise, hence the decrease in power densities with increasing aspect ratios.

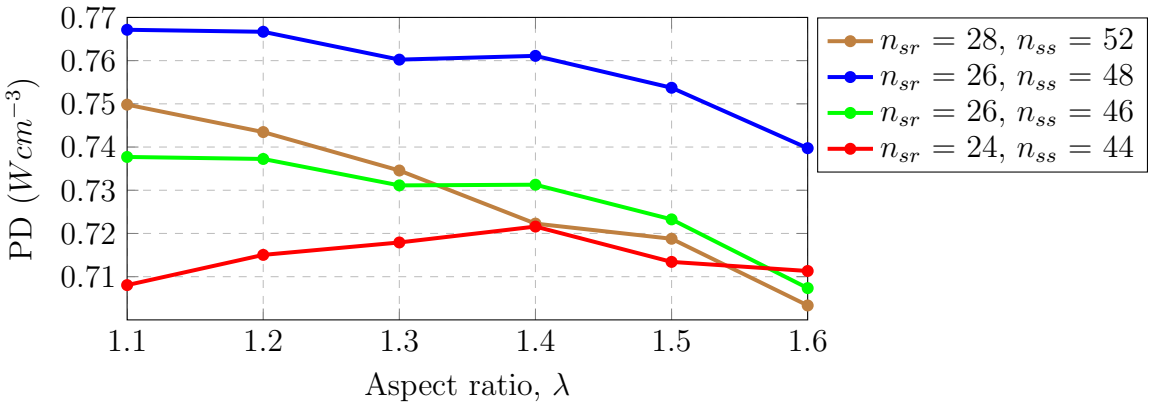

Figure 4.2: Power density of 5.5 kW rotor-tied DFIGs designed with different aspect ratios.

4.1.3 Current and voltage THD

The current and voltage THDs of the different designs are illustrated in Figures 4.3 & 4.4 respectively. There seems to be a decrease in THDs with increasing aspect ratios. The trend is also such that the designs with higher winding turns have less THDs than those with lower winding turns. This may be as a result of the higher number of mmf steps present from the higher number of turns, thereby reducing harmonics.

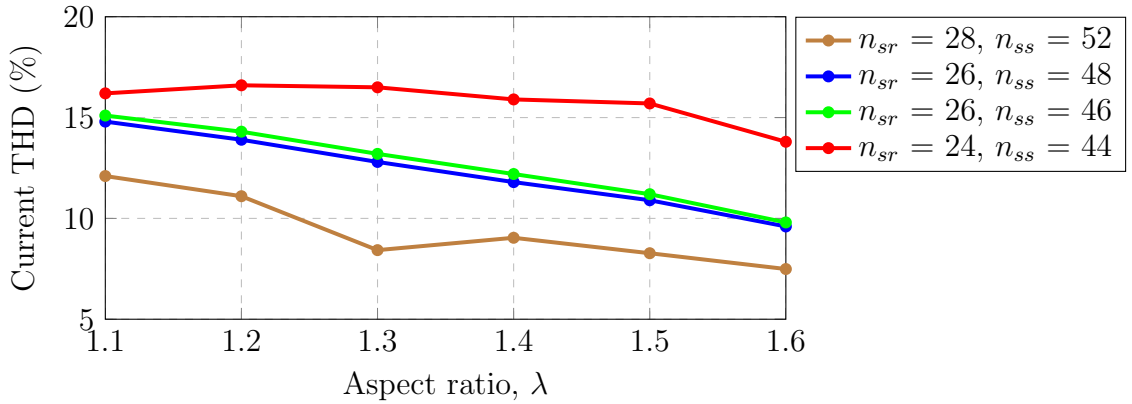

Figure 4.3: Current THD of 5.5 kW rotor-tied DFIGs designed with different aspect ratios.

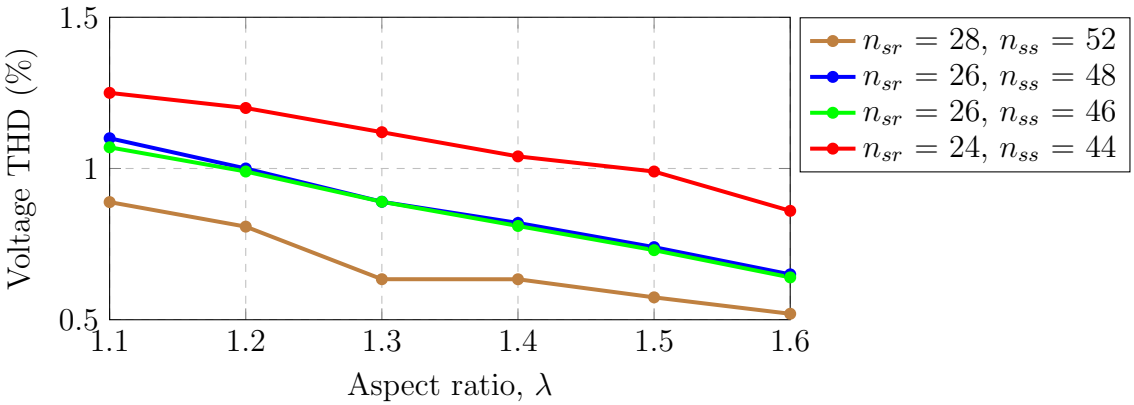

Figure 4.4: Voltage THD of 5.5 kW rotor-tied DFIGs designed with different aspect ratios.

4.1.4 Conventional DFIG aspect ratios

Conventional 5.5 kW DFIGs are designed using a similar initial design process for rotor-tied DFIGs given in chapter 3. Optimization is also not performed for the designs. The stators are however used as the primary sides, which generate a higher proportion of the DFIG power, with the rotors generating only a fraction of the rated power. The stators of the conventional DFIG designs also have 36 slots and the rotors, 24. To ensure fair comparisons with the rotor-tied DFIG designs, similar winding turn numbers are used. The stator inner diameter of the conventional DFIGs is determined in the same manner as the outer rotor diameter of the rotor-tied DFIGs.

The performances of the conventional DFIG designs with different aspect ratios are similar to the rotor-tied DFIGs with the same aspect ratios. The power factors, power density and total harmonic distortions of the conventional DFIGs are illustrated in Figures 4.5, 4.6, 4.7 & 4.8 respectively. There is no striking difference in the performance of either topology.

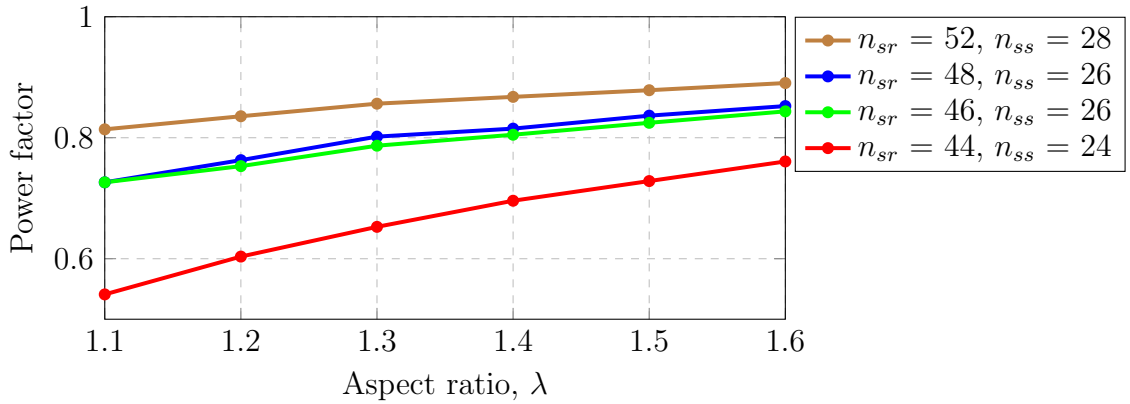

Figure 4.5: Power factors of conventional 5.5 kW DFIGs designed with different aspect ratios.

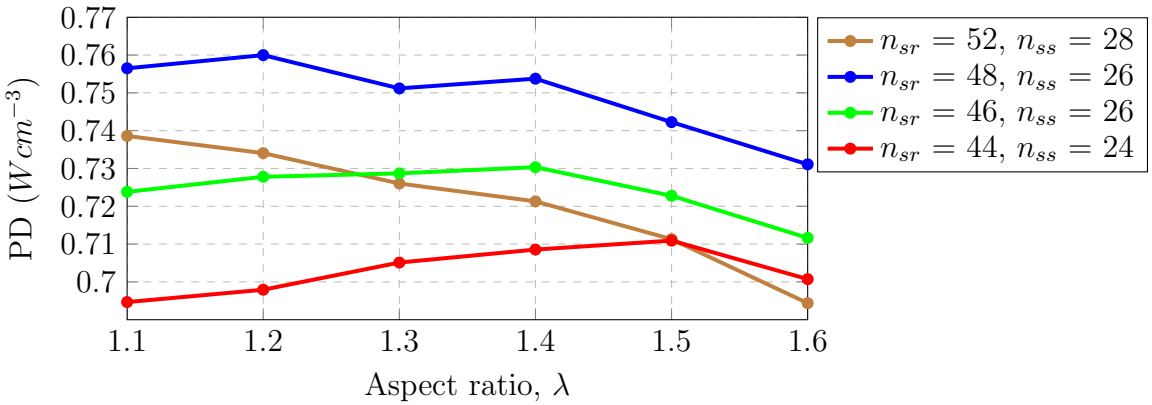

Figure 4.6: Power density of conventional 5.5 kW DFIGs designed with different aspect ratios.

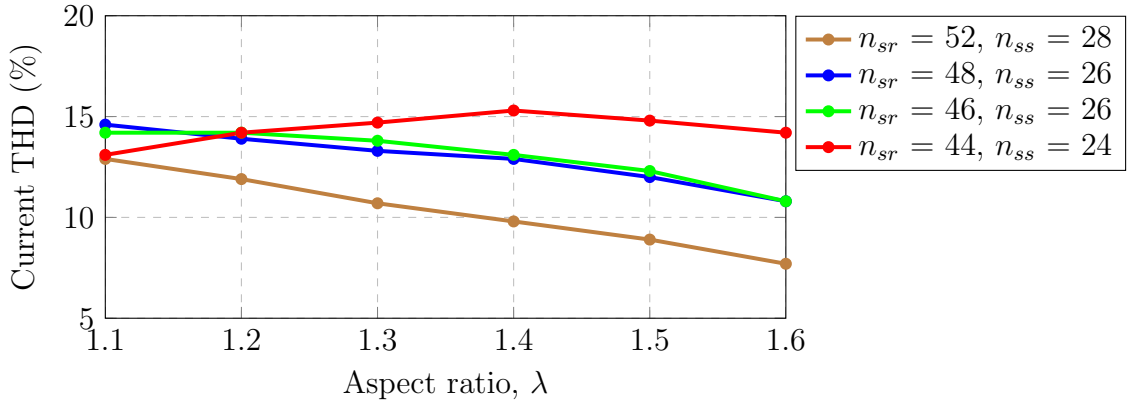

Figure 4.7: Current THD of conventional 5.5 kW DFIGs designed with different aspect ratios.

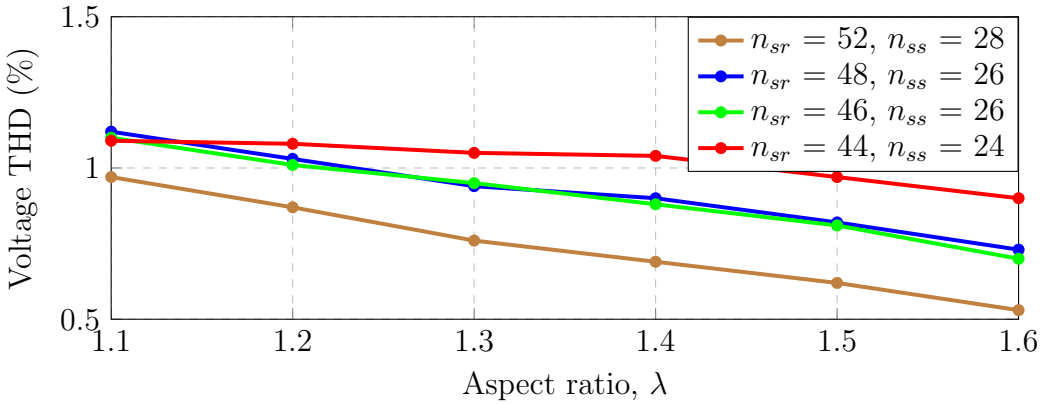

Figure 4.8: Voltage THD of conventional 5.5 kW DFIGs designed with different aspect ratios.

4.2 Assessing rotor-tied and conventional DFIGs

According to [21], designing DFIGs in view of the rotor-tied operation results in smaller sized machines. The FEA results of the designs in section 4.1 do not show any significant difference in the performance of rotor-tied and conventional DFIGs. The power densities (and performance in general) of the designs in either topology are very similar. In the methodology detailed in chapter 3, the core and teeth sizes are determined by the choice of flux densities in those parts. The outer rotor diameter (D_{ro}), of rotor-tied DFIGs and the inner stator diameter (D_{si}), of conventional DFIGs are sized according to power. (D_{ro}) and (D_{si}) for similar power ratings and aspect ratios are however approximately the same, given the negligible value of the air-gap length.

To further test the different topologies, the core and teeth flux densities of 5.5 kW rotor-tied and conventional DFIGs, with specifications given in Table 4.3, are varied and performances are compared. Varying the flux densities is influenced by the knowledge that designing machines with higher flux densities leads to smaller machines but may compromise performance. The designs are therefore to test the tolerances of both topologies to size reductions.

Table 4.3: Design specifications of rotor-tied and conventional DFIGs being compared.

Item	Unit	Rotor-tied	Conventional
Air-gap flux density, $\hat{B}_g$	T	0.75	
Electric loading, A	Am^{-1}	17000	
Pole pairs, p_1		2	
Test speed	rpm	2025	
Stack length, L	mm	150	
D_{ro}/D_{si}	mm	144 (D_{ro})	144 (D_{si})
Number of rotor slots, n_r	-	36	24
Number of stator slots, n_s	-	24	36
Rotor turns per phase, N_r	-	168	192
Stator turns per phase, N_s	-	192	168
Stator/rotor current, (I_s/I_r)	A	5.65 (I_s)	5.65 (I_r)

Four different parameters are selected for variations, the rotor & stator teeth flux densities, $B_{tr,s}$, and the rotor & stator core flux densities, $B_{cr,s}$. The flux densities are varied between 1.6 - 1.9 T for the teeth and cores. Although the primary purpose of this section is to compare the different DFIG topologies, observations of the performances of DFIGs in general to flux density variations are also underscored.

4.2.1 Effect of flux density on power factor

The effect of increasing the flux density on the machine grid side power factor is straightforward. The resultant power factors with different flux densities in the teeth and cores of the designed rotor-tied and conventional DFIGs are illustrated Figures 4.9 & 4.10 respectively. Higher flux densities lead to higher magnetizing currents and consequently lower power factors as observed in the figures. The power factor for both topologies decrease with increase in flux densities and there is no clear difference in power factors for designs with the same flux density for either topology.

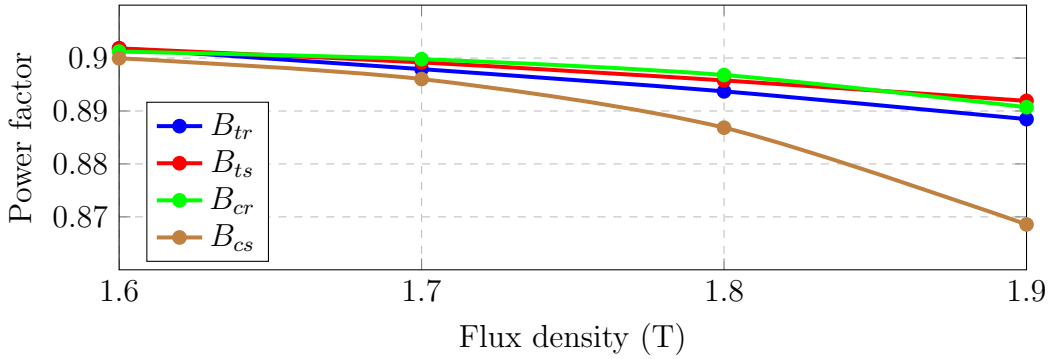

Figure 4.9: Power factor at different teeth and core flux densities for 5.5 kW rotor-tied DFIGs

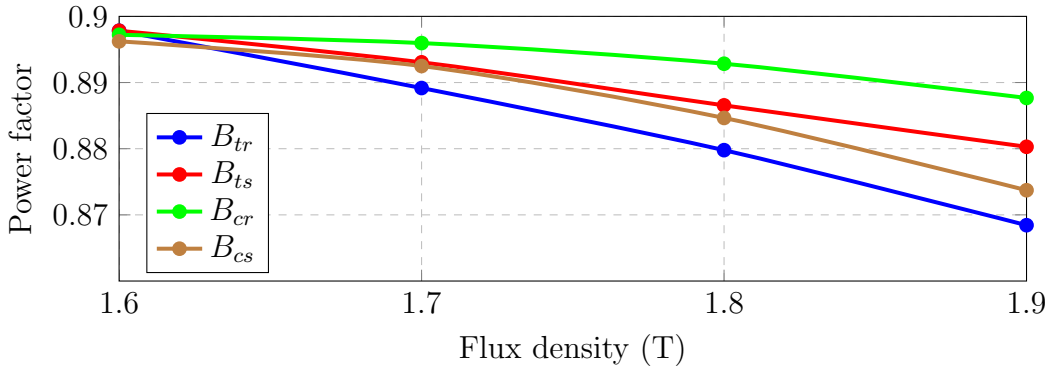

Figure 4.10: Power factor at different teeth and core flux densities for 5.5 kW conventional DFIGs.

4.2.2 Effect of flux density on power density

The effect of teeth and core flux densities on the power densities of a rotor-tied and conventional DFIG is illustrated in Figures 4.11(a) & 4.11(b) respectively. The designs with higher (teeth or core) flux density have higher power densities for both topologies. The power density variation is more significant with the core flux density variations especially the stator core for both topologies. This is due to the stator core being large, so increases in the design stator core flux density shave off more significant core volume. Similar to the power factor, the power density values at the same flux densities for both topologies are not significantly different.

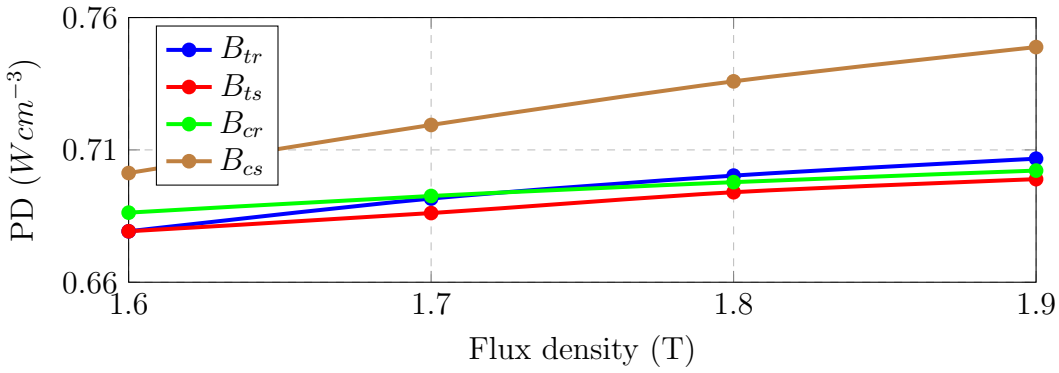

(a)

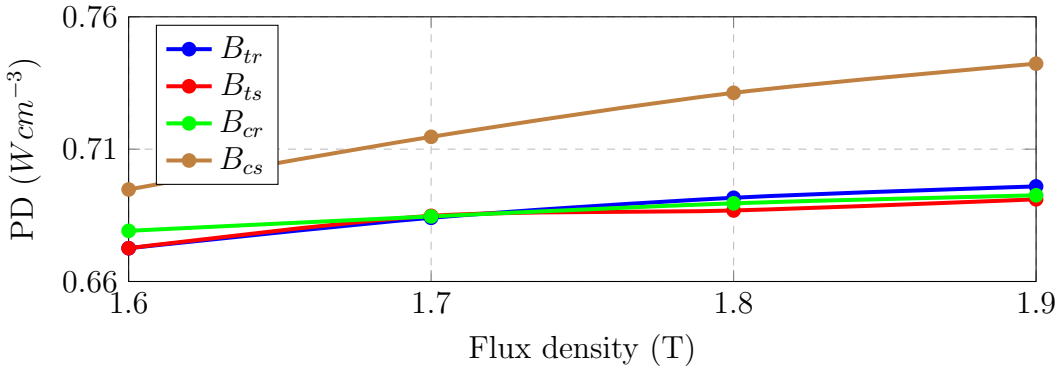

(b)

Figure 4.11: Power density at different teeth and core flux densities (a) 5.5 kW rotor-tied DFIGs, (b) 5.5 kW conventional DFIGs.

4.2.3 Effect of flux density on current and voltage THD

The plots for current and voltage THDs with varying design flux densities for both topologies are illustrated in Figures 4.12 & 4.13. The patterns and values for the THDs for both topologies are similar. Increasing the teeth flux density increased the THDs while increasing the core flux densities reduced the THDs. The designs with high stator core flux densities had the least THDs for both topologies.

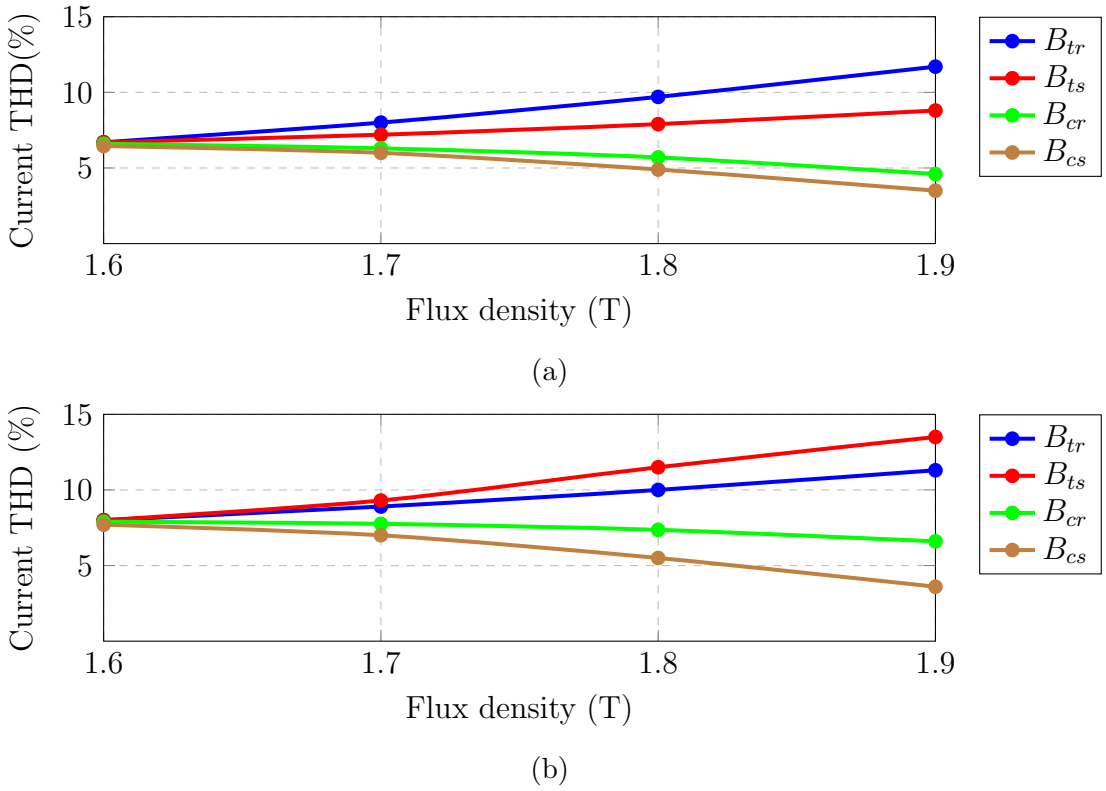

(a)

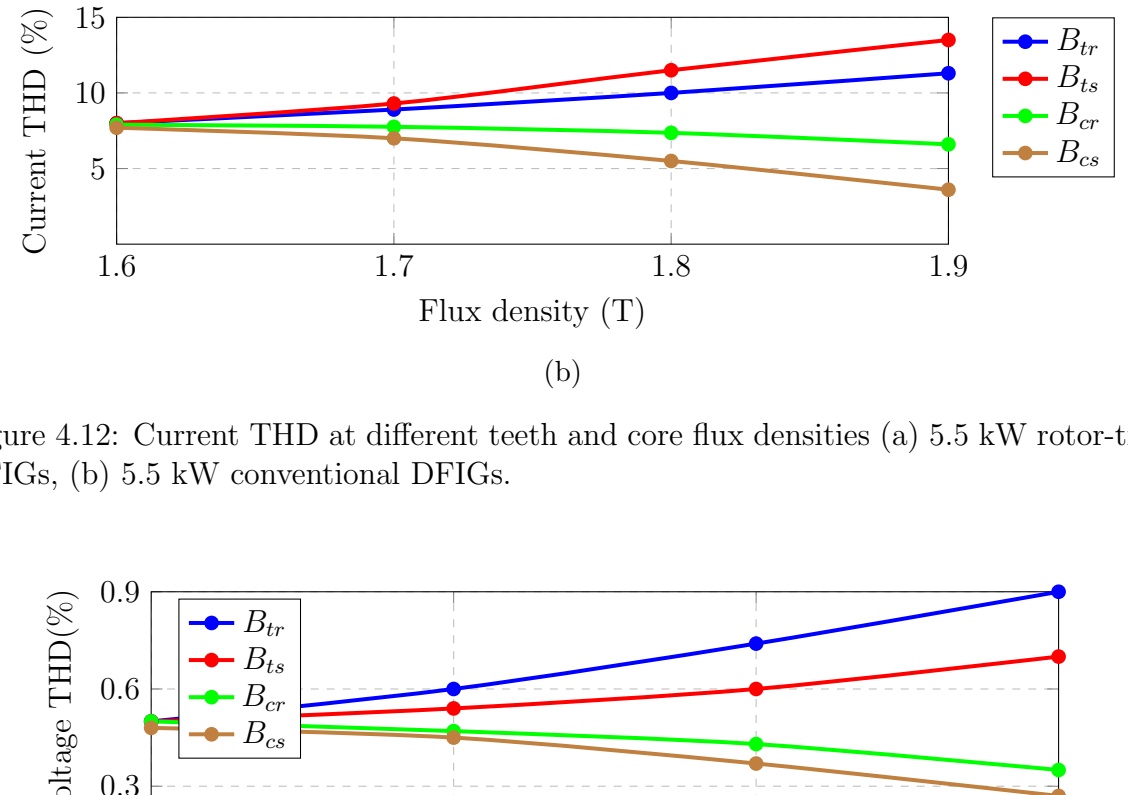

(b)

Figure 4.12: Current THD at different teeth and core flux densities (a) 5.5 kW rotor-tied DFIGs, (b) 5.5 kW conventional DFIGs.

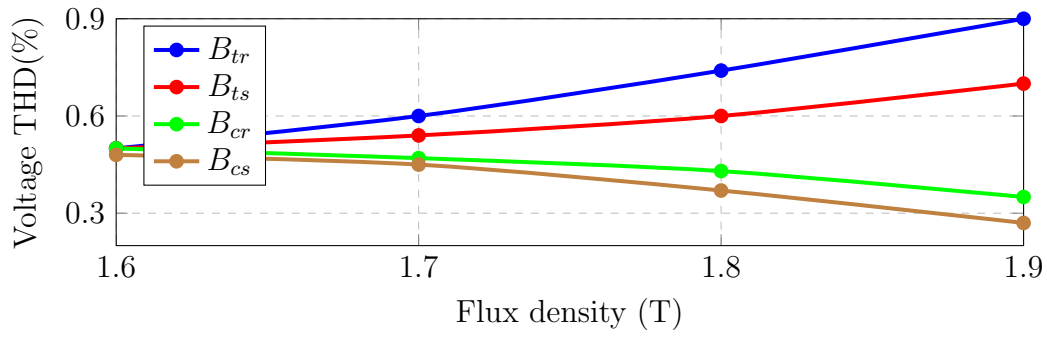

(a)

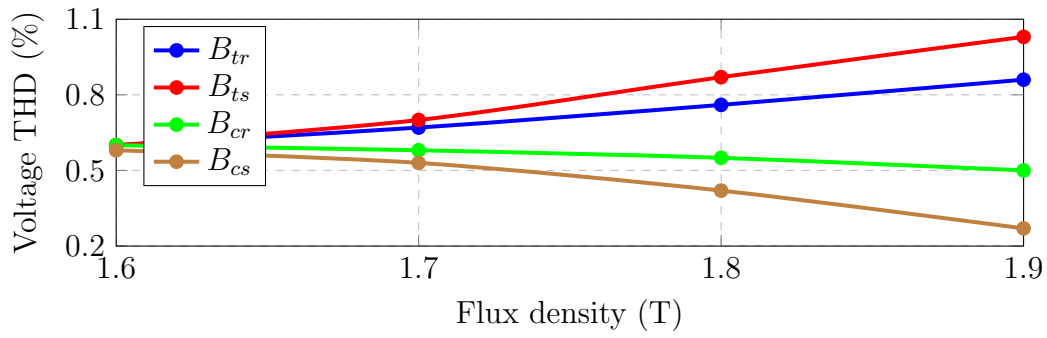

(b)

Figure 4.13: Voltage THD at different teeth and core flux densities (a) 5.5 kW rotor-tied DFIGs, (b) 5.5 kW conventional DFIGs.

4.3 Core flux density limit

From section 4.2, increasing the core flux densities increased the power densities while decreasing the power factor, with a reduction in the THDs within the range tested. In design handbooks [12, 14], the core flux densities are usually prescribed lower values than the teeth flux densities. Although, the reduction in THDs with increased core flux density is desired the flux densities cannot be increased indefinitely as the effects of saturation become more significant at some point. Further 5.5 kW rotor-tied DFIG designs with higher flux densities on the cores are tested. Conventional DFIG designs are not tested as their performances closely match rotor-tied DFIG designs of the same specifications. The flux density in the cores is steadily raised till $2.5T$. Different steel lamination types $M400-50A$, $M530-50A$ & $M19-24G$ are also used.

4.3.1 Power factor

The power factors of different steel laminations used in 5.5 kW rotor-tied DFIG designs with varying core flux densities are illustrated in Figure 4.14. The different steel lamination types follow similar patterns as the power factors decrease with increase in flux densities. Varying the rotor core flux density as illustrated in Figure 4.14(a) affects the power factor less than the stator core flux densities as illustrated in Figure 4.14(b), because of their smaller core area.

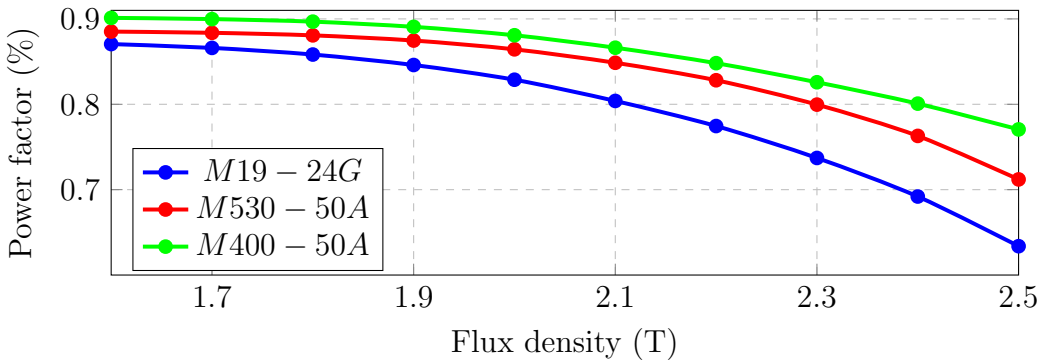

(a)

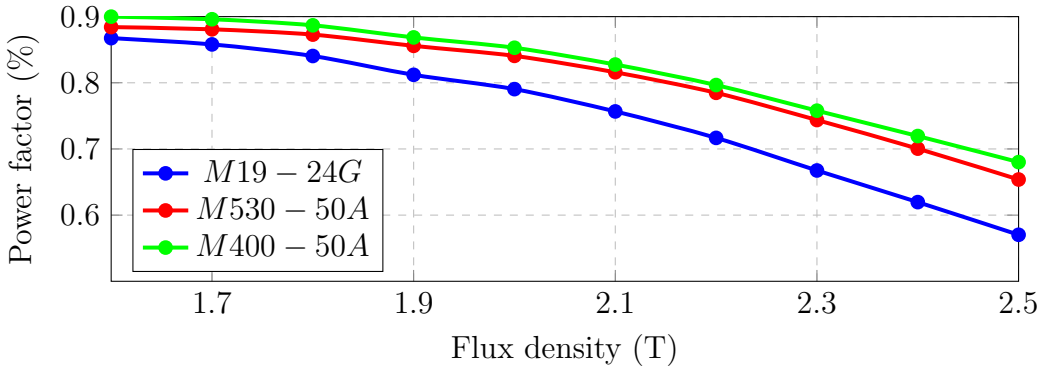

(b)

Figure 4.14: Power factors of 5.5 kW rotor-tied DFIGs with different steel lamination types (a) Varying B_{cr}, (b) Varying B_{cs}.

4.3.2 Total harmonic distortions

The current and voltage THDs illustrated in section 4.2 closely match in pattern as designs with higher current THDs had higher voltage THDs and vice versa. This pattern is also observable for the THDs illustrated in Figures 4.15 & 4.16. As observed, the THD values do not decrease indefinitely with increases in core flux density. For the different steel lamination types, the THD values are lowest at core flux densities around 2 - 2.2T. Varying the rotor core flux density achieved the lowest THD values. This can be due to higher degrees of freedom in varying the rotor core flux density as it affects smaller areas.

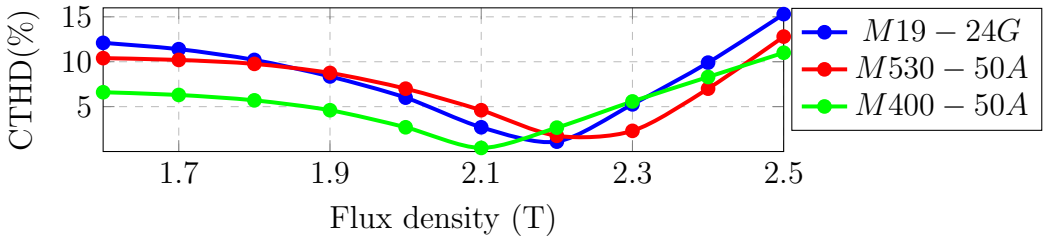

(a)

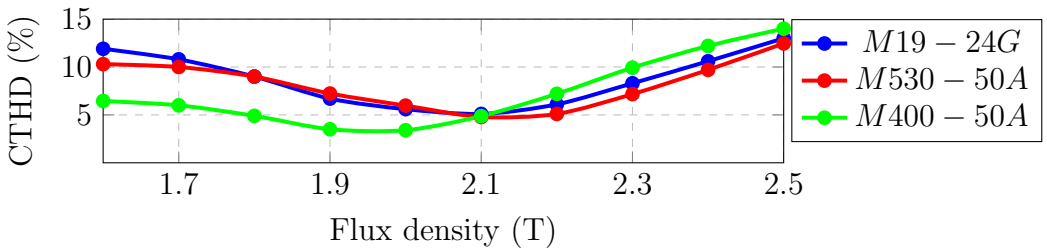

(b)

Figure 4.15: Current THD of 5.5 kW rotor-tied DFIGs with different steel lamination types (a) Varying B_{cr}, (b) Varying B_{cs}.

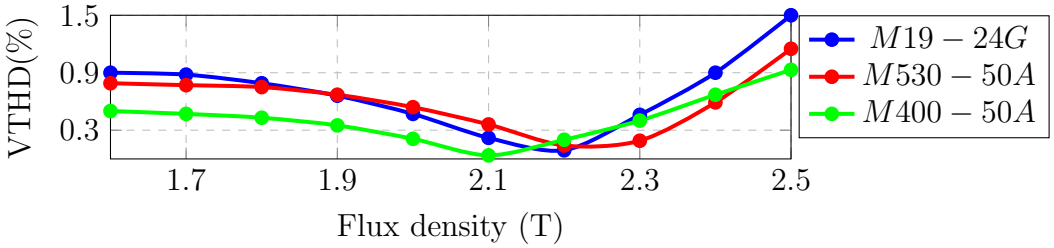

(a)

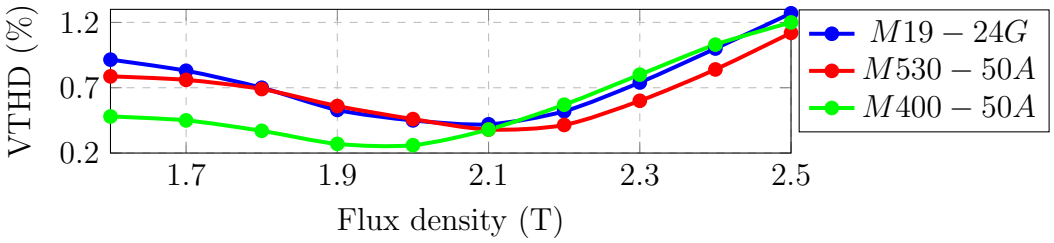

(b)

Figure 4.16: Voltage THD of 5.5 kW rotor-tied DFIGs with different steel lamination types(a) Varying B_{cr}, (b) Varying B_{cs}.

4.3.3 Rotor-tied DFIGs with different power ratings

Prior tested rotor-tied DFIGs are rated at 5.5 kW, so the performance of rotor-tied DFIGs with higher power ratings (7.5 kW, 10 kW, 20 kW & 25 kW) are tested for further observation. The rotor-tied DFIGs are designed using the initial design process given in chapter 3 without optimization. In Table 4.4, the specifications and dimensions of the different designs tested are detailed. The rotor and stator core flux densities are varied from 1.5 - 2.5T for the different power ratings and the THDs are observed.

The current and voltage THDs of the different designs are illustrated in Figures 4.17 & 4.18 respectively. Similar to the different 5.5 kW rotor-tied DFIGs, the lowest THD values are achieved at slightly higher rotor core flux densities than the stator core flux densities. For all the power ratings, the lowest THD values are obtained at higher than typically prescribed flux density values.

Table 4.4: Design summary of rotor-tied DFIGs with different power ratings

Item	**Unit**	**7.5 kW**	**10kW**	**20kW**	**25kW**
D_{ro}	mm	146	161	205	209
L	mm	172	190	225	246
g	mm	0.35	0.4	0.45	0.45
N_r	-	36	36	48	48
n_r	-	24	20	8	8
N_s	-	24	24	36	36
n_s	-	42	78	32	28
V_{2ph}	V	100	230	230	230

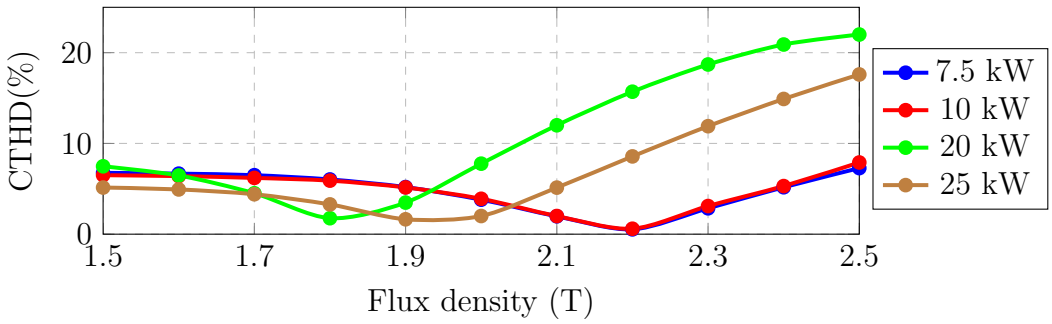

(a)

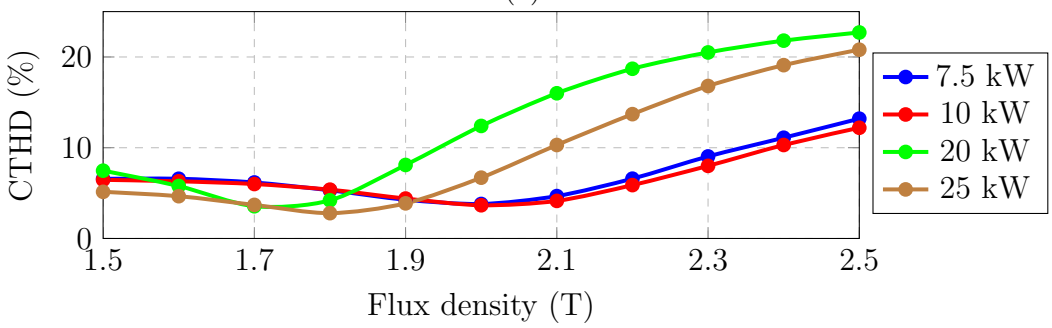

(b)

Figure 4.17: Current THD of rotor-tied DFIGs with different power ratings (a) Varying B_{cr}, (b) Varying B_{cs}.

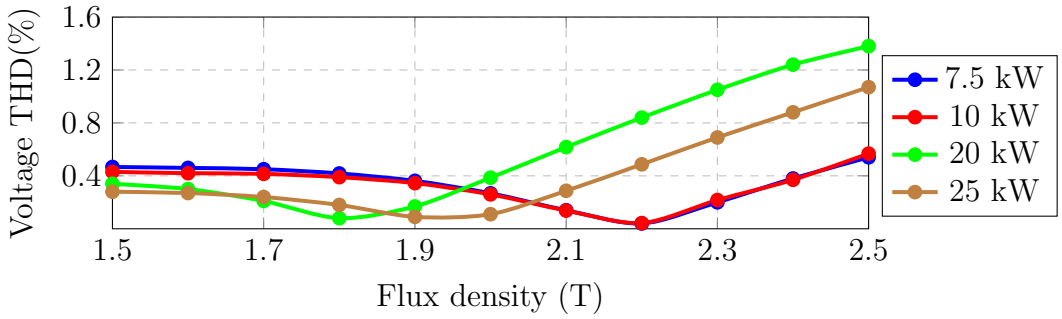

(a)

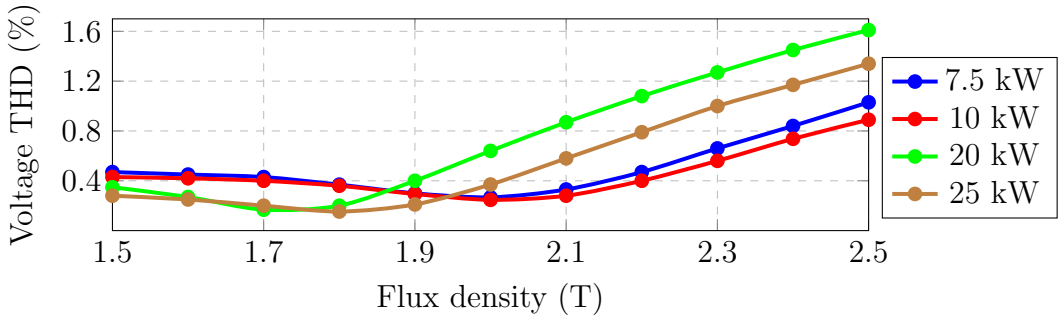

(b)

Figure 4.18: Voltage THD of rotor-tied DFIGs with different power ratings (a) Varying B_{cr}, (b) Varying B_{cs}.

4.4 Summary

In this chapter, the performances of (rotor-tied and conventional) DFIGs with different aspect ratios, teeth and core flux densities were evaluated. The effects of these input parameters on the machine performance were highlighted. Important points in the chapter are listed as follows:

- For designs with the same number of turns per phase, the rotor-tied and conventional DFIGs with higher aspect ratios tended to achieve higher power factors with lower harmonic content at the expense of slightly lower power densities.
- For the same power rating, the total machine size was not dependent on the part (rotor or stator) generating the bulk of the power, instead the size was dependent on the choice of flux densities in the teeth and core of these parts and the aspect ratio.
- An increase in teeth flux density increased the harmonic content in the machine and lowered the power factor. This phenomenon is traceable to saturation in the teeth.
- An increase in core flux density also leads to lower power factors but seemed to lead to lower harmonic content till flux densities were too high and the effect of saturation was more apparent. Lower harmonic contents were observed in core flux densities which are higher than normally prescribed in machine design handbooks.

Chapter 5

FEA and Optimization of a 5.5 kW Rotor-tied DFIG

One of the objectives of this project is to design and test a 5.5 kW rotor-tied DFIG, and an initial prototype design is obtained using the proposed design process described in chapter 3. 2D transient time step FEA is performed on the design in a grid connected generating mode to examine performance. The FEA is used to determine the power density, the power factor and harmonic content of the design.

A shape optimization of the initial design to increase the power density and reduce the harmonic content is also performed. The optimization is performed with a response surface approximation of the machine FEA model developed using a combination of the latin hypercube sampling (LHS) and composite sampling.

5.1 Initial design

The prototype design specifications are given in Table 5.1. Following the design process presented in chapter 3, the calculated initial DFIG dimensions are given in Table 5.2. The machine rated speed is selected as 2025 rpm which corresponds to a slip of -0.35, and it is estimated that the proportion of the stator to the input mechanical power, $|\frac{P_s}{P_m}|$, is 0.26 at this speed using equation (2.17). A standard 132M frame and a pre-designed shaft are used for the prototype, thus the stator outer diameter, D_{so}, and the rotor inner diameter, D_{ri}, are fixed at 220 mm and 48 mm respectively. The fixed value of D_{so} influenced the aspect ratio, λ, choice as care is taken to maximize the rotor size, thus the low λ value. The value of the specific electric loading, A, selected is based on the range of values suggested in [33] for 5.5 kW rated machines. The rotor and stator teeth flux density $\hat{B}_{t(r,s)}$, is selected based on the range given in [12].

Two rotor-stator slot combinations are tested; the first with 36 rotor and 24 stator slots, the other with 24 rotor and 36 stator slots. The values of the design dimensions are given in Table 5.2. The values in the square brackets represent the dimensions of the 24 rotor slot design. To ensure a fair comparison, the same number of turns per phase are used in both model sets, i.e., for both sets their stators have the same number of turns likewise for the rotors.

The grid voltage (230V) is considered alongside a lower voltage (100V) for use as the rated stator phase voltage. In Table 5.3, the details of the stator windings are specified. The values in square brackets are of the parameters using 100V on the stator. The stator windings with similar voltage (230V) to the grid require too many turns in the slot with too thin cross-sections, so 100V is selected.

Table 5.1: Design specifications and parameters of a 5.5 kW rotor-tied DFIG

Item	Symbol	Unit	Value
Rated output power	P_n	kW	5.5
Rated phase voltage	V_{1ph}	V	230
Grid frequency	f	Hz	50
Efficiency	η	%	90
Inherent Power factor	$\cos\varphi$	-	0.84
Number of pole pairs	p_1	-	2
Magnetic Loading (Air-gap flux density)	$\hat{B}_g$	T	0.75
Electric loading	A	Am^{-1}	17000
Form factor	K_f	-	1.11
Flux density shape factor	α	-	$\frac{2}{\pi}$
Rated Speed	n	rpm	2025
Stator to input mechanical power ratio	$\lvert\frac{P_s}{P_m}\rvert$		0.26
Stator power	P_s	kW	1.43
Rotor power	P_r	kW	4.07
Rotor current	I_{1ph}	A	6.2
Stack aspect ratio	λ	-	1.15
Teeth flux density	$B_{t(r,s)}$	T	1.6
Outer stator diameter	D_{so}	mm	220
Inner rotor diameter	D_{ri}	mm	48

Table 5.2: Initial dimensions of a 5.5 kW rotor-tied DFIG

Items		Unit	Value
Stack length, L		mm	130
Air gap		mm	0.35
Rotor	Outer diameter	mm	144
	Inner diameter, D_{ri}	mm	48
	Slot number	-	36[24]
	Turns per slot	-	28[42]
	Coil pitch	-	$\frac{7}{9}$
	Teeth width, b_{tr}	mm	6.04[9.18]
	Upper slot width, b_{r1}	mm	6.35[9.7]
	Lower slot width, b_{r2}	mm	2.9[4.96]
	Slot height, h_r	mm	19.75[17.9]
	Conductor diameter (a_p)	mm	0.912(2)
	Useful slot area	mm^2	91.46[131]
Stator	Outer diameter, D_{so}	mm	220
	Inner diameter	mm	144.7
	Slot number	-	24[36]
	Turns per slot	-	48[32]
	Coil pitch	-	$\frac{5}{6}$
	Teeth width, b_{ts}	mm	9.1[6.14]
	Lower slot width, b_{s1}	mm	10.11[6.5]
	Upper slot width, b_{s2}	mm	13.26[8.65]
	Slot height, h_s	mm	11.98[12.4]
	Conductor diameter (a_p)	mm	1.219(1)
	Useful slot area	mm^2	140.1[94]

Table 5.3: Stator winding parameters

Item	Symbol	Unit	Value
Stator phase voltage	V_{2ph}	V	230[100]
Stator frequency	f	Hz	17.5
Stator current	I_{2ph}	A	2.35[5.65]
Turns per slot	n_s		112[48]
Wire cross-section	A_{co}	mm^2	0.47[1.13]

5.2 FEA results

The flux density distributions and flux lines of the 36 and 24 rotor slots models using FEA are illustrated in Figure 5.1. The desired values for the teeth and core flux densities ($\hat{B}_{t(r,s)}$ & $\hat{B}_{c(r,s)}$), which are 1.6T & 1.5T respectively, are not exceeded in the initial designs.

The FEA stator power to the input mechanical power ratio $|\frac{P_s}{P_m}|$, with varying slip is compared with values calculated using equation (2.18); This is illustrated in Figure 5.2. The 36 rotor slots model is used for the FEA and it can be observed that the FEA results closely match the analytical calculations.

5.2.1 Power factor and power density

The design with 36 rotor slots has a power factor of 0.86 while the 24 rotor slots design has a power factor of 0.85. The power density of the 36 rotor slots is also higher at 0.632 Wcm^{-3} compared to the 24 rotor slots design at 0.573 Wcm^{-3}.

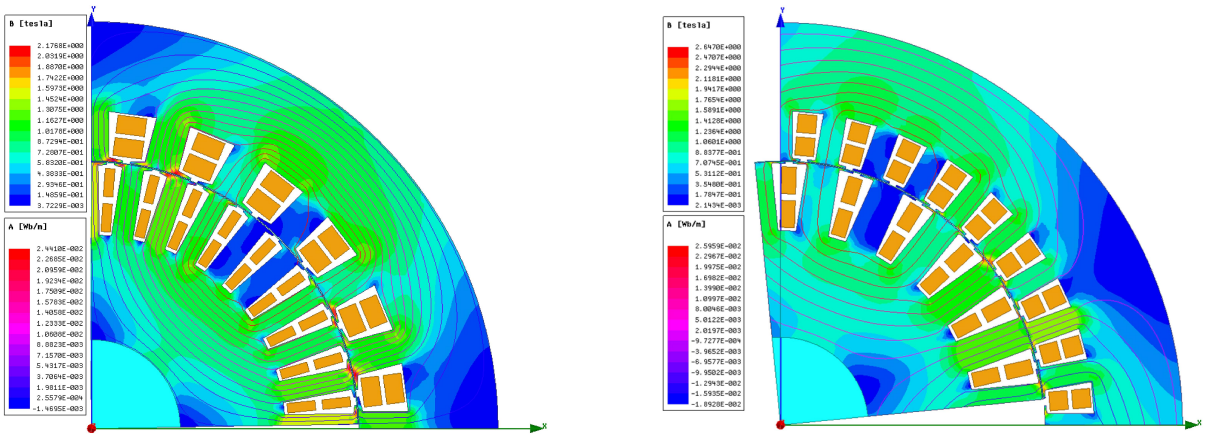

(a) (b)

Figure 5.1: Model flux distribution and flux lines using FEA (a)36 rotor slots model (b) 24 rotor slots model.

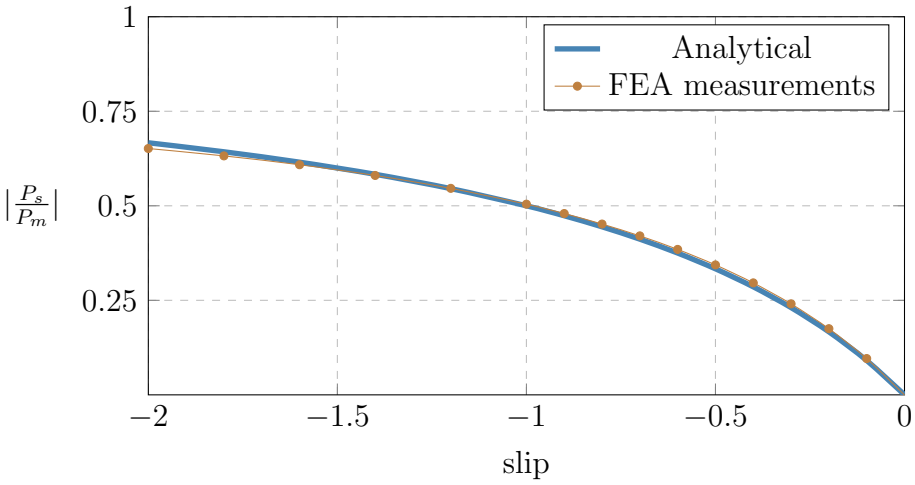

Figure 5.2: Proportion of stator power to the input mechanical power vs slip.

5.2.2 Current and voltage distortions

The current and voltage total harmonic distortions (THD) of the design with 24 rotor slots is lower than the with 36 rotor slots design. The design with 36 rotor slots however has a significantly superior power density, thus the 36-24 (rotor-stator) slot combination is selected for optimization.

The rotor current and induced voltage waveforms of the initial 36 rotor slots design with a 130mm stack are illustrated in Figure 5.3. The rotor current and voltage fast fourier transforms (FFT) are also illustrated in Figures 5.4 & 5.5 respectively. The current waveform and FFT indicate an undesired high current distortion. With the rotor and stator excited by purely sinusoidal waveforms for the FEA as illustrated in Figure 3.7, these distortions are due to space harmonics and need mitigation.

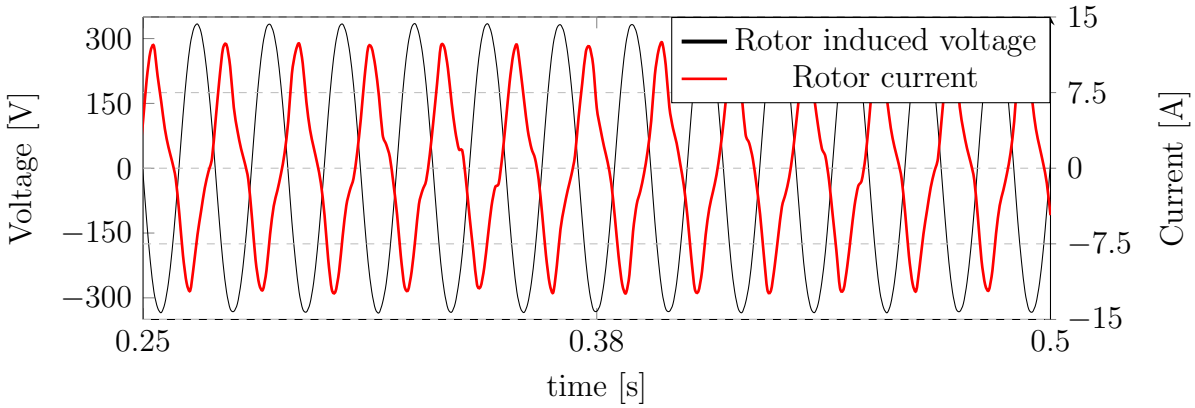

Figure 5.3: Steady state induced voltage and current in the rotor of 130mm stack model.

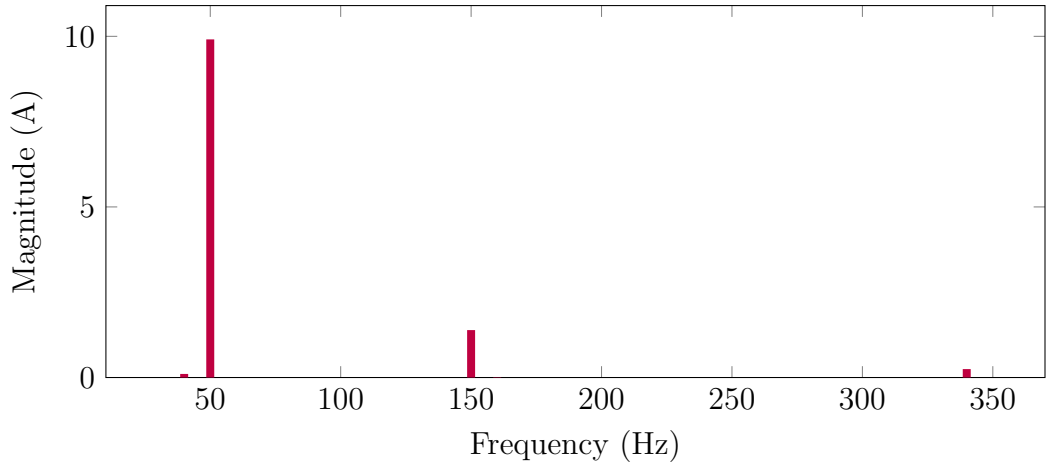

Figure 5.4: Rotor current FFT plot of 130mm stack model.

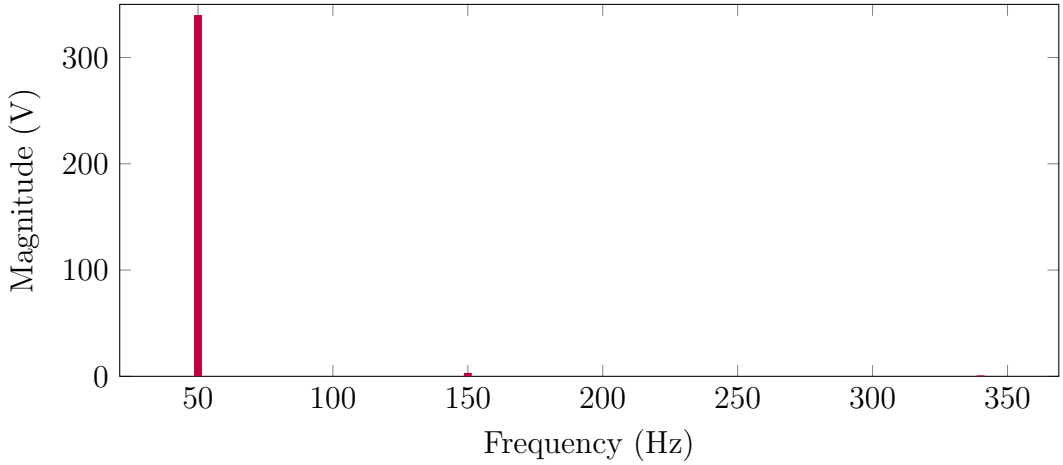

Figure 5.5: Rotor induced voltage FFT plot of 130mm stack model.

5.2.3 Results summary

A summary of the time step 2D-FEA results of the initial models is given in Tables 5.4 and 5.5. A number of experimental designs with 36 rotor slots and 130 mm stack length were tested to be used for a response surface approximate optimization. These experimental designs all had similarly high current distortion values, suggesting a difficulty in reducing the current THD below 5 %. As a result, the machine stack length is increased to 150mm with which an immediate reduction in current and voltage THD is observed. The decision to increase the stack length is influenced by observations in section 4.1.3, which recommend higher aspect ratios (longer stacks) for decreased THDs.

In Table 5.4, the FEA results suggest a significant difference in the power density between the 130mm stack and 150mm stack models. The gap is noticeably shortened when the models are run at unity power factor as seen in Table 5.5. This can be traced to the initially obtained power factors of both models. It is also due to the fact that, although the increase in the stack length increases the machine size, the rotor power is also slightly increased with an increased D^2L.

Table 5.4: FEA summary of initial designs

Items	**Unit**	**36** n_r		**24** n_r	
		130mm stack	150mm stack	130mm stack	150mm stack
Rotor power	kW	4.36	4.47	3.96	4.06
Stator power	kW	1.64	1.64	1.49	1.494
Power factor (Pf)	-	0.862	0.901	0.848	0.897
Power density (PD)	Wcm^{-3}	0.632	0.556	0.573	0.507
Efficiency	%	91.9	92.3	91.8	92.3
Voltage THD	%	1.05	0.56	0.9185	0.522
Current THD	%	14.15	7.8	12.56	7.42

Table 5.5: Unity power factor results of 36 rotor slots design

Items	**Unit**	**Unity power factor**	
		130mm stack	150mm stack
Rotor power	kW	3.92	4.18
Stator Power	kW	1.32	1.4
Efficiency	%	93.4	93.3
PD	Wcm^{-3}	0.55	0.51

5.3 Optimization

The optimization (a shape optimization) is implemented to increase the power density and reduce the harmonic content of the machine without compromising the performance in terms of power factor and efficiency. As explained in section 3.2.7, a response surface approximation of the rotor-tied DFIG FEA model is used with the genetic algorithm. The DOE is developed with FEA samples using a combination of the LHS technique and the composite sampling.

5.3.1 Objective and constraints

The total lamination material volume is used as a reference to the power density, as the rotor and stator have similar stack length. Thus, to increase the power density, a minimize volume objective is applied to the optimizer. The optimization process is also used to ensure that the voltage and current THDs are less than 5%. The THDs are used as constraints because the initial values (in the 36 rotor slots design with 150 mm stack) are already in/close to the desired range, so there is no need to place them as main objectives. The power factor is used as a constraint. The useful slot areas of the rotor and stator are also applied as constraints so that the optimum design does not have a higher impractical slot fill factor. There is no need to use efficiency as a constraint alongside the power factor, because the efficiency cannot be less than the desired value within that power factor constraint range.

5.3.2 Variables selection

The initial machine model was designed with parallel teeth on the rotor and stator. Consequently, the first run of optimization is executed using a variable set comprising of the rotor and stator teeth widths, slot heights and the outer rotor diameter (b_{ts}, b_{tr}, h_s, h_r, D_{ro}). This set is dropped because the current THD constraints were violated in the optimal design. Also from examining DOE samples used in the response surface approximation, none of the samples had a desired current THD value.

The variables are then changed such that the stator/rotor upper and lower slot widths replaced the teeth widths to form a new variables set of (b_{s1}, b_{s2}, b_{r1}, b_{r2}, h_s, h_r, D_{ro}). Using non-parallel teeth proved better for tolerable current distortion values. This is however at the expense of having more variables, which require more DOE samples to create a response surface. The increased number of DOE samples extends the total optimization time. In spite of this, the time taken is less than using FEA directly to execute the optimization.

The rotor (inner) and stator (outer) diameters are kept constant alongside the stack length. Although the stator inner diameter is not fixed, it is directly related to the rotor outer diameter because the air-gap length is fixed, thus there is no need to use as a variable. The number of turns in the rotor and stator are also fixed. The variables used for the optimization are illustrated in Figure 5.6.

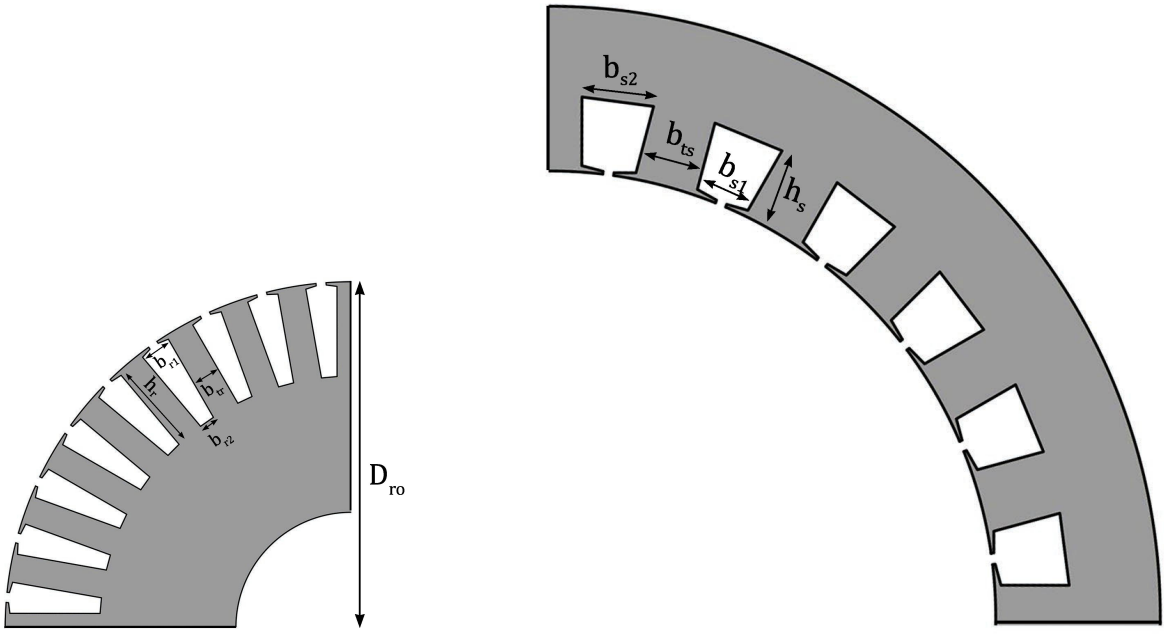

(a) (b)

Figure 5.6: Optimization input dimension variables (a)Rotor (b) Stator.

5.4 Optimization results

A summary of the optimal design results is given in Table 5.6. The power density of the machine is increased by 3.33 %. There is also a significant reduction in the current THD from 7.8 % to 3.13 %. The voltage THD is reduced from 0.56 % to 0.22 % while the power factor remains constant.

Figure 5.7 shows the actual vs predicted plots for the approximate responses (objective and constraints) used in the optimization process as obtained in VisualDoc. As shown in Table 5.6 and Figures 5.7(a) and 5.7(b), it can be observed that the estimated values of the stator/rotor slot areas and the machine volume very similar to the analytical calculations given the linear nature of their responses to the optimization variables.

The estimated optimum value for the current distortions has the largest deviations from the actual FEA value. Having the same "unit", it can be seen that the range for current distortion is much wider than that of the voltage distortion which accounts a bit for the difference in accuracy. The current distortion estimation error is however at tolerable level and the actual FEA value falls very much within the desired range specified.

The rotor current and induced voltage of the optimized design as obtained by FEA are illustrated in Figure 5.8. The rotor current FFTs of the initial design model with 130mm stack and the optimized design obtained by FEA are compared as illustrated in Figure 5.9. A substantial reduction in the magnitude of the harmonic content is observed for the optimized design. The initial design has a higher fundamental magnitude because of the lower power factor. The optimized design shape in comparison to the initial design shape is illustrated alongside the flux distribution plots and flux lines in Figure 5.10.

Table 5.6: Optimal design results

Parameters		**Unit**	**Initial model**	**Range**	**Optimum** (Approx)	(FEA)
Input variables	b_{s1}	mm	10.11	8.5 - 11.2	8.26	
	b_{s2}	mm	13.26	12 - 14.5	13.92	
	b_{r1}	mm	6.35	6 - 8	6.13	
	b_{r2}	mm	2.9	1.5 - 3.5	1.76	
	h_s	mm	11.98	10 - 15	13.4	
	h_r	mm	19.75	18 - 35	34.9	
	D_{ro}	mm	144	135 - 165	160	
Objective	Volume (minimize)	cm^3	10937	< 10937	10240	
Constraints	Stator slot area	mm^3	140.1	≥ 140.1	148.6	
	Rotor slot area	mm^3	92	≥ 92	137.7	
	Voltage THD	%	0.56	≤ 5	0.19	0.22
	Current THD	%	7.8	≤ 5	3.49	3.13
	Power factor	-	0.9	≥ 0.86	0.9	0.9
PD (at unity Power factor)		Wcm^{-3}	0.51			0.527

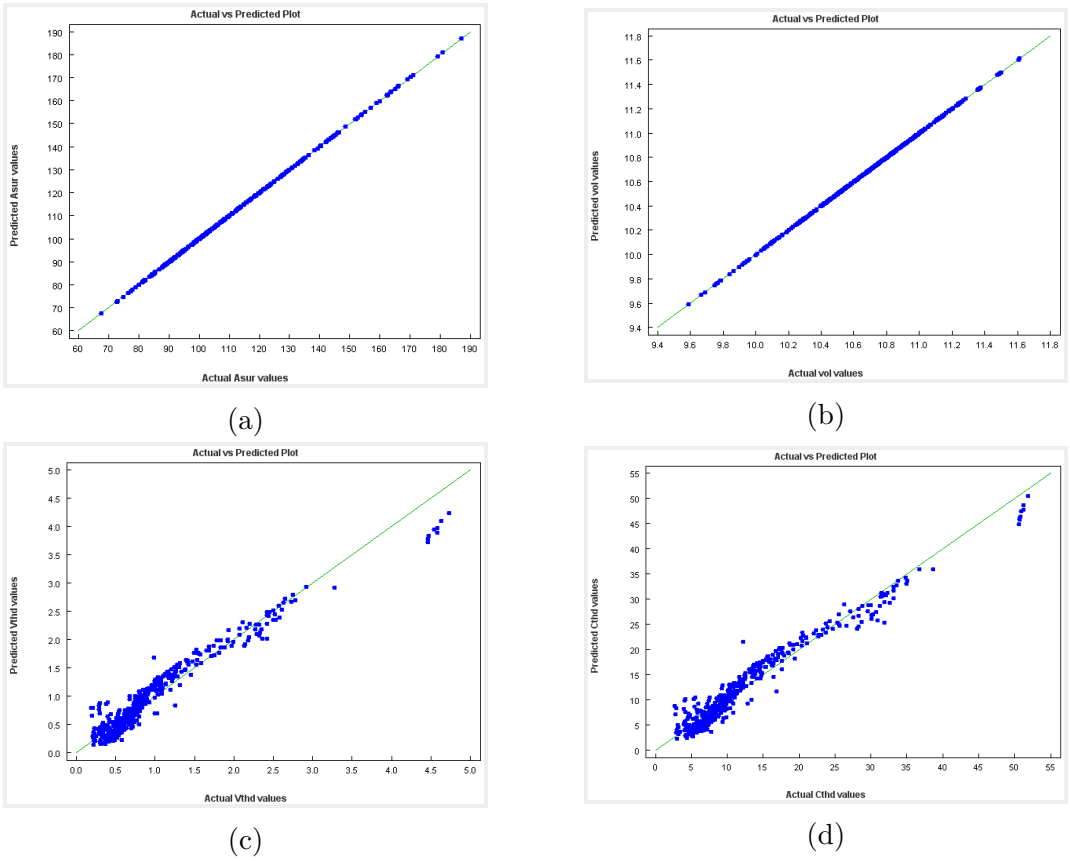

Figure 5.7: Actual vs Predicted plots: (a) Rotor slot area (mm^2), (b) Machine volume ($10^3 cm^3$), (c) Rotor voltage total harmonic distortion (%), (d) Rotor current total harmonic distortion (%).

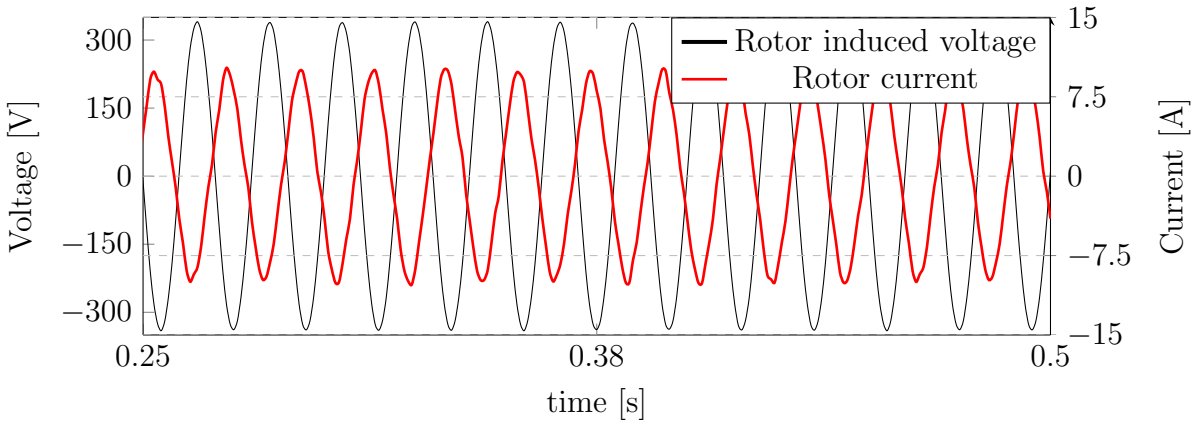

Figure 5.8: Steady state induced voltage and current in the rotor of optimized model.

The torque production (and ripple) of the optimized model is illustrated in Figure 5.11.

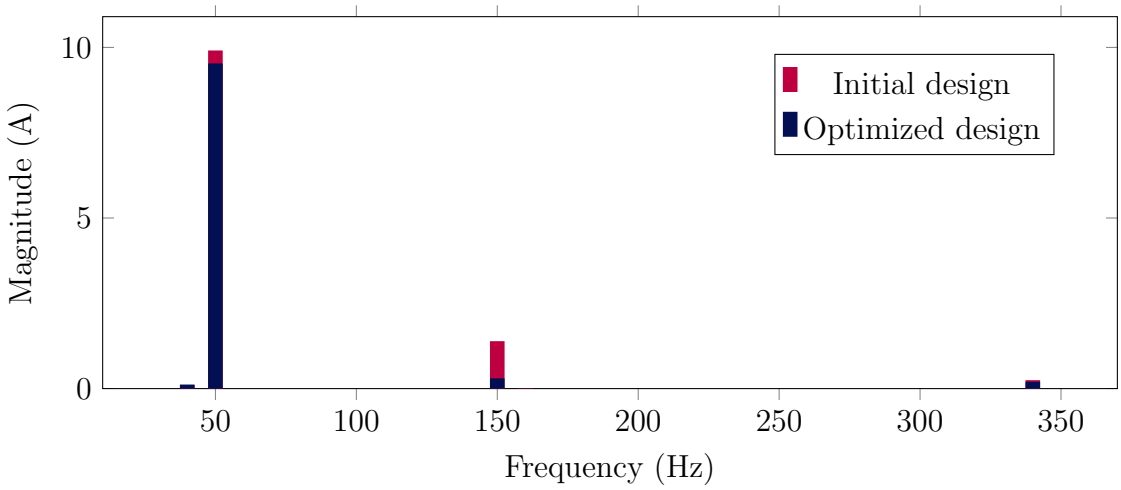

Figure 5.9: Current fft of initial and optimized design

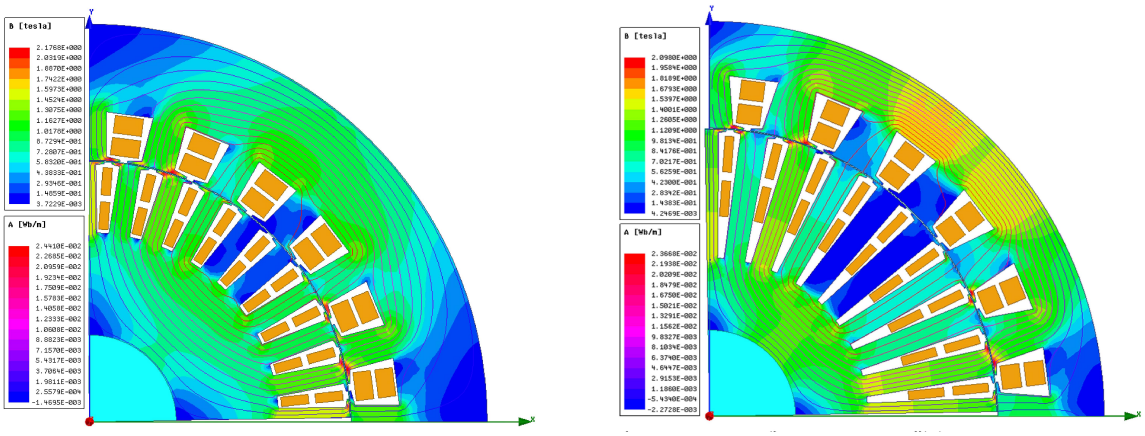

(a) (b)

Figure 5.10: (a) Intial design (b) Optimized design.

5.4.1 Skewed torque

Figure 5.11(a) shows the electromagnetic torque production of the unskewed optimized design. The unskewed machine torque ripple is too high and can shorten the machine life span. The common practice is to skew the rotor by one stator slot pitch to reduce the torque ripple in the machine [12].

The effects of skewing on the machine was simulated using the "Multi Slice Model" method [1] as given in [39]. Using this method, a finite number N_{sl} of the machine model slices are simulated. In each slice, the rotor is placed at an initial angle γ calculated as follows:

$$\gamma^i = \frac{\theta_{sk}(2i - N_{sl} - 1)}{2N_{sl}}, (i = 1, ..., N_{sl}), \tag{5.1}$$

where, θ_{sk} is the total skew angle (taken as the full stator slot pitch angle).

[1] The Skewing functionality is present in the more recent releases of ANSYS Maxwell ($\geq v17.1$)

The aggregate of the induced torque of the simulated slices is used to evaluate the effects of skewing. There is a significant reduction in the ripple in the skewed design as illustrated in Figure 5.11(b). The torque shown in Figure 5.11 has a positive value which differs from the negative torque polarities indicating generating modes for induction machines, but is however in line with section 2.2 and Figure 2.2(b).

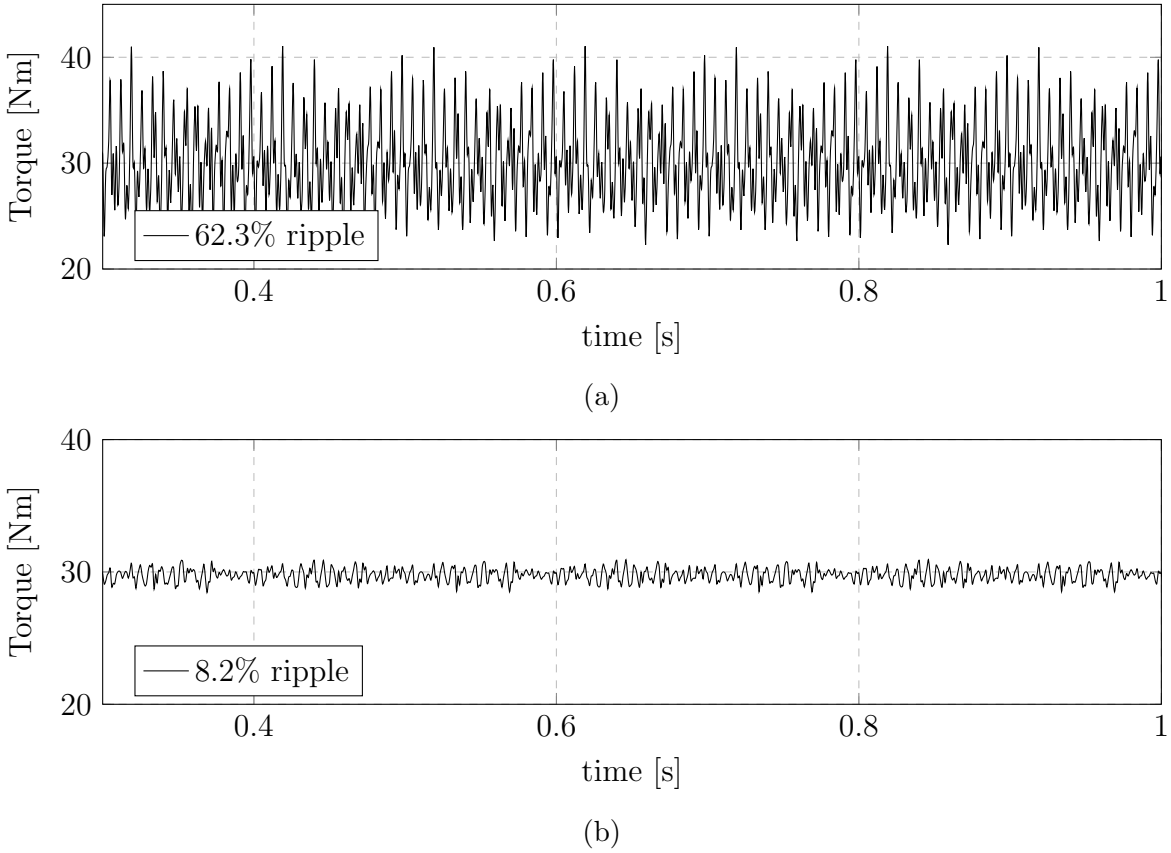

Figure 5.11: Optimization model torque (a)Unskewed (b)15^0 rotor skew.

5.5 Summary

The design and optimization of a 5.5 kW rotor-tied DFIG is discussed in this chapter and a summary is given as follows:

- Two rotor to stator slot combinations were used to obtain initial designs for the 5.5 kW rotor-tied DFIG
- FEA of the initial designs was performed to evaluate the power density, power factor, efficiency and harmonic content.
- The design with higher rotor to stator slots was selected because of its higher power density.
- An optimization of the selected initial design to increase the power density and reduce harmonic content using a full quadratic response surface approximation of FEA models with a genetic algorithm was executed.
- The response surface approximation was developed from a combination of LHS and composite samples.

Chapter 6

Prototype Construction and Test Bench

In this chapter, the prototyping process of the optimized 5.5 kW rotor-tied DFIG in chapter 5 is discussed. A standard 132M induction machine frame is used with an already designed shaft. The shaft is modified to skew the rotor laminations and place the slip ring and brush assembly outside the frame end-plates. Although the rotor and stator lamination shapes are based on the optimized design in chapter 5, extra features are added for adaptation while stacking, and these are described.

The prototype is to be tested in the sub-synchronous, synchronous and super-synchronous regions of operation. The various equipment to be used in the prototype test bench are highlighted with their functions stated.

6.1 Prototype assembly process

An image of the 132M IM frame is shown in Figure 6.1, which is used alongside a pre-designed shaft for the rotor-tied DFIG prototype. The frame and shaft predetermined both the outer stator diameter, D_{so}, and the inner rotor diameter, D_{ri}, respectively. Although 132M frames (generally used for 7.5kW, 4 pole IMs) have similar outer stator diameters with their 132S counterparts (used for 5.5kW, 4 pole IMs), they have longer stacks which is more suitable for the DFIG design, hence the frame size choice. The cost of these frames are also lower than slip ring motor frames.

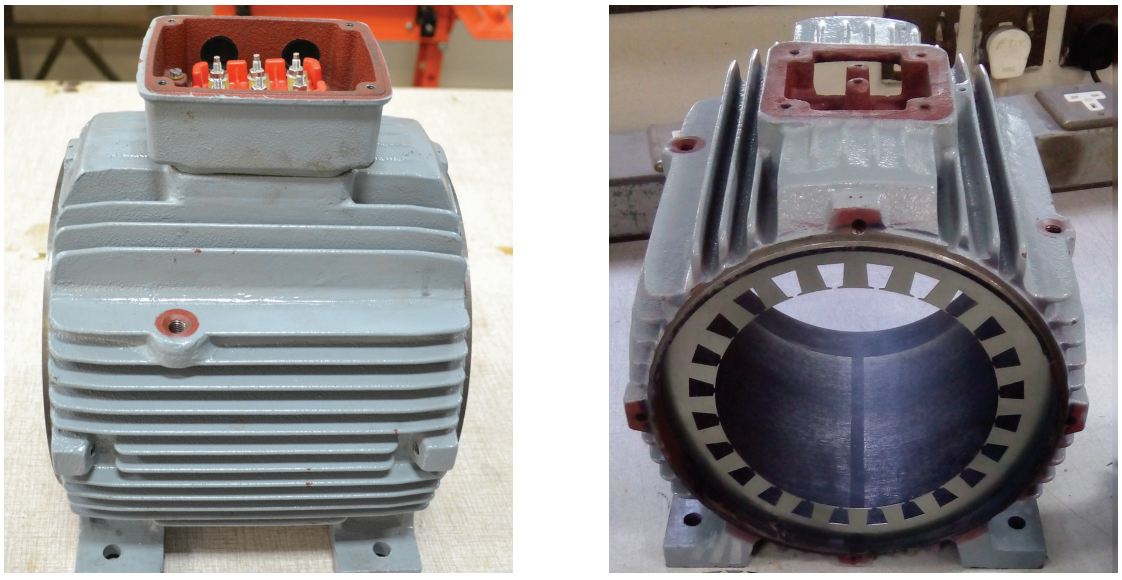

(a) (b)

Figure 6.1: 132M induction motor frame.

6.1.1 Shaft modification

The shaded mechanical drawing of the shaft used is illustrated in Figure D.1. To skew the rotor, the shaft is modified by cutting a slanting keyway across the top. The keyway is cut at a 15^0 angle as illustrated in Figures D.2 & D.3. The keyway is not cut across the whole stacking length of the shaft to prevent the rotor laminations from sliding out at the back.

There was no shaft space for the slip rings inside the machine frame, therefore a decision to place the slip rings at the back-end of the shaft is made. A slot to line out the cables from the rotor windings under the bearing to the slip rings is cut out as illustrated in Figures D.2 & D.3.

6.1.2 Stator laminations and stacking

M530-65A steel with 0.65mm thickness is used for the stator laminations. An image of a single stator lamination is shown in Figure 6.2, while an annotated mechanical drawing of the stator lamination is illustrated in Figure D.4. The stator lamination dimensions are according to the optimized design given in chapter 5. Small slots are cut out at the top of the stator laminations to assist with the alignment while stacking.

The stator laminations are first stacked on a pipe and pressed using an hydraulic press. An image of the pressed stator stack on the pipe is shown in Figure 6.3(a). A stacking factor of about 0.98 is achieved for the stator laminations. The frame is heated to temporarily increase the size, after which the stacked laminations are pushed in. Following the fitting of the stator stack, the frame is allowed to cool and return to its original size. A picture of the stator stack inside the frame is shown in Figure 6.3(b).

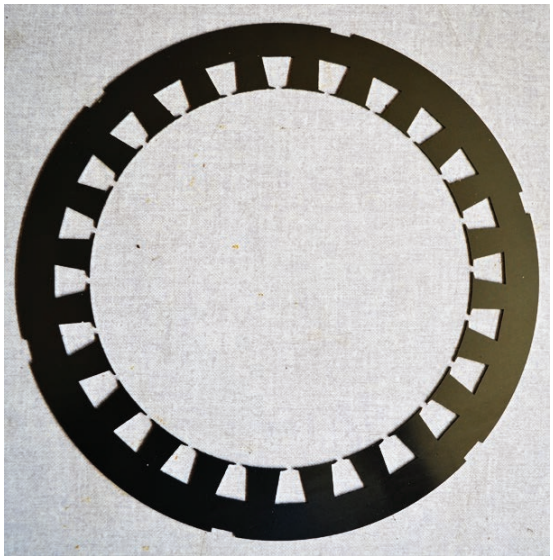

Figure 6.2: Stator lamination.

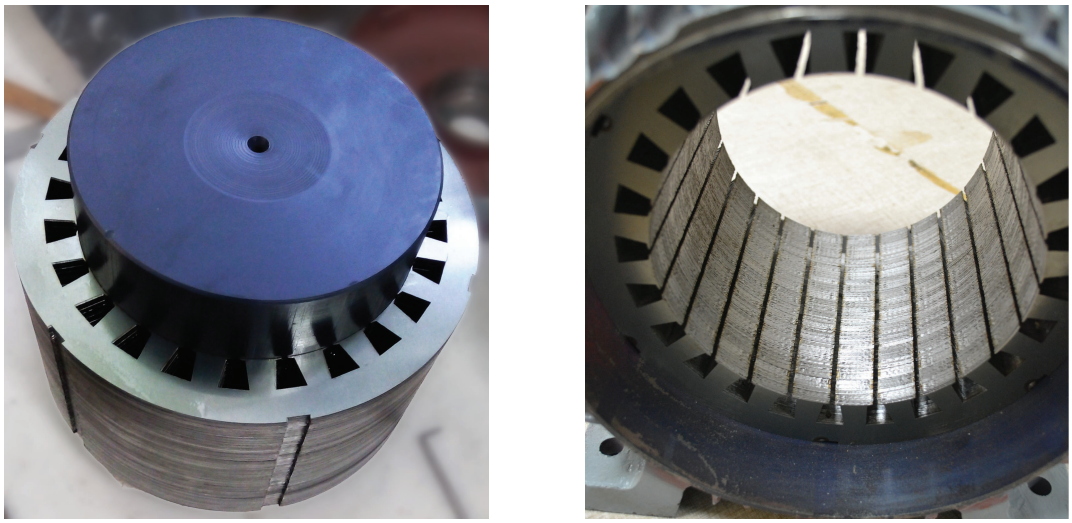

(a) (b)

Figure 6.3: (a) Stacked stator laminations on pipe (b) Stacked stator laminations in shrink fitted frame.

6.1.3 Rotor laminations and stacking

The M530-65A steel with 0.65mm thickness is also used for the rotor laminations. An image of a single rotor lamination is shown in Figure 6.4, while an annotated mechanical drawing of the rotor lamination is illustrated in Figure D.4. Keying protrusions are cut with the rotor laminations for both alignment and fitting on the shaft. The key is cut according to mechanical standards based on the shaft diameter.

The stacking process of the rotor laminations is illustrated in Figure 6.5. A steel end-plate shaped like the rotor laminations is first press fitted on the shaft on which the laminations are stacked against as illustrated in Figure 6.5(a). The laminations are pressed together as illustrated in Figure 6.5(b) with an hydraulic press as was done with the stator stack. Another end-plate is fitted on the lamination stack when the desired stack length is reached. The end-plates are used to provide support for the laminations.

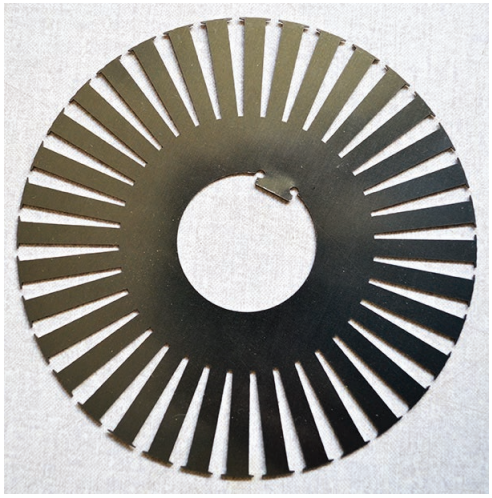

Figure 6.4: Rotor lamination

The keyway cut across the shaft terminates with a round edge which causes an imbalance with the end-plate position at that edge. This consequently affected the whole rotor stack alignment. To correct this, a properly aligned steel ring is shrink fitted at the side of the keyway with the round edge as shown in Figure 6.5(c). The ring is used as a shoulder for the alignment of the laminations. The stack is then carefully pressed from the ring unto a circlip. The circlip is used to hold the rotor stack and end-plates in place and prevent them from sliding across the keyway at the shaft front end as shown in Figure 6.5(d).

A stacking factor k_{fe} of just slightly above 0.98 is also achieved rotor laminations.

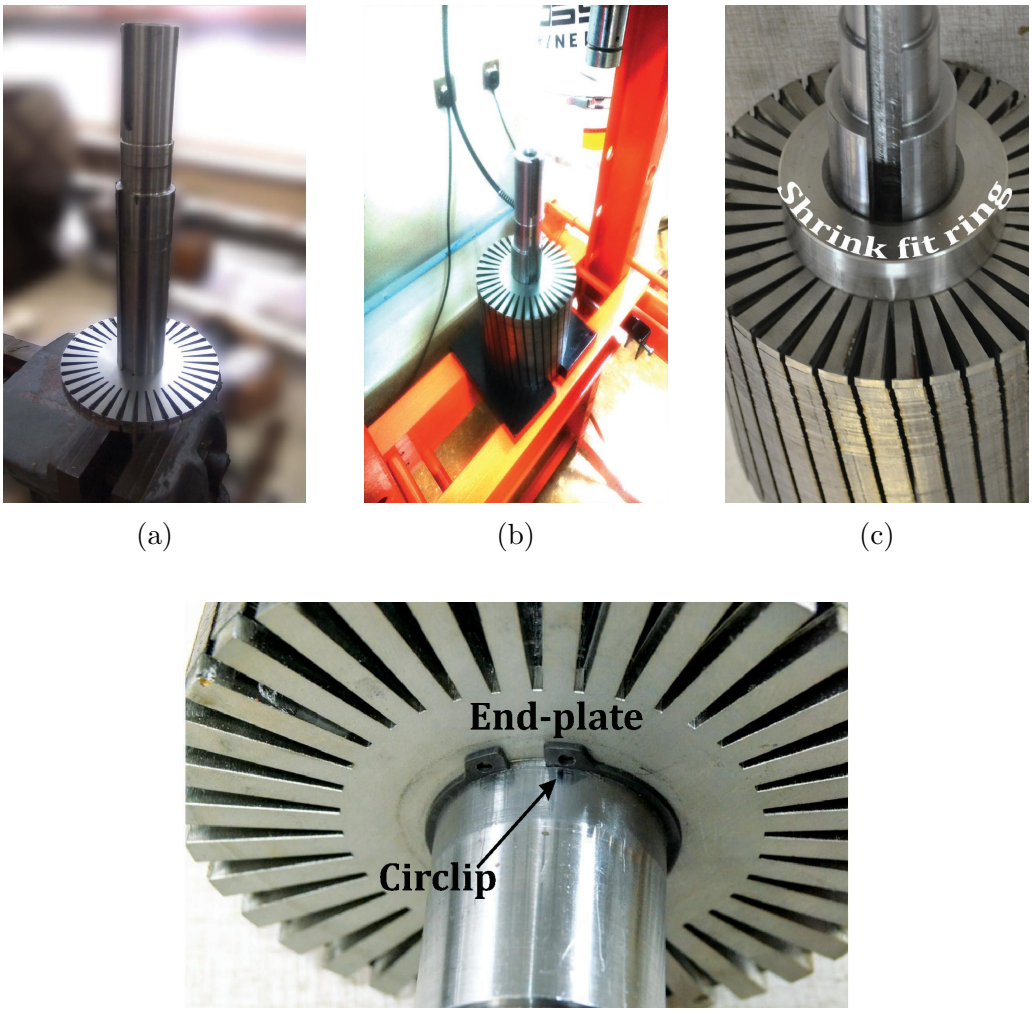

(a) (b) (c)

(d)

Figure 6.5: (a) Slide fitting rotor laminations on the shaft (b) Stacked rotor laminations being pressed (c) Stacked rotor laminations with shrink fit ring for alignment (d) End plate and circlip.

6.1.4 Winding

The stator is wound according to Table 5.2 with 48 turns per slot leading to 192 turns per phase at a coil pitch of $\frac{5}{6}$. Similarly, the rotor is wound with 28 turns per slot leading to 168 turns per phase at a coil pitch of $\frac{7}{9}$. The rotor slot shape posed some challenges with achieving the design fill factor. Also, in the process of skewing the rotor laminations, there were some irregularities in the slots which needed filing to ensure that the insulation coatings on the conductors were not peeled off during winding. Pictures of the fully wound stator and rotor parts are shown in Figure 6.6 & Figure 6.7 respectively.

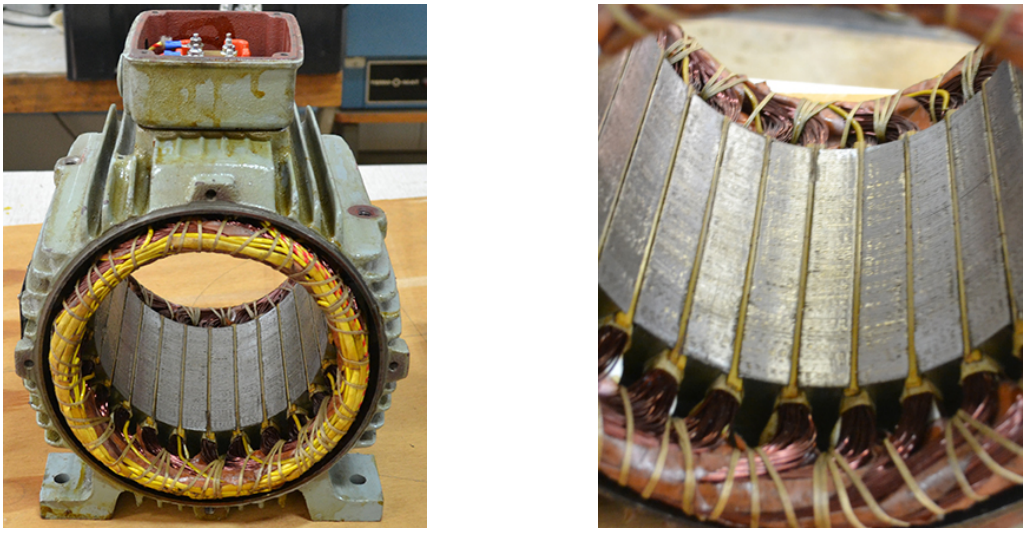

(a) (b)

Figure 6.6: Fully wound stator (a) Full view (b) close-up view of the windings.

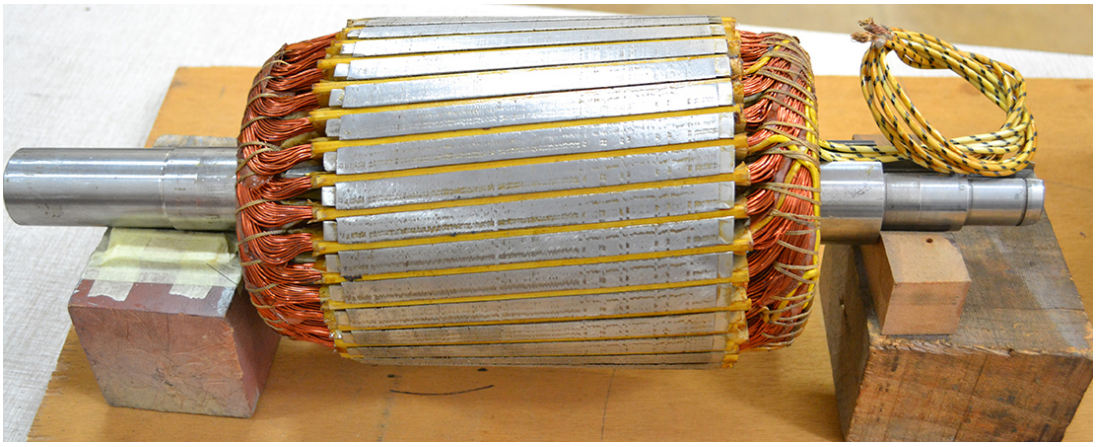

Figure 6.7: Full view of wound rotor.

6.1.5 Complete assembly

After the rotor is placed inside the frame with the bearings, there is a need to fix a slip ring and brush assembly for the rotor windings on the prototype. As seen in Figure 6.7, the rotor stack occupies most of the shaft between the two bearings, and there is no room for the slip ring and brush assembly, thus it is placed outside the frame end-plates. The rotor wires are passed through the slot cut out on the shaft and connected to the slip rings. The slip rings are shrink fitted on at the back end of the shaft outside the frame and a rod fastened to the frame end-plates is used to hold it in place. Pictures of the fitted slip rings and brush assembly for the rotor windings are shown in Figure 6.8. Pictures of the complete prototype assembly are shown in Figure 6.9.

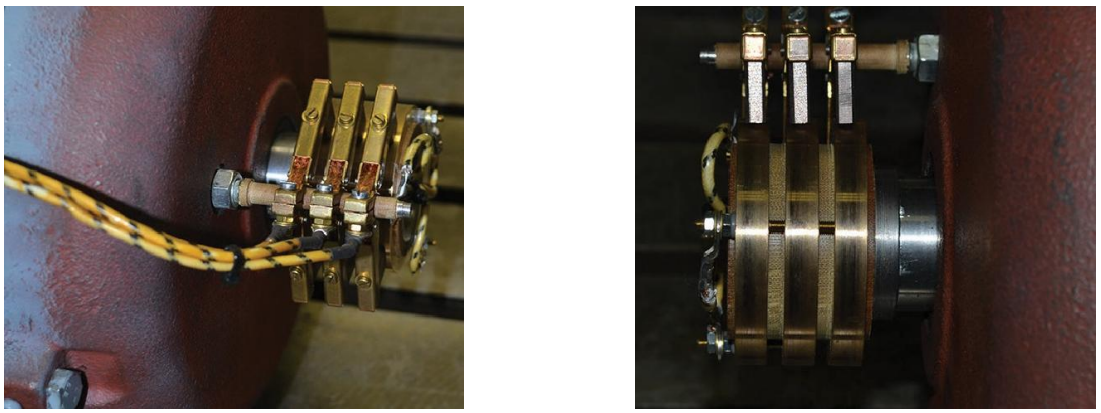

(a) (b)

Figure 6.8: Slip ring and brush assembly (a) top view (b) side view.

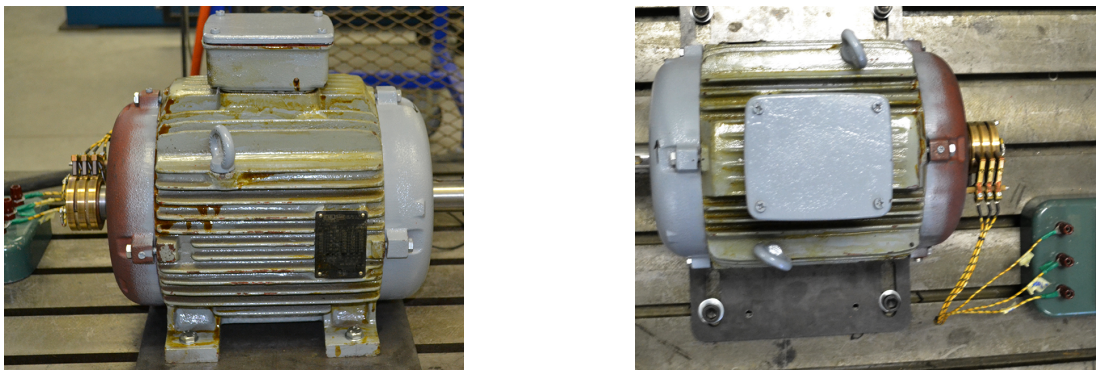

(a) (b)

Figure 6.9: Complete prototype (a) side view (b) top view.

6.2 Test bench

Schematic diagrams of the test bench are illustrated in Figure 6.10. An 11 kW induction motor is used as a prime mover to drive the 5.5 kW rotor-tied DFIG prototype in the place of a wind turbine.

A Lorenz Messtechnik GmbH 500Nm torque sensor is connected in between the 11 kW motor and the rotor-tied DFIG prototype by propeller shafts. The torque sensor is to be used to monitor the input mechanical power from the 11 kW motor into the prototype. It should be ensured that all connections are grounded especially from the AC drives as they can severely interfere with the torque sensor. The propeller shafts are used to balance any non-alignment between the coupled machines. An image of the connection of the prototype, torque sensor and 11 kW motor is shown in Figure 6.11. The 11 kW motor is powered with an Allen-Bradley PowerFlex 755 AC drive shown in Figure 6.12. The drive is used for speed control of the 11 kW motor.

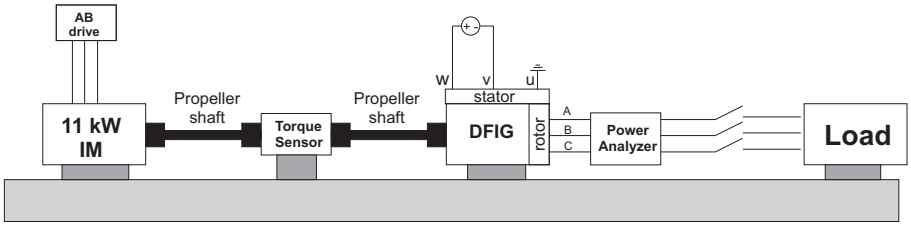

(a)

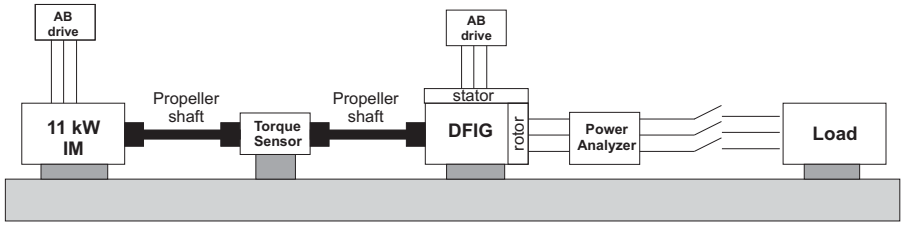

(b)

Figure 6.10: (a) Bench schematic at synchronous speed (b) Bench schematic at slip speeds.

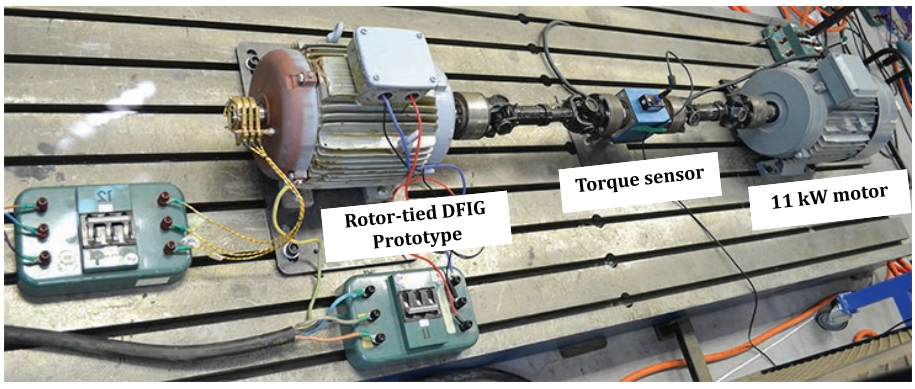

Figure 6.11: Prototype test bench setup

For tests at synchronous speed, a DC power supply is connected to two of the stator terminals from a 185 VDC source controlled by a variac as illustrated in Figure 6.10(a). For tests at other speeds the stator terminals are connected to an Allen-Bradley PowerFlex 700 AC drive shown in Figure 6.12 to provide slip frequency excitations as illustrated in Figure 6.10(b).

A purely resistive load is connected to the rotor terminals. The load is a bank of heating elements with resistances of 18 Ω each. Three sets of two of heating elements connected in series are combined to form a balanced three phase load rated at 6 kW. A Norma 5000 power analyzer which measures the induced voltages, currents, frequency, output power, power factor, current and voltage THDs of the prototype at the rotor side is connected with the load to the rotor terminals (in parallel as regards voltage and in series for current measurements). A Tektronix DPO 3014 oscilloscope is also used to capture the waveforms of the prototype outputs. An image of the power analyzer and oscilloscope is shown in Figure 6.13.

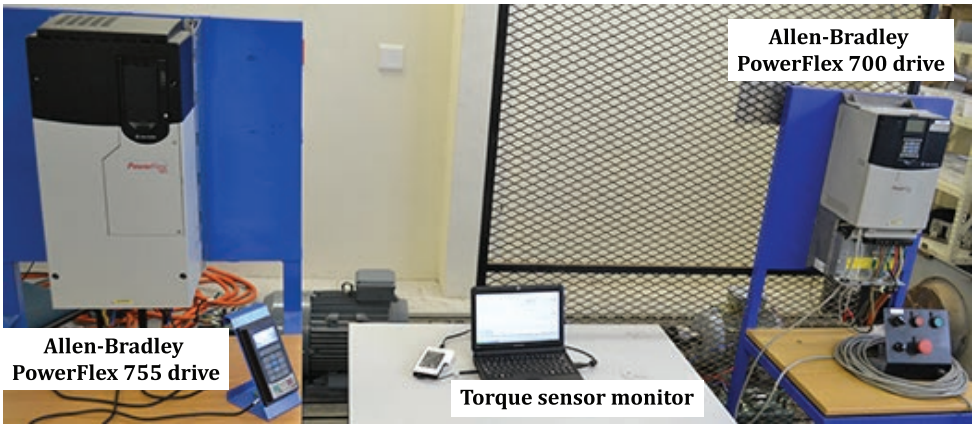

Figure 6.12: AC drives and torque sensor monitor

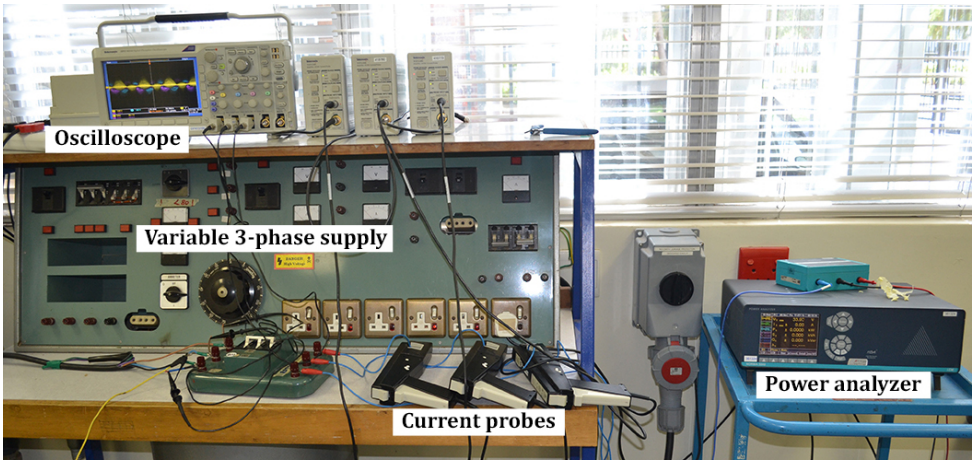

Figure 6.13: Oscilloscope and power analyzer

6.3 Summary

The prototyping process of a 5.5 kW rotor-tied DFIG was discussed in this chapter alongside the test bench used in testing the prototype. The crucial points in this chapter are as follows:

- A 132M frame and pre-designed shaft is used for the prototype. The shaft is modified slightly to enable skewing of the rotor laminations and the placement of the slip rings and brush assembly outside the frame end-plates.
- Challenges were encountered with mis-alignment of the rotor laminations on the shaft, and the method used to solve this was discussed.
- A description of the prototype test bench is given with illustrations of all the equipment used and their functions.

Chapter 7

Rotor-tied DFIG Testing

In this chapter, the machine equivalent circuit parameters (resistances and reactances) are first estimated from parameter tests. The parameter tests results are compared with calculated values from analytical estimations given in [12].

DFIGs operate in three broad regions: the sub-synchronous region, the synchronous region and the super-synchronous region with regards to the mechanical rotational speed. In the absence of a specific control system, the prototype is tested in a standalone mode. The stator windings are excited by either a DC source at synchronous speeds, or by an AC drive supplying slip frequency excitation at other speeds. The rotor is connected to a resistive load.

7.1 Machine parameter tests

The phase resistances of the stator and the rotor are determined by simple DC resistance tests and compared with analytical estimations. An open circuit test is then carried out to confirm the turns ratio in the machine. This is conducted by connecting the rotor to the variable three phase supply and the voltage is increased to the rotor rated voltage (230 V_{ph}). The measured stator voltage is then used to verify that the turns ratio is according to the design specifications. The measured and analytical resistances and turns ratio are given in Table 7.1.

The inductances (magnetizing and leakage) are obtained from modified no load and blocked rotor tests. The no load test is conducted by applying rated voltage to the rotor terminals and short-circuiting the stator terminals. The prototype is then allowed to rotate as a motor till its full no-load speed is attained. The machine settles around a speed of 1496 rpm at no load.

The modified blocked rotor test is performed by short-circuiting the stator terminals and clamping the rotor to prevent rotation. The rotor voltage is steadily increased till the rated current of the rotor is reached and the power is measured. The results of the no-load and blocked rotor tests are given in Table 7.2 and the calculated reactances are given with the analytical estimations in Table 7.3.

Table 7.1: Winding resistances and turns ratio

Parameters	**Unit**	**Analytical**	**Measured**
Rotor phase resistance, R_r	Ω	1.9	1.85
Stator phase resistance, R_s	Ω	2.5	2.1
Turns ratio	-	0.85	0.86

Table 7.2: Parameter test results

Parameters	Unit	No-load test	Blocked rotor (test)
Rotor voltage, V_r	V	230	40.3
Rotor current, I_r	A	2.87	5.96
Power	W	250	306
Power factor, $\cos\varphi$	-	0.125	0.42
Speed, Ω_m	rpm	1496	0

Table 7.3: Calculated Inductances

Parameters	Unit	Analytical	Measured
Magnetizing inductance, L_m	H	0.2	0.257
Leakage Inductance, L_l	H	0.0121	0.0188

7.2 Standalone rotor-tied DFIG tests

The prototype performance tests are conducted such that the prototype is rotated at specific speeds by the 11 kW motor, and voltage sources at different frequencies corresponding to the mechanical rotational speeds are connected to the stator. Preliminary tests are conducted with the rotor windings open-circuited as a safety measure to ensure proper configurations before the machine is loaded. The frequencies of the induced voltages on the rotor terminals are observed. The tests are also used to check for balance in the induced voltages at the rotor windings demonstrated.

The first of the initial tests is carried out at synchronous speed (1500 rpm), and DC of the same magnitude but different polarities is fed into two phases of the stator. The prototype is again rotated at a sub-synchronous speed and a three phase voltage source at a positive slip frequency is fed into the stator terminals. The final of these set of tests is conducted with the prototype rotated at a super-synchronous speed and the voltage source at the stator terminals has a negative slip frequency.

The slip frequency voltages are supplied by running the Allen-Bradley PowerFlex 700 drive in the adjustable voltage motor control mode. The frequency ramp rates are set to zero, and the minimum and maximum frequencies are fixed at the desired slip frequency. This way, a slip frequency can be fixed at the drive output with the voltage magnitude varied to control the amount of current into the stator. Altering the polarity of the slip frequencies is implemented by changing the phase sequence of the wiring to the stator (swapping any 2 phases).

The Allen-Bradley PowerFlex 700 drive is controlled by an analog input and even when the analog input is at a zero reference value, there is a small excitation present which is seemingly DC in nature as it induces a voltage at the rotor side at the frequency of the mechanical rotation. This excitation is superimposed by the fundamental frequency set for the drive once the voltage magnitude is cranked up.

7.2.1 Loaded rotor tests

After successfully testing the prototype with the rotor terminals open-circuited, the next set of tests is to apply a load at the terminals at the same speeds. The resistive load described in section 6.2 is used.

The test at synchronous speed is first conducted with DC applied to the stator terminals. A schematic diagram of the test bench for the test at synchronous speed is illustrated in Figure 7.1. The power analyzer is connected in between the rotor terminals and the loads to monitor the induced voltages, currents, power output and THDs in the rotor. The Allen-Bradley PowerFlex 755 drive is used to run the 11 kW motor at 1500 rpm and the DC from the variable DC supply is fed to two phases in the stator. The input power is obtained from the torque sensor in the drive train.

The prototype is tested in the sub-synchronous region at 975 rpm. A schematic diagram of the test bench for the tests at sub-synchronous speeds is illustrated in Figure 7.2. Slip frequency is applied to the stator terminals via the Allen-Bradley PowerFlex 700 drive with the rotor terminals connected as in the synchronous speed test. The drive voltage is gradually adjusted till the rated stator current is reached. The powers from the torque sensor and power analyzer are then measured alongside the power supplied to the stator windings.

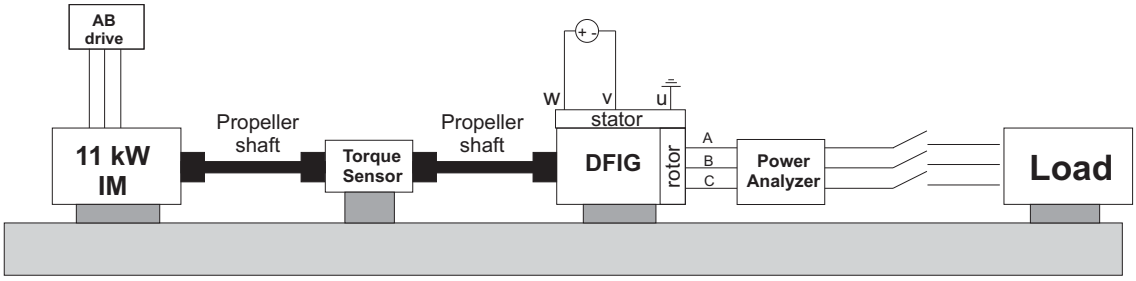

Figure 7.1: Schematic of test bench for the synchronous speed test

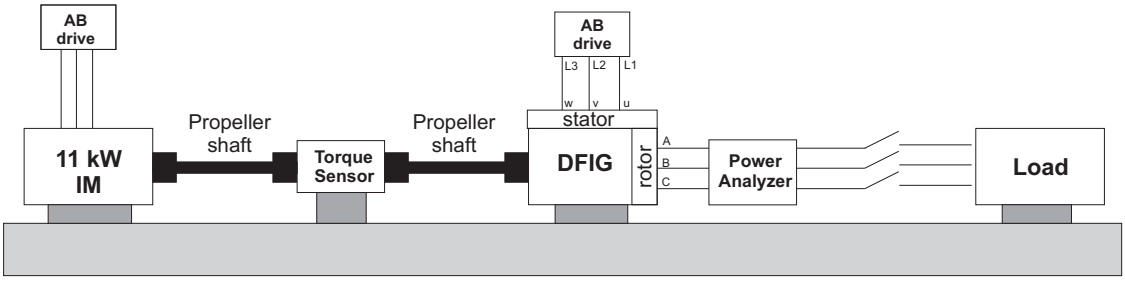

Figure 7.2: Schematic of test bench for sub-synchronous speed test

For the tests at super-synchronous speeds (1650 rpm and 2025 rpm), the connections at the rotor side remain unchanged while two phases in the stator terminals are swapped to change the phase sequence and alter the frequency polarity of the stator excitation. A schematic diagram of the test bench for the tests at super-synchronous speeds is illustrated in Figure 7.3. At super-synchronous speeds, the AC drive connected to the stator terminals works in a regenerative region, which raises the DC bus voltage of the drive. The DC bus of the drive used has a voltage threshold of 750 V, and an external dynamic brake resistor is installed to absorb the extra power. Three elements from the resistive load are combined to form the external resistor.

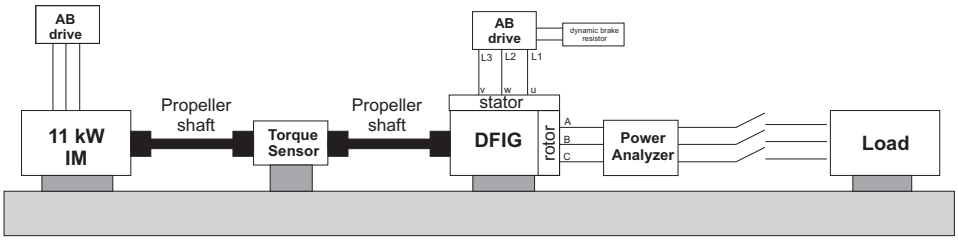

Figure 7.3: Schematic of test bench for super-synchronous speeds tests

7.2.2 Synchronous speed test results

Rated DC of 7A current is first applied at the stator side at synchronous speed, which induces a voltage at the rotor of about 210 V and current of 5.72A. The reason for using 7A is due to the rated stator AC value of $5.65A_{rms}$. The instantaneous algebraic sum of alternating currents in the stator is about 14A at a rated value of $5.65A_{rms}$. Also at a rms value of 5.65 A, the peak stator AC is 8A, and in accordance with section 3.2.6, the DC currents at the two stator terminals are $\frac{8\sqrt{3}}{2}$A and $\frac{-8\sqrt{3}}{2}$A. The efficiency of the prototype with 7A on the stator is about 85.8 % with current and voltage THDs of about 2 % each. The induced voltage and current waveforms in the rotor with 7A on the stator are illustrated in Figure 7.4. The induced voltage is compared with FEA results of the optimized design simulated in a standalone mode. The standalone mode is simulated by using the external circuit feature in Ansys Maxwell. The measured induced voltage and the FEA voltage are illustrated in Figure 7.5.

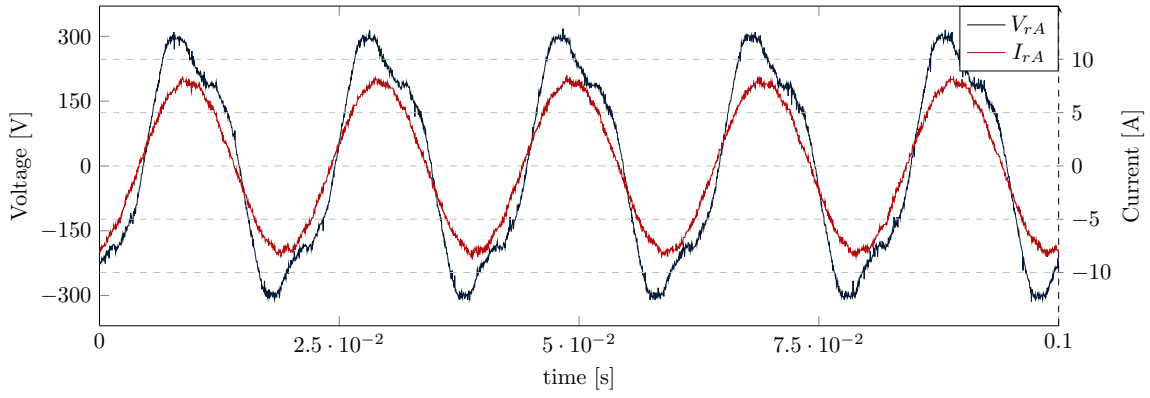

Figure 7.4: Rotor induced voltage and current at synchronous speed (7A)

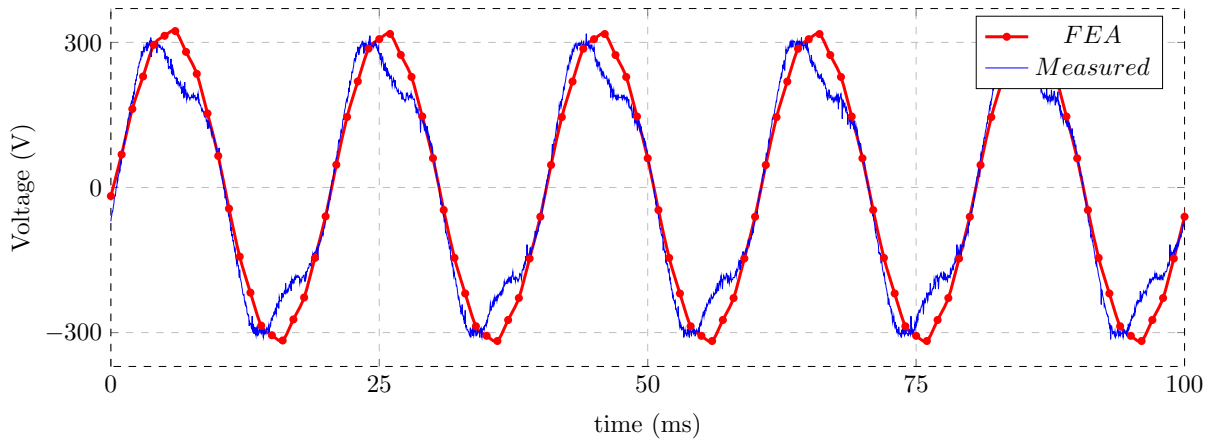

Figure 7.5: FEA and measured rotor induced voltages at synchronous speed (7A)

Other tests at the synchronous speed are conducted with varying stator phase currents. The efficiency of the prototype generally increased with the magnitude of the stator current as illustrated in Figure 7.6. At a stator phase current of 8A, the induced rotor phase voltage and efficiency of the prototype are 235V and 87 % respectively, while the voltage induced on the rotor and efficiency at a stator current of 1A are 33.7V and 26% respectively. A summary of the results at synchronous speed with different stator currents is given in Table 7.4.

The waveform of the voltage from the DC source at 8A is compared with the induced rotor voltage as illustrated in Figure 7.7. The three phase induced voltages on the rotor at synchronous speed are illustrated in Figure 7.8. The induced voltage and current in rotor with 8A on the stator are illustrated together in Figure 7.9.

The induced voltage on the rotor with 8A on the stator is also compared with FEA results of the optimized design simulated in a standalone mode. The measured induced voltage and the simulated results are illustrated in Figure 7.10. The results of the prototype with 8A on the stator are highlighted because the induced voltage on the rotor at this current is closest to the rated rotor voltage.

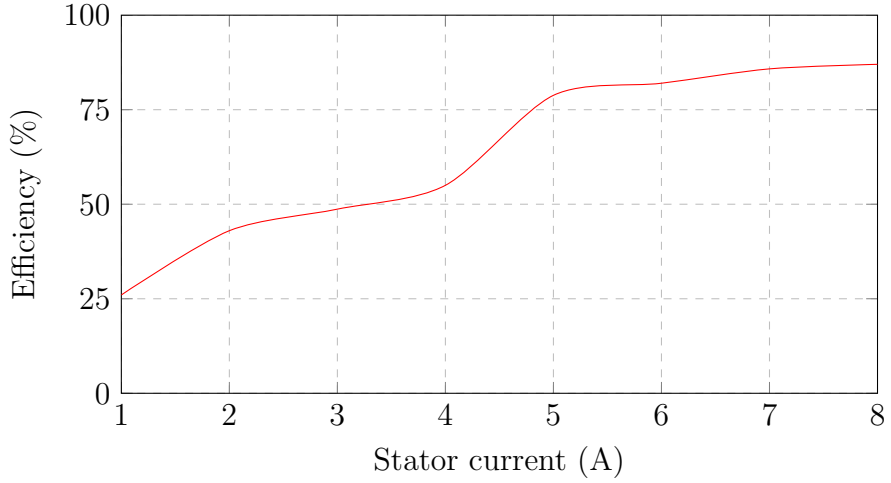

Figure 7.6: Efficiency of generator at synchronous speed with different stator currents

Table 7.4: Synchronous speed test results at different stator currents

Parameters	**Unit**	**Stator current (A)**							
		1	2	3	4	5	6	7	8
Rotor phase voltage, V_r	V	33.7	60.7	92	124.6	150.7	176.1	210.9	235
Rotor current, I_r	A	0.92	1.67	2.53	3.4	4.12	4.8	5.74	6.37
Mechanical torque, T_m	Nm	2.5	4.45	9.1	14.6	15	19.7	27	32.9
Mechanical power, P_m	kW	0.36	0.7	1.43	2.3	2.36	3.09	4.233	5.166
Rotor power, P_r	kW	-0.09	-0.3	-0.696	-1.27	-1.86	-2.54	-3.63	-4.49
Efficiency	%	26	43	48.7	55	78.8	82	85.8	87

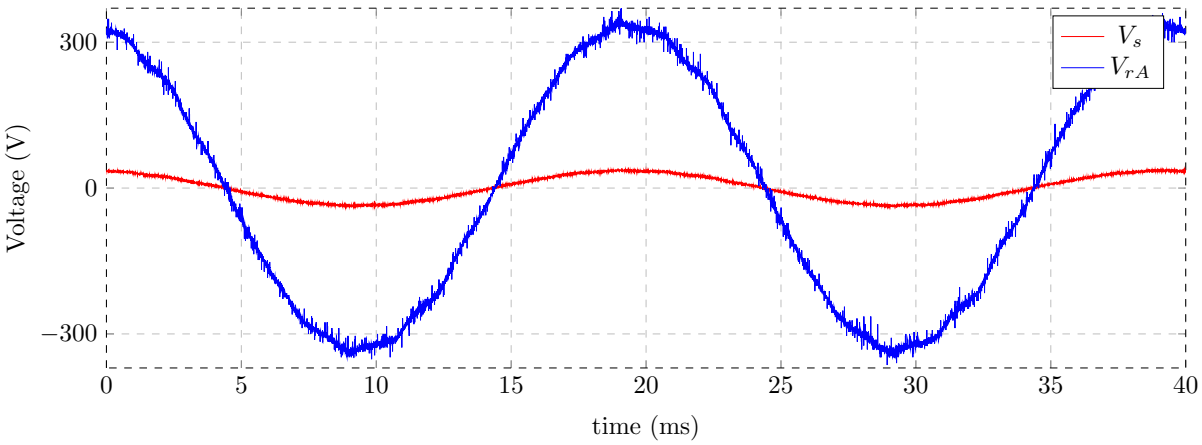

Figure 7.7: Stator voltage and induced rotor voltage at synchronous speed (8A)

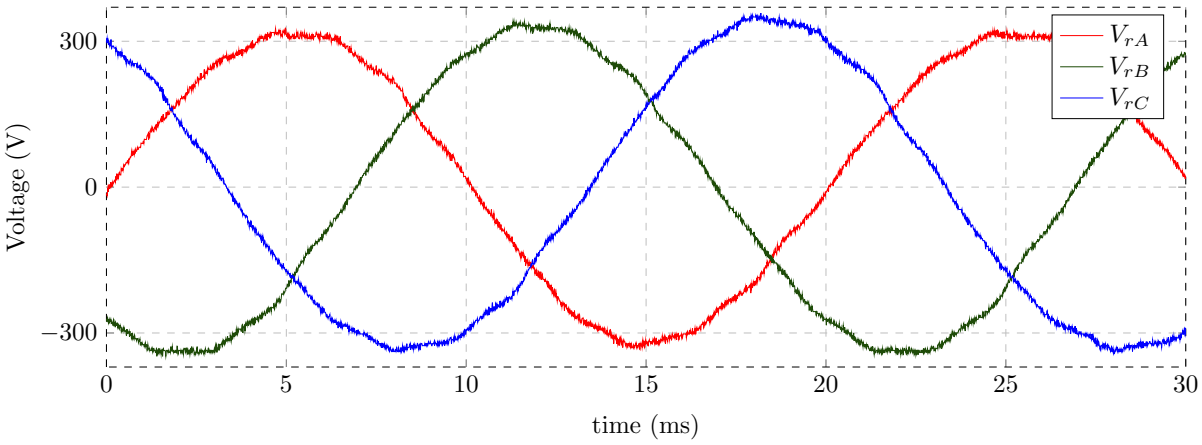

Figure 7.8: Rotor induced voltages at synchronous speed (8A)

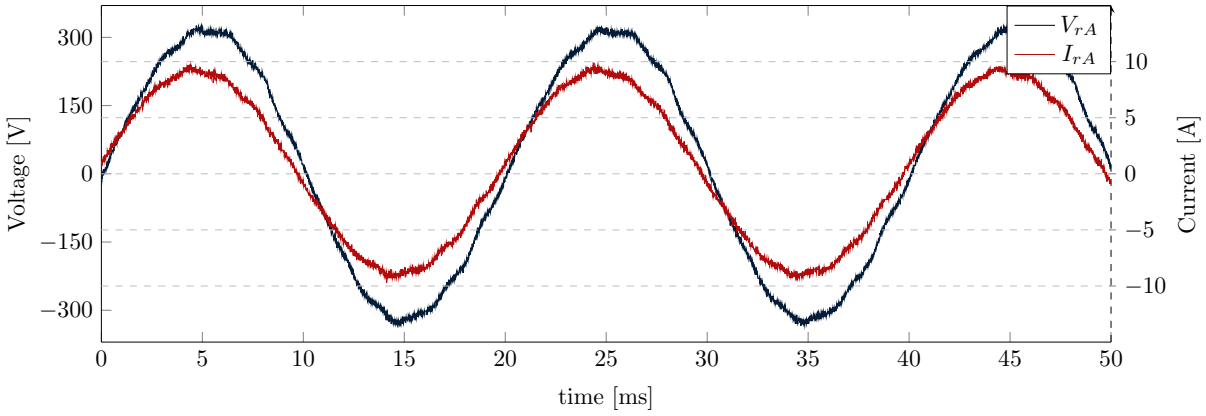

Figure 7.9: Rotor induced voltage and current at synchronous speed (8A)

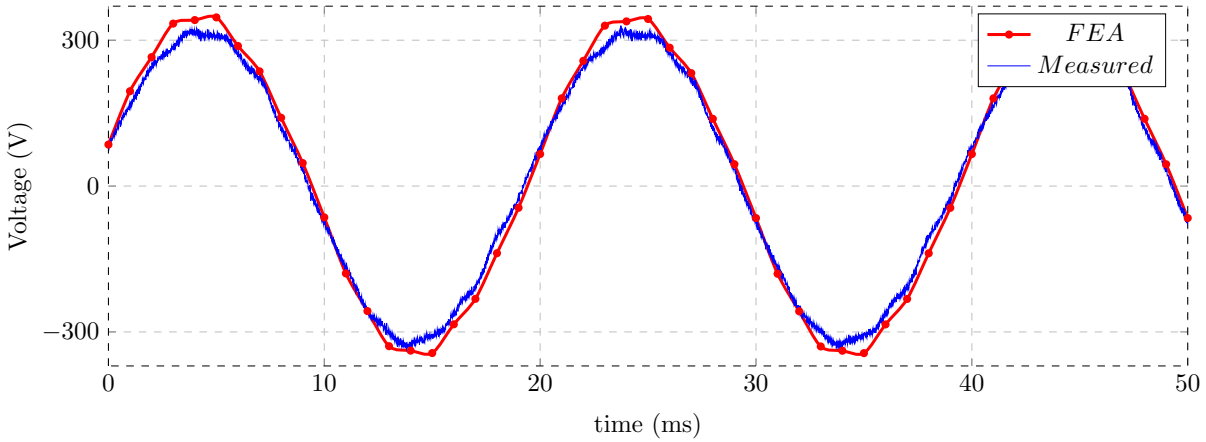

Figure 7.10: FEA and measured rotor induced voltages at synchronous speed (8A)

7.2.3 Sub-synchronous speed test results

At the rated current of $5.6A_{rms}$ on the stator, the induced voltage on the rotor is just over 200 V. The stator current is supplied at a power factor of 0.86. The voltage supplied by the AC drive and the current in the stator at 975 rpm are illustrated in Figures 7.11 and 7.12 respectively. The PWM voltage waveform from the AC drive is illustrated with a moving average function. The induced voltages on the rotor at 975 rpm are illustrated in Figures 7.13. The rotor-side is at unity power factor, similar to the test at synchronous speed.

The voltage from the AC drive is noisy given the unfiltered PWM signal nature. Consequently, the harmonic content for the sub-synchronous speed test is higher than the synchronous speed. The measured current and voltage THDs at the rotor-side are 3.2 % and 6.2 % respectively. The efficiency of the generator at the sub-synchronous test is 85.3% and is similar to the efficiency at the rated stator current at synchronous speed.

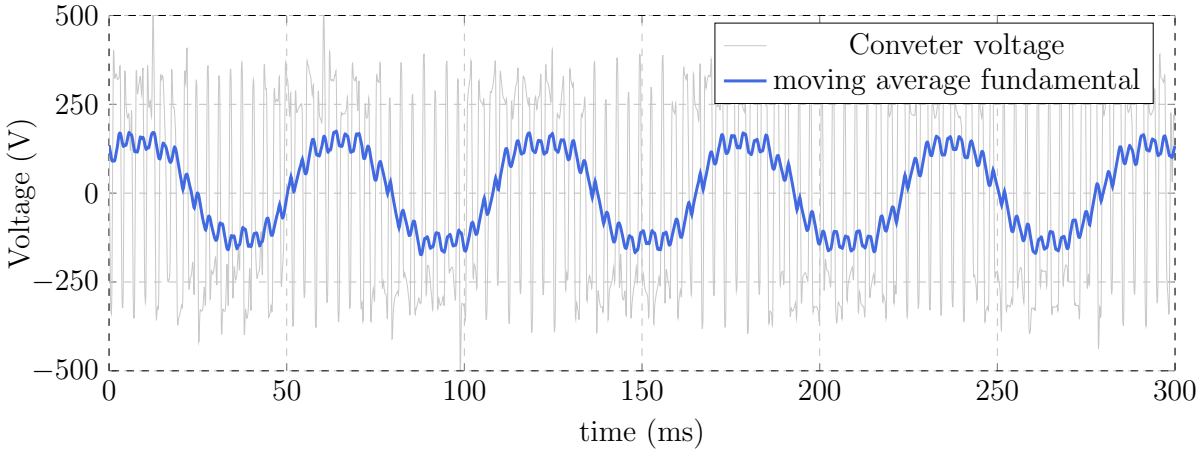

Figure 7.11: Stator phase voltage supplied by AC drive at 975 rpm (17.5 Hz).

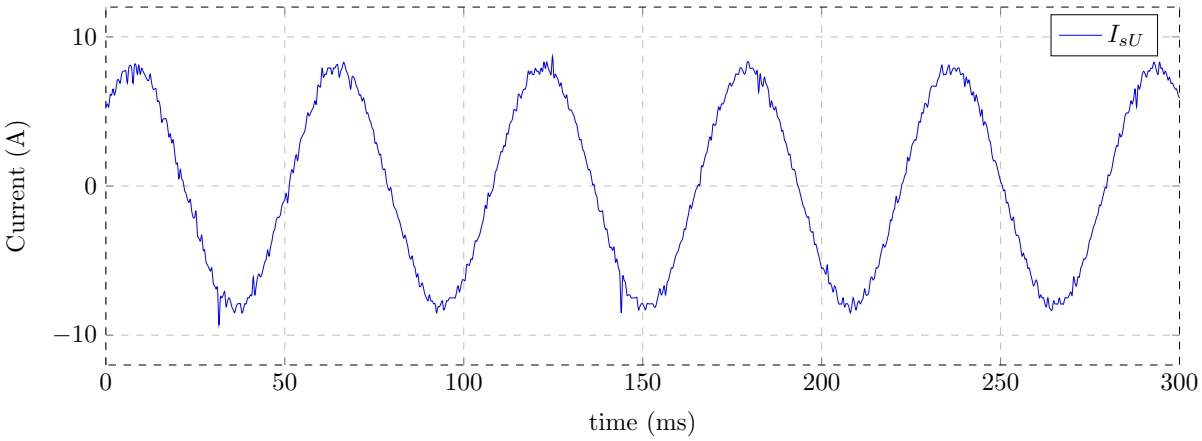

Figure 7.12: Stator phase current at 975 rpm (17.5 Hz).

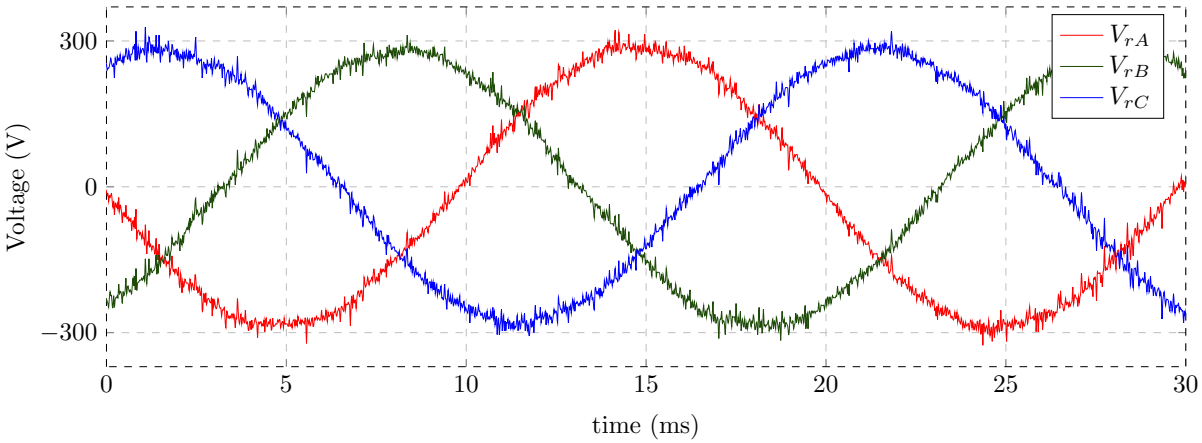

Figure 7.13: Rotor induced voltages at 975 rpm.

7.2.4 Super-synchronous region test results

The prototype is tested at two speeds in the super-synchronous region. The first speed is 1650 rpm in which a (-)5 Hz excitation is applied by the drive to the stator windings. The

second test in the super-synchronous region is at the rated design speed of the prototype (2025 rpm), at which (-)17.5 Hz excitation is applied to the stator.

Test at 1650 rpm

The efficiency of the prototype at 1650 rpm for the rated stator current of $5.6A_{rms}$ is 81%, with the stator side power factor at 0.6. The power factor at 1650 rpm is significantly lower than at 975 rpm, and this is a likely cause of the drop in efficiency as compared to the tests at synchronous speed and 975 rpm.

The voltage supplied by the AC drive and stator current at 1650 rpm are illustrated in Figures 7.14 and 7.15 respectively. The three phase rotor induced voltages at 1650 rpm are illustrated in Figure 7.16. The measured current and voltage THDs for the test at 1650 rpm at the rotor-side are 3 % and 7.5 % respectively.

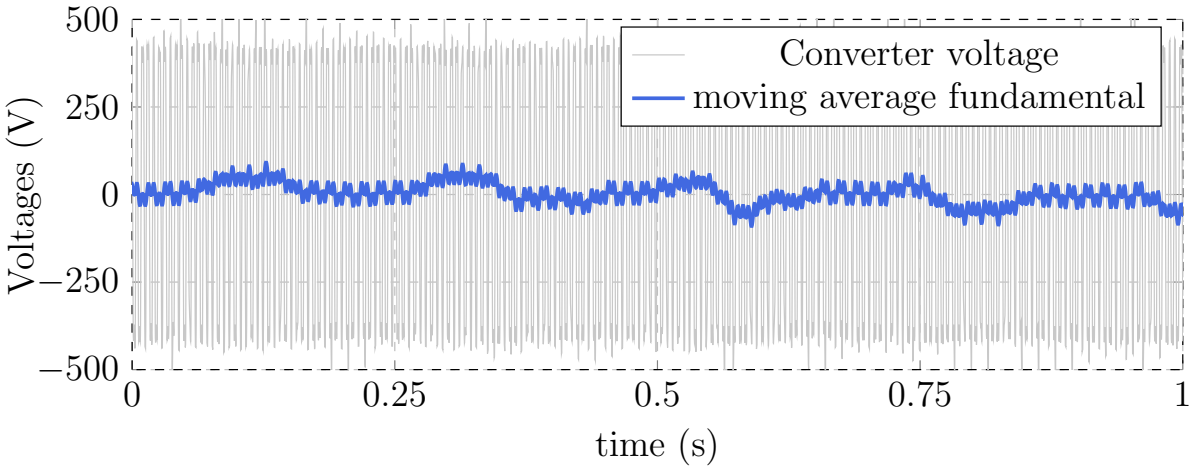

Figure 7.14: Stator phase voltage supplied by AC drive at 1650 rpm (-5 Hz).

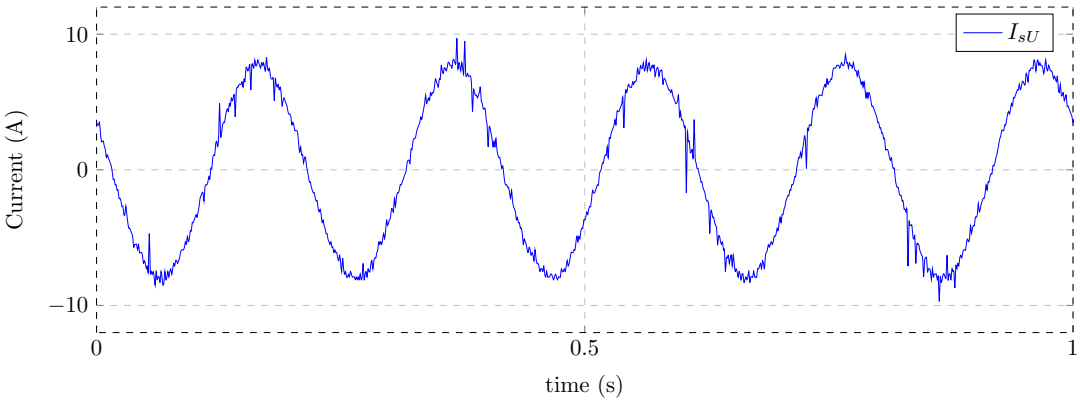

Figure 7.15: Stator phase current supplied by AC drive at 1650 rpm (-5 Hz).

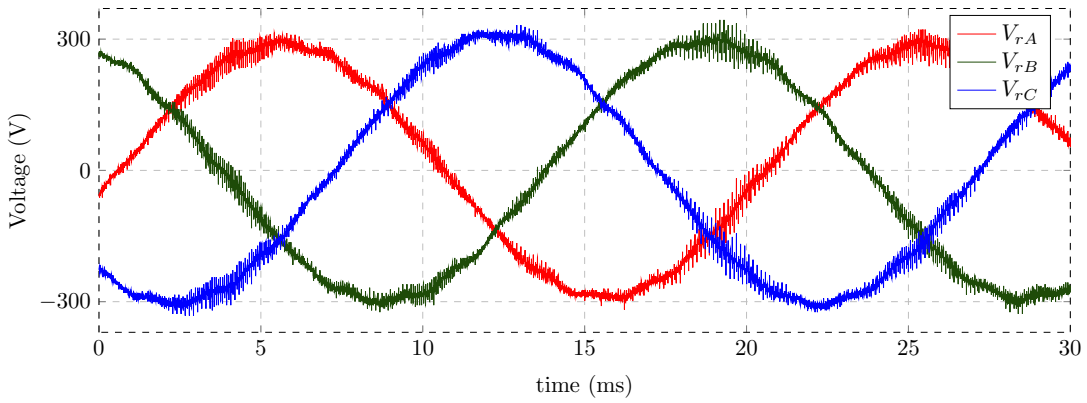

Figure 7.16: Rotor induced voltages at 1650 rpm.

Test at 2025 rpm

The stator side power factor is increased to 0.78 at 2025 rpm and the prototype efficiency is 82.7 %. The voltage supplied by the AC drive and stator current at 2025 rpm are illustrated in Figures 7.17 and 7.18 respectively.

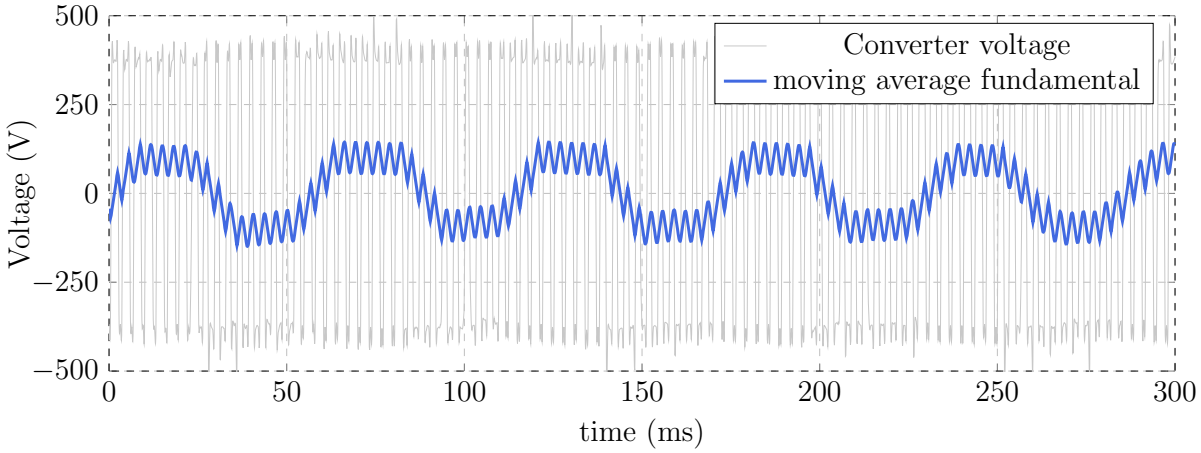

Figure 7.17: Stator phase voltage supplied by AC drive at 2025 rpm (-17.5 Hz).

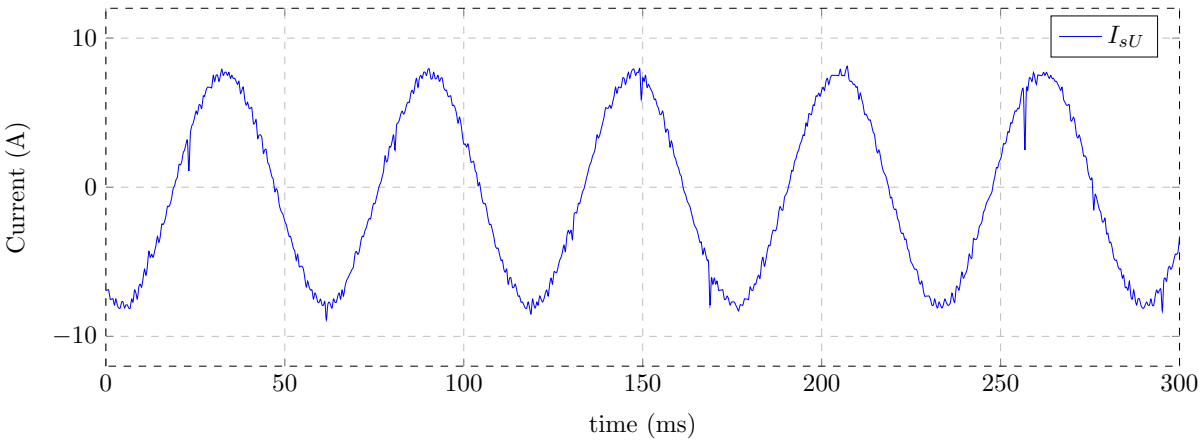

Figure 7.18: Stator phase current supplied by AC drive at 2025 rpm (-17.5 Hz).

The induced rotor voltage waveform at 2025 rpm as captured by the oscilloscope is really noisy as illustrated in Figure 7.19. However the current waveform is not as noisy with a THD value of 3.8%. The voltage as observed from the power analyzer is a lot less noisy with a THD around 4%.

7.2.5 Experimental results summary

A summary of the experimental results of the tests conducted on the prototype at synchronous speed, 975 rpm (sub-synchronous speed), 1650 rpm & 2025 rpm (super-synchronous speeds) is given in Table 7.5. The negative value of the rotor power and the stator power at super-synchronous speeds is used to indicate power being generated. The power factor values given in brackets are for the stator side. The resistive nature of the load connected to the rotor overshadows the rotor winding impedance, thus all the power factors measured at the rotor side at the different speeds are approximately at unity power factor.

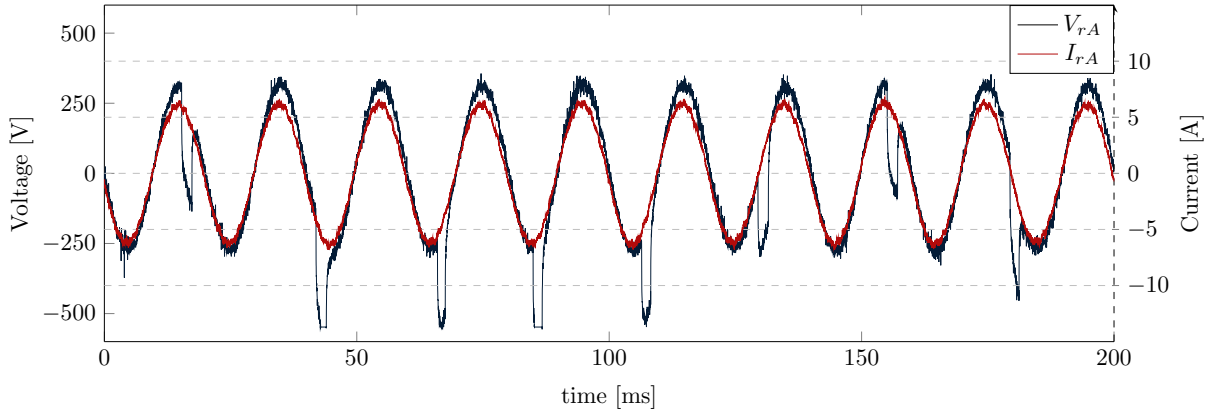

Figure 7.19: Rotor induced voltage and current at 2025 rpm.

Table 7.5: Experimental results

Parameters	**Unit**	**Speed (rpm)**				
		975	1500	1500	1650	2025
Rotor phase voltage, V_r	V	202	210	235	204	204.3
Rotor current, I_r	A	5.51	5.74	6.37	5.56	5.59
Stator phase voltage, V_s	V	99.3	26.7	30.4	18.9	83.6
Stator current, I_s	A	5.6	7	8	5.6	5.6
Mechanical torque, T_m	Nm	24.6	27	32.9	25.67	25.82
Mechanical input power, P_m	kW	2.515	4.23	5.166	4.43	5.475
Rotor power, P_r	kW	-3.34	-3.63	-4.49	-3.4	-3.43
Stator Power, P_s	kW	1.4	-	-	-0.2	-1.1
Rotor voltage THD	%	6.2	2	3.83	7.5	4
Rotor current THD	%	3.2	2	2.4	3	3.8
Rotor power factor (stator)	-	1(0.86)	1(1)	1(1)	1(0.6)	1(0.78)
Efficiency	%	85.3	85.8	87	81	82.7

The stator connection at synchronous speed is such that the same DC voltage source is connected to the two phases in use, although in different directions. This voltage source combines with the sum of resistances of the two phases to produce the necessary current, hence its value.

Although, the induced voltage in the rotor at 2025 rpm is noisy as illustrated in Figure 7.19, the THD values as for all the other tests is measured by the power analyzer. The efficiency is calculated by computing the mechanical input power measured by the torque sensor with the measured input/output power at the stator-side (measured by the AC drive) and the output power at the rotor-side (measured by the power analyzer).

7.3 Summary

In this chapter, the testing of a 5.5 kW rotor-tied DFIG prototype is discussed. The testing is done without a control system and the prototype is tested in a standalone DFIG mode. The main points in the chapter are as follows:

- Machine parameter testing was conducted to determine the prototype's parameters and compare with analytical estimations. The measured resistances were similar to the analytical estimations while the measured inductances were slightly higher than their estimated values.
- The prototype is tested in 3 operating regions: the sub-synchronous, synchronous and the super-synchronous regions.
- For the tests, the stator was connected to a DC source at synchronous speed and to an Allen-Bradley drive at other speeds to provide slip frequency excitation while the rotor was connected to a resistive load.
- The synchronous speed test and sub-synchronous speed test at the rated stator current had similar efficiencies at about 85 %. The tests at super-synchronous speeds had lower efficiencies. An efficiency of 87 % is observed at a synchronous speed test with a slightly higher stator current than the rated current (8A compared to the rated 7A).

Chapter 8

Conclusions and Recommendation

The rotor-tied DFIG configuration is extensively investigated and described in this study. The steady state mode of operation of rotor-tied DFIGs in wind turbines is clearly detailed with a developed transformer model equivalent circuit also described. A comprehensive design methodology for rotor-tied DFIGs is developed which is used to obtain an initial design for a prototype. The initial design is optimized to obtain a final design for the prototype. The prototype is tested to validate the design methodology and FEA. In this chapter, the conclusions reached from this study with recommendations for future work are stated.

8.1 Conclusions

The following conclusions are drawn from this study on the design methodology of a rotor-tied DFIG:

- The mode of operation of rotor-tied DFIGs was comprehensively described, with an alternative way of calculating slip which is similar to conventional DFIG slip. The estimated proportion of power handled by the stator of a rotor-tied DFIG (rotor of conventional DFIG) with slip was calculated analytically and illustrated with FEA. The transformer model equivalent circuit of rotor-tied DFIGs is also discussed.
- A detailed design process is given for rotor-tied DFIGs, clearly stating how the rotor is sized. The process, which seeks to obtain rotor-tied DFIGs with superior power densities and lower space harmonics, explains the impact of design parameter choices. The method of calculating the number of turns per phase in the stator of rotor-tied DFIGs (or rotor of conventional DFIGs) based on a convenient voltage choice is shown. The calculation of the dimensions of rotor slots with parallel teeth is clearly explained.
- FEA of rotor-tied DFIGs connected to a grid is illustrated, and critical performances of rotor-tied DFIGs designs can be evaluated using the FEA configuration. The use of larger number of slots on the rotor compared to the stator of rotor-tied DFIGs was shown to have a higher power density. For small power rotor-tied DFIGs, using the rotor voltage on the stator leads to too many stator turns per slot with very small cross-sections. As a result, although using the same voltage avoids the use of a transformer at the stator side of the rotor-tied DFIG, using a lower voltage on the stator may be more practical.
- When designing a DFIG, maximizing the turns per phase within permissible values as applicable to the power and voltage ratings, and using higher aspect ratios, can produce better machines in terms of higher power factors and lower harmonic content. With the design methodology developed in this project, there is not much

to suggest that rotor-tied DFIGs have higher power densities than conventional DFIGs. Higher teeth flux densities than prescribed in literature reduce the power factors of DFIGs while also increasing harmonic content. On the other hand, it seems that increasing the core flux densities slightly higher than prescribed values can reduce harmonic content and increase power densities although with reduced power factors.

- As regards optimization, the use of a response surface approximation with a genetic algorithm was shown to considerably reduce optimization execution time as opposed to using FEA directly with the genetic algorithm. The response surfaces also give acceptable estimations of performances of machines with different design variables. The accuracy of the response surfaces can be improved by increasing the number of samples. The LHS method was shown to be an efficient sampling method but when increasing the number of initial samples, it may be better to combine another sampling technique to ensure coverage at extremes of the design variable space.

  Modifying the air-gap diameter and the slot shapes of a rotor-tied DFIG by an optimization process can reduce harmonic content to permissible levels and increase the power density. This can be done while keeping a lid on the outer stator and inner rotor diameter.

- The appropriate mechanical tolerances have to be keenly observed for lamination keys and keyways on the shaft, otherwise the laminations which are supposed to be slide fitted on the shaft may require filing which can also cause misalignment. When using an already designed shaft, it is vital to have a "shoulder" piece on which the laminations rest on while stacking to ensure alignment especially when skewing is required. If the "shoulder" is not present on the designed shaft, a shrink fit ring can be fitted on the shaft to serve this purpose before stacking the rotor laminations.

- Testing a rotor-tied DFIG in a standalone mode at specific speeds without a control system has been illustrated; it involves using a DC source connected to the stator terminals at synchronous speed or an AC drive connected at slip speeds. The tests takes a different approach to testing DFIGs as seen in literature, in which the machines are tested as motors or DC generators, and are evaluated by the torque production or DC generation in the absence of a control system. This can be misleading as a wound rotor induction machine working as a motor, induction generator or DFIG have differences in torque output. The approach used in this project takes the testing closer to how an actual DFIG works.

- The efficiency of the prototype for the synchronous and sub-synchronous with the rated stator current were similar. Raising the stator current by 1A at synchronous speed significantly raised the power generated and efficiency. It is reckoned that the lack of grid connection reduces the excitation available to the generator. The performance of the prototype is expected to improve with a grid connection. The prototype efficiency at super-synchronous speed tests had lower efficiencies than expected. The stator power factor at this speeds was noticeably low and could be the reason for the reduced efficiency.

8.2 Recommendations

Certain areas in the design and testing of a rotor-tied DFIG need further investigation and they are listed as follows:

- During construction, designing a custom shaft within IEC standards may afford greater degrees of freedom during the design of a small rotor-tied DFIG prototype. The custom shaft design should have a shoulder base for the rotor laminations to rest on for proper alignment. Having a custom frame also helps but the costs may far outweigh the benefits unlike for the shaft.
- A fractionally rated AC drive as compared to the machine power, can be used to excite the stator of a rotor-tied DFIG for a standalone test, and the performance investigated especially at super-synchronous speeds.
- It will be interesting to test a rotor-tied DFIG designed according to the methodology in this research with a DFIG control system (with grid connection). With this, the efficiency of the machine can be clearly observed at different speeds. Excitation from the grid is also expected to improve the machine performance compared to a standalone system.

References

[1] FS-UNEP, "Global Trends in Renewable Energy Investment 2016," p. 84, 2016. [Online]. Available: http://fs-unep-centre.org/sites/default/files/publications/globaltrendsinrenewableenergyinvestment2016lowres_0.pdf

[2] Climate Council, "Key Issues for the New Climate Agreement," 2015. [Online]. Available: https://www.climatecouncil.org.au/uploads/de494149f16b3b235d8fa74fb8a9c52d.pdf

[3] REN21, *Renewables 2016: Global Status Report*, 2016. [Online]. Available: http://www.ren21.net/wp-content/uploads/2016/10/REN21_GSR2016_FullReport_en_11.pdf

[4] Global Wind Energy Council, "Global Wind Report Annual Market Update 2015," 2015. [Online]. Available: http://www.gwec.net/wp-content/uploads/vip/GWEC-Global-Wind-2015-Report_April-2016_22_04.pdf

[5] WEC, "World Energy Resources," p. 468, 2016. [Online]. Available: https://www.worldenergy.org/wp-content/uploads/2016/10/World-Energy-Resources_Report_2016.pdf

[6] Department of Trade and Industry, "The wind energy industry localisation roadmap in support of large -scale roll-out in South Africa," no. January, 2015. [Online]. Available: http://www.wasaproject.info/docs/WindEnergyLocalisationStudyJan2015.pdf

[7] H. Polinder, J. A. Ferreira, B. B. Jensen, A. B. Abrahamsen, K. Atallah, and R. a. McMahon, "Trends in Wind Turbine Generator Systems," *IEEE Journal of Emerging and Selected Topics in Power Electronics*, vol. 1, no. 3, pp. 174–185, 2013.

[8] S. Müller, M. Deicke, and D. W., & Rik Doncker, "Doubly fed induction generator systems for wind turbines," *Industry Applications Magazine, IEEE*, vol. 8, no. 3, pp. 26–33, 2002.

[9] G. Abad, J. López, M. Rodríguez, L. Marroyo, and G. Iwanski, *Doubly Fed Induction Machine: Modeling and Control for Wind Energy Generation*, ser. IEEE Press Series on Power Engineering. Wiley, 2011.

[10] W. Cao, Y. Xie, and Z. Tan, "Wind Turbine Generator Technologies," in *Advances in Wind Power*. InTech, 2012.

[11] M. Lindholm and T. W. Rasmussen, "Harmonic analysis of doubly fed induction generators," in *The Fifth International Conference on Power Electronics and Drive Systems, 2003. PEDS 2003.*, vol. 2, Nov 2003, pp. 837–841 Vol.2.

[12] I. Boldea and S. Nasar, *The Induction Machines Design Handbook, Second Edition*, ser. Electric Power Engineering Series. Taylor & Francis, 2009.

[13] M. Say, *The Performance and Design of Alternating Current Machines: Transformers Three-phase Induction Motors and Synchronous Machines*. CBS Pub., 1983.

[14] J. Pyrhönen, T. Jokinen, and V. Hrabovcová, *Design of Rotating Electrical Machines*. Wiley, 2008.

[15] H. A. Toliyat and G. B. Kliman, *Handbook of Electric Motors*. CRC Press, 2004.

[16] I. Boldea, *Variable Speed Generators*. CRC Press, 2005.

[17] V. Delli Colli, F. Marignetti, and C. Attaianese, "Analytical and multiphysics approach to the optimal design of a 10-MW DFIG for direct-drive wind turbines," *IEEE Transactions on Industrial Electronics*, vol. 59, no. 7, pp. 2791–2799, 2012.

[18] G. I. Vakil and K. R. Rajagopal, "Computer aided design of a compact doubly-fed induction generator for small wind power application," in *2010 Joint International Conference on Power Electronics, Drives and Energy Systems 2010 Power India*, Dec 2010, pp. 1–4.

[19] S. P. Barave and B. H. Chowdhury, "Optimal design of induction generators for space applications," *IEEE Transactions on Aerospace and Electronic Systems*, vol. 45, no. 3, pp. 1126–1137, July 2009.

[20] Y.-M. You, T. a. Lipo, and B.-I. Kwon, "A Novel Grid-connected to Rotor Type Doubly Fed Induction Generator for Wind Turbine Systems," in *8th International Conference on Power Electronics - ECCE Asia*, The Shilla Jeju, 2011, pp. 646–653.

[21] ——, "Design and Analysis of a Novel Grid-Connected to Rotor Type Doubly Fed Induction Machine," *IEEE Transactions on Magnetics*, vol. 48, no. 2, pp. 919–922, 2012.

[22] ——, "Optimal Design of a Grid-Connected-to-Rotor Type Doubly Fed Induction Generator for Wind Turbine Systems," *IEEE Transactions on Magnetics*, vol. 48, no. 11, pp. 3124–3127, 2012.

[23] N. David and D. C. Aliprantis, "DFIG with grid-connected rotor for wind energy conversion system," *Proceedings of the 2013 IEEE International Electric Machines and Drives Conference, IEMDC 2013*, pp. 125–130, 2013.

[24] ——, "Improved efficiency of dfig wind energy conversion systems by operating in the rotor-tied configuration," in *Electrical Machines (ICEM), 2014 International Conference on*, Sept 2014, pp. 189–195.

[25] S. Williamson and a.C. Ferreira, "Generalised theory of the brushless doubly-fed machine. Part 2: Model verification and performance," *IEE Proceedings - Electric Power Applications*, vol. 144, no. 2, p. 123, 1997.

[26] N. L. Zietsman and N. Gule, "Optimal design methodology of a three phase rotary transformer for doubly fed induction generator application," in *IEEE International Electric Machines Drives Conference (IEMDC)*, May 2015, pp. 763–768.

[27] L. Fan, S. Yuvarajan, and R. Kavasseri, "Harmonic analysis of a dfig for a wind energy conversion system," *IEEE Transactions on Energy Conversion*, vol. 25, no. 1, pp. 181–190, March 2010.

[28] Y. Liao, L. Ran, G. A. Putrus, and K. S. Smith, "Evaluation of the effects of rotor harmonics in a doubly-fed induction generator with harmonic induced speed ripple," *IEEE Transactions on Energy Conversion*, vol. 18, no. 4, pp. 508–515, Dec 2003.

[29] Z. Tan, X. Song, W. Cao, Z. Liu, and Y. Tong, "DFIG Machine Design for Maximiz-

ing Power Output Based on Surrogate Optimization Algorithm," *IEEE Transactions on Energy Conversion*, vol. 30, no. 3, pp. 1154–1162, 2015.

[30] J. Fletcher and J. Yang, "Introduction to Doubly-Fed Induction Generator for Wind Power Applications," *Paths to Sustainable Energy*, pp. 259–278, 2010.

[31] L. Qu and W. Qiao, "Constant power control of DFIG wind turbines with supercapacitor energy storage," *IEEE Transactions on Industry Applications*, vol. 47, no. 1, pp. 359–367, 2011.

[32] C. Abbey and G. Joós, "A systematic approach to design and operation of a doubly fed induction generator," *Electric Power Systems Research*, vol. 78, no. 3, pp. 399–408, 2008.

[33] A. Still and C. Siskind, *Elements of Electrical Machine Design*. McGraw-Hill, 1954.

[34] M. Deshpande, *Design And Testing Of Electrical Machines*. Prentice-Hall Of India Pvt. Limited, 2010.

[35] A. Shanmugasundaram and R. Palani, *Electrical Machine Design Data Book*. New Age International (p) Limited, 1979.

[36] ANSYS inc, "Design of Experiments (DOE) Introduction to ANSYS DesignXplorer Available DOE schemes," pp. 1–19, 2013.

[37] J. B. Kim, K. Y. Hwang, and B. I. Kwon, "Optimization of two-phase in-wheel IPMSM for wide speed range by using the kriging model based on latin hypercube sampling," *IEEE Transactions on Magnetics*, vol. 47, no. 5, pp. 1078–1081, 2011.

[38] K. R. Davev, "Latin hypercube sampling and pattern search in magnetic field optimization problems," *IEEE Transactions on Magnetics*, vol. 44, no. 6, pp. 974–977, 2008.

[39] J. Gyselinck, L. Vandevelde, and J. Melkebeek, "Modelling of electric machines with skewed slots using the two dimensional finite element method," in *International Conference on Electrical Machines (ICEM)*, Vigo, September 1996.

Appendices

Equivalent circuit parameter calculatons

A.1 Winding resistances

The phase winding resistance R of the rotor or stator is estimated as in [12]:

$$R = \rho_{cu} \frac{l_c W}{A_{co} a_b} \tag{A.1}$$

Where:
ρ_{cu} = Copper resistivity at machine operating temperature
l_c = coil length
A_{co} = Conductor cross sectional area
a_b = number of parallel branches in the winding
The coil length is the addition of the machine stack length (L) and end connection length (l_{end}) as given:

$$l_c = 2(L + l_{end}) \tag{A.2}$$

For a 4 pole machine, the end connection length can be estimated from the empirically developed formula:

$$l_{end} = 2y - 0.02 \quad \text{m} \tag{A.3}$$

$$y = \tau\beta \tag{A.4}$$

Where:
y = coil pitch
τ = machine pole pitch
β = winding pitch/chording factor

A.2 Leakage Inductances

The leakage inductance of the rotor or stator ($L_{lr,s}$) is given as:

$$L_{lr,s} = \frac{2\mu_0 W^2 L(\lambda_s + \lambda_{ds} + \lambda_{ec})}{p_1 q} \tag{A.5}$$

With:
μ_0 = permeability of free space
λ_s = geometrical specific slot permeance
λ_{ds} = differential leakage coefficient
λ_{ec} = end winding leakage coefficient
q = no slots per pole per phase

$$\lambda_s = \left(\frac{2h_{r,s}}{3(b_{r,s1} + b_{r,s2})} + \frac{2h_w}{b_{or,s} + b_{r,s1}} + \frac{h_{or,s}}{b_{or,s}} \right) \left(\frac{1 + 3\beta}{4} \right) \tag{A.6}$$

$$\lambda_{ds} = \frac{0.9\tau_{r,s} q^2 K_{wr,s}^2 C_{r,s} \gamma_{ds}}{K_c g(1 + K_{st})} \tag{A.7}$$

K_c is the carter coefficient, which can be described as a ratio between the equivalent machine air-gap and the actual physical air-gap.

$$C_{r,s} = 1 - \frac{0.033 b_{or,s}^2}{g\tau_{r,s}} \tag{A.8}$$

$$\begin{aligned} \gamma_{ds} &= (0.25 sin\varphi + 2.6) \times 10^{-2} \quad \text{for q} = 2 \\ \gamma_{ds} &= (0.18 sin\varphi + 1.24) \times 10^{-2} \quad \text{for q} = 3 \\ \varphi &= \pi(6\beta - 5.5) \end{aligned} \tag{A.9}$$

$$\lambda_{ec} = \frac{0.34q}{L}(l_{end} - 0.64\beta\tau) \tag{A.10}$$

A.3 Magnetizing Inductance

The magnetizing inductance calculated with reference to the rotor (the primary side) is estimated as:

$$L_m = \frac{6\mu_0 (W_r K_{wr})^2 \tau L}{\pi^2 p_1 K_c g(1 + K_s)} \tag{A.11}$$

Where:
K_s = total saturation factor [1]

[1] Should not be confused with k_{st}, the teeth saturation factor

Winding calculations

B.1 Winding induced voltage

The flux ϕ in a single turn coil is:

$$\phi = \phi_p \sin(2\pi f t), \tag{B.1}$$

where, f is the flux frequency (Hz), and the emf e induced in the coil is determined as:

$$e = \frac{d\phi}{dt} = 2\pi f \phi_p \cos(2\pi f t) \tag{B.2}$$

The rms value, E for this purely sinusoidal flux is obtained as [15]:

$$E = \frac{2\pi}{\sqrt{2}} f \phi_p = 4.44 f \phi_p. \tag{B.3}$$

Now, considering a full phase winding with number of turns N, and a winding factor k_w, the rms voltage induced is:

$$E_{ph} = 4 k_f k_w f N \phi_p. \tag{B.4}$$

The form factor k_f takes ferromagnetic core saturation into account which affects the shape of the flux waveform. k_f varies from 1.11 - 1.02, with 1.11 being the form factor for a purely sinusoidal waveform [12, 14].

The induced phase emf in the rotor windings is further obtained as:

$$\underline{E}_r = 4 k_f k_{wr} f_r N_r \underline{\phi}_m, \tag{B.5}$$

where, k_f is the form factor, k_{wr} is the rotor winding factor and $\underline{\phi}_m$ is the peak magnetizing flux. Correspondingly, the stator windings induced emf is determined as;

$$\underline{E}_s = 4 k_f k_{ws} f_s N_s \underline{\phi}_m, \tag{B.6}$$

where, k_{ws} is the stator winding factor.
In making the equivalent circuit less cumbersome, the stator parameters are referred to the rotor side such that:

$$\underline{E}_r = a_{rs}(s\underline{E}_s), \tag{B.7}$$

where a_{rs}, the effective turns ratio is determined as:

$$a_{rs} = \frac{k_{wr} N_r}{k_{ws} N_s}. \tag{B.8}$$

As done for transformer circuits, the stator (the secondary side) impedance components are referred to the rotor side as shown:

$$R'_s = a_{rs}^2 R_s \tag{B.9}$$

$$X'_{ls} = a_{rs}^2 X_{ls} \tag{B.10}$$

Similarly, the stator voltage and current referred to the rotor are obtained respectively:

$$\underline{V}'_s = a_{rs}\underline{V}_s \tag{B.11}$$

$$\underline{E}'_s = a_{rs}\underline{E}_s \tag{B.12}$$

$$\underline{I}'_s = \frac{\underline{I}_s}{a_{rs}} \tag{B.13}$$

Power factor calculation

Using the synchronous reference frame, the three phase space vectors (current, flux linkages and voltages) of the DFIG can be represented with the space vector notation [9]. This frame, which can be linked to either the stator or rotor flux [8] is rotating at the synchronous speed of the machine.

C.1 Power factor

Splitting the rotor and stator Induced voltages and currents into their component d,q equations in the synchronous reference frame, the power factor was calculated as follows:

$$V_d = \frac{2}{3}\left(V_a cos\theta + V_b cos(\theta - \frac{2\pi}{3}) + V_c cos(\theta + \frac{2\pi}{3})\right) \tag{C.1}$$

$$V_q = \frac{2}{3}\left(-V_a cos\theta - V_b cos(\theta - \frac{2\pi}{3}) - V_c cos(\theta + \frac{2\pi}{3})\right) \tag{C.2}$$

$$I_d = \frac{2}{3}\left(I_a cos\theta + I_b cos(\theta - \frac{2\pi}{3}) + I_c cos(\theta + \frac{2\pi}{3})\right) \tag{C.3}$$

$$I_q = \frac{2}{3}\left(-I_a cos\theta - I_b cos(\theta - \frac{2\pi}{3}) - I_c cos(\theta + \frac{2\pi}{3})\right) \tag{C.4}$$

Where:
$V_{a,b,c}$ = Induced voltages for phases a, b and c
$I_{a,b,c}$ = current in the phases
$\theta = 2\pi ft$

The reactive power and real power (P & Q) are calculated as:

$$P = \frac{3}{2}(V_d I_d + V_q I_q) \tag{C.5}$$

$$Q = \frac{3}{2}(V_q I_d - V_d I_q) \tag{C.6}$$

The apparent power is calculated as:

$$S = \sqrt{P^2 + Q^2} \tag{C.7}$$

From (C.7), the power factor,Pf is calculated as:

$$Pf = \frac{P}{S} \tag{C.8}$$

All these were calculated using output variables calculations in Maxwell.

Mechanical drawings

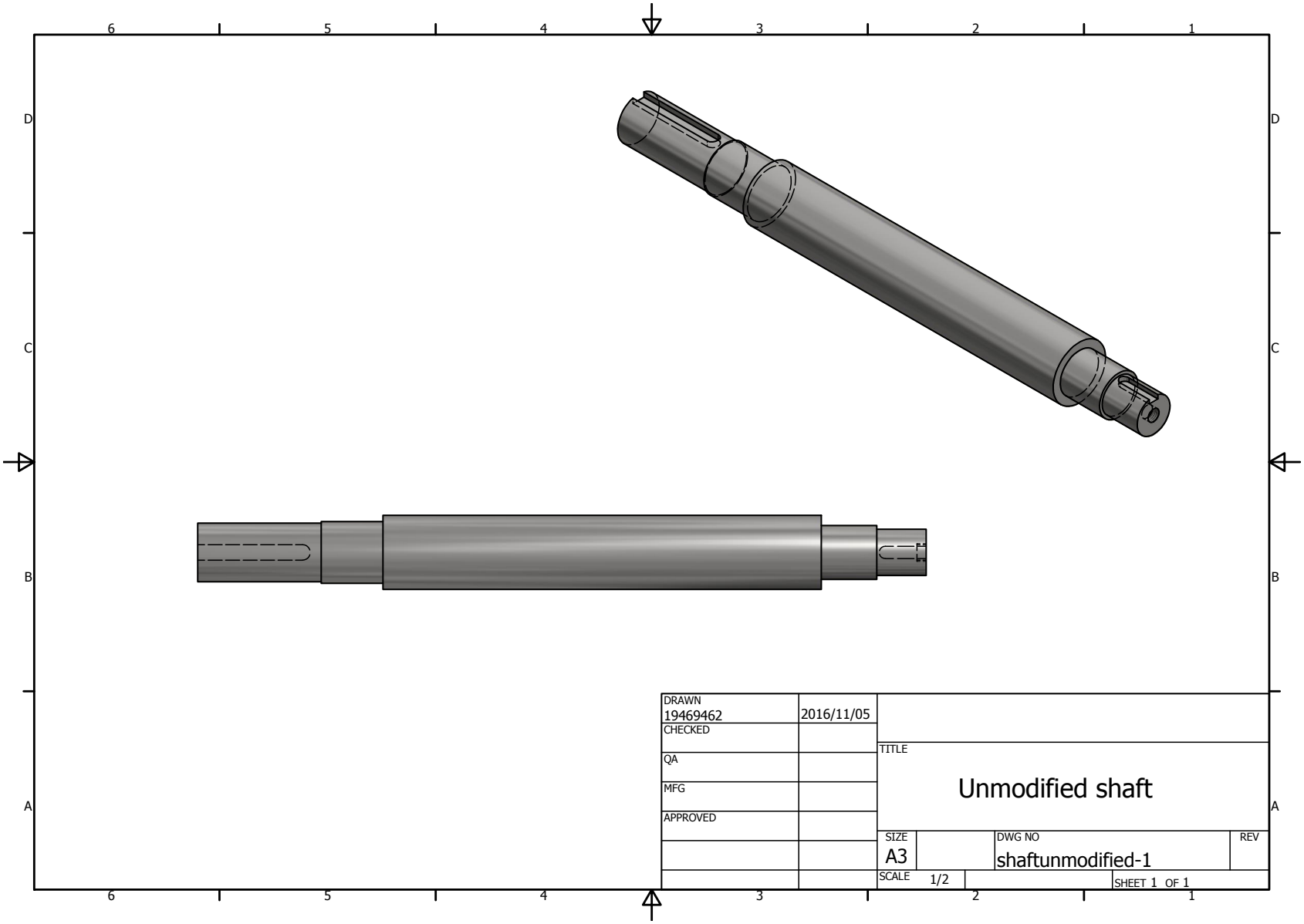

Figure D.1

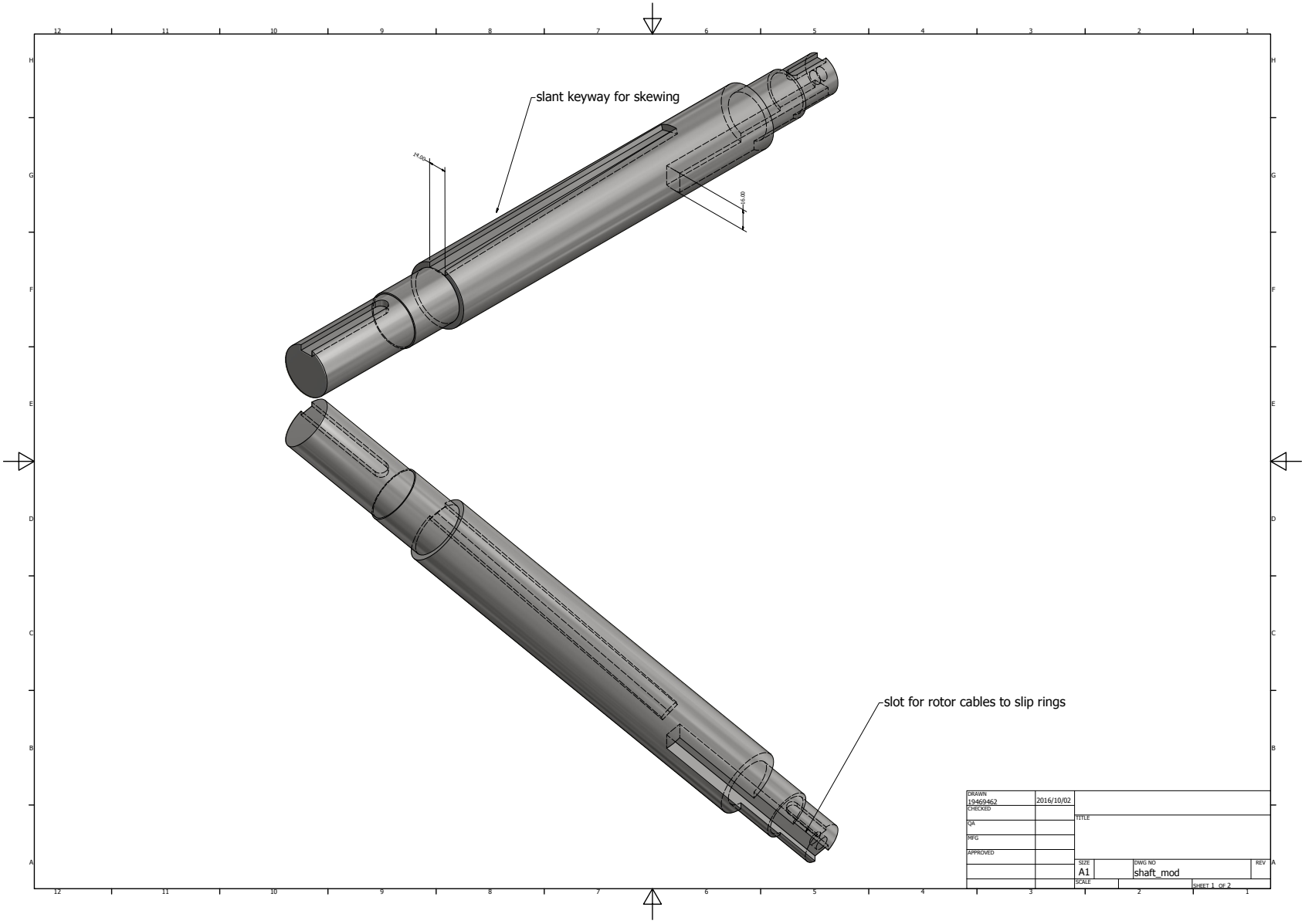

Figure D.2

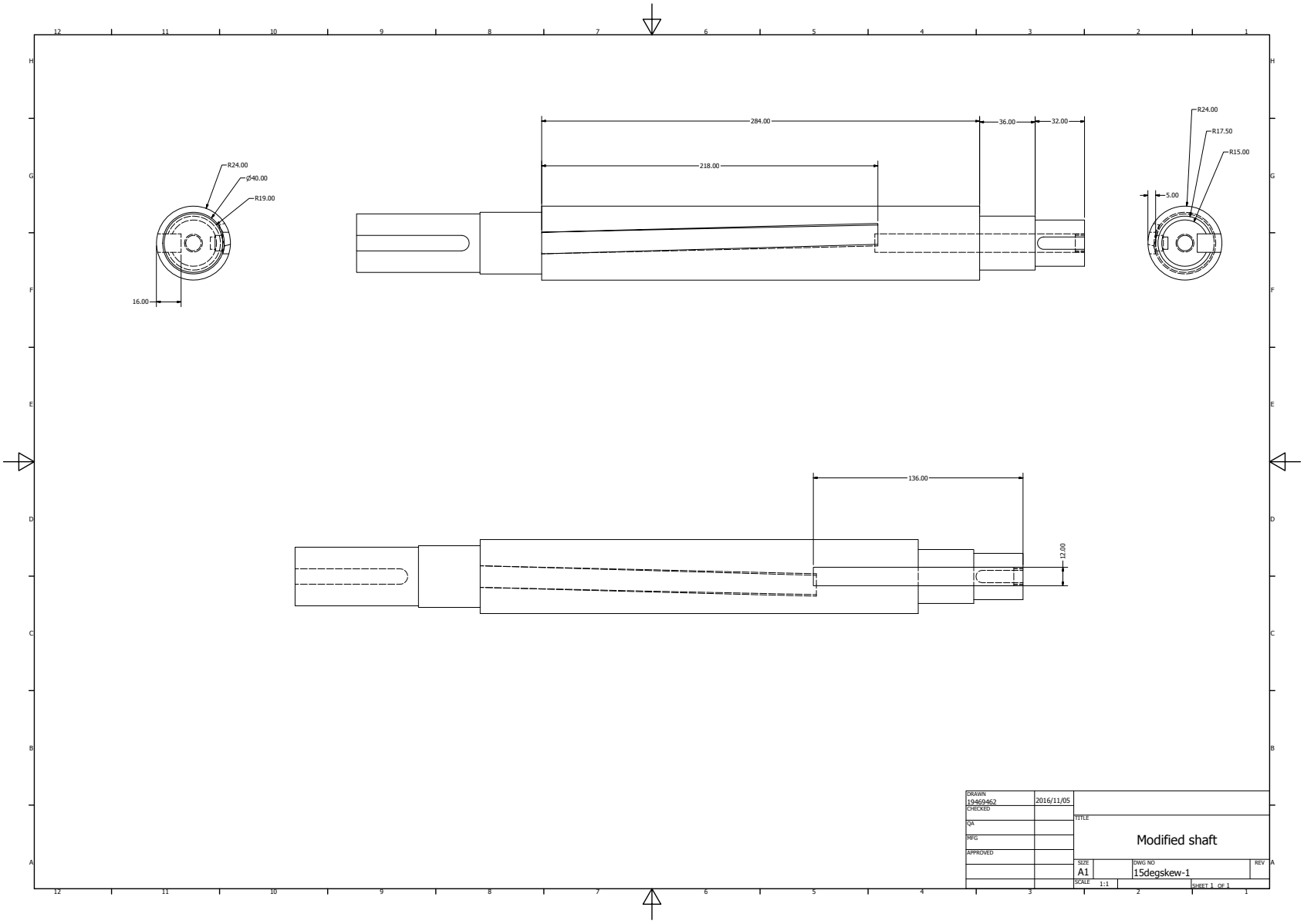

Figure D.3

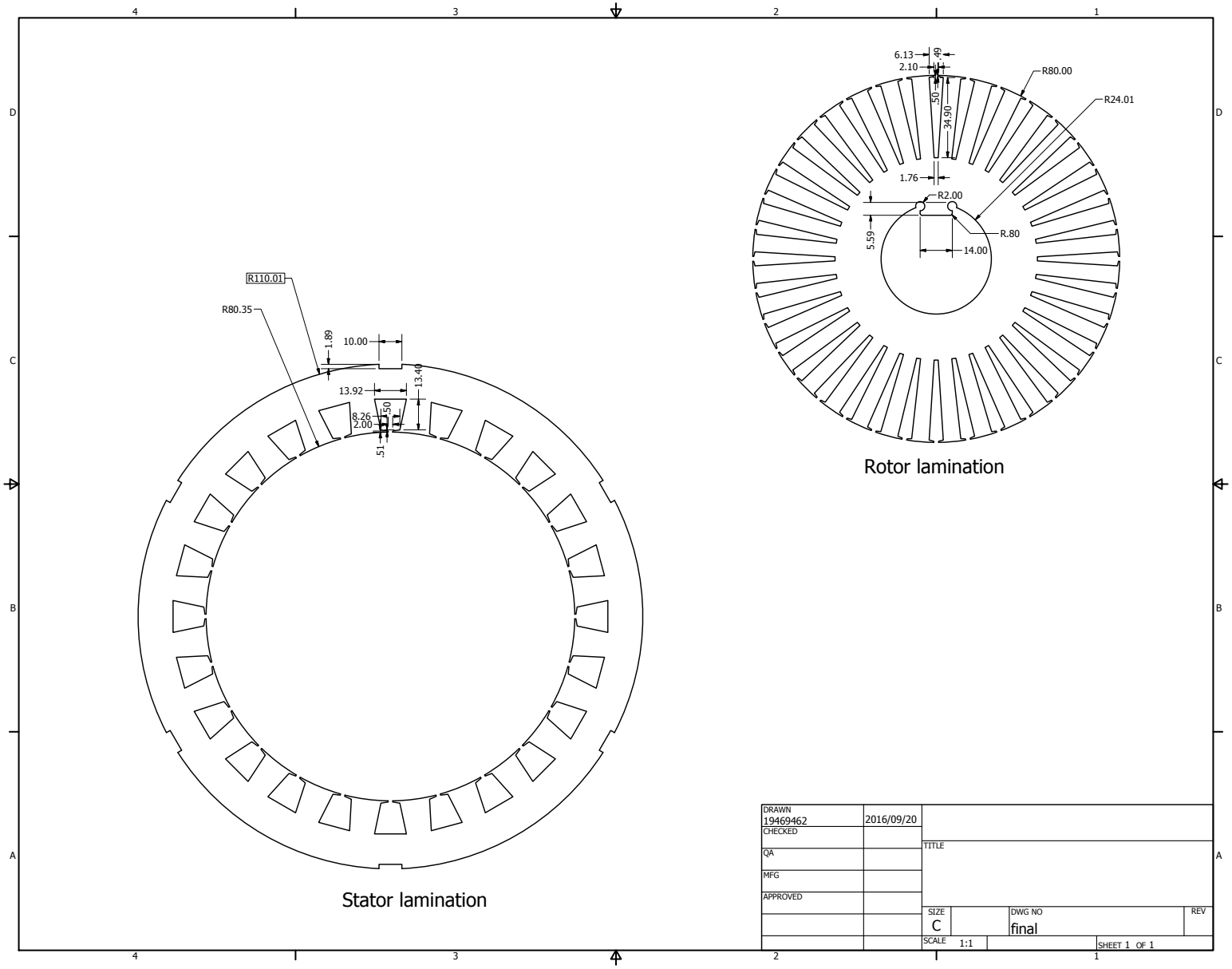

Figure D.4